January 2016

Sensitivity Of Two-Dimensional Stereo (2DS) Probe Derived Parameters To Particle Orientation

Joseph Robert O'brien

SENSITIVITY OF TWO-DIMENSIONAL STEREO (2DS) PROBE DERIVED PARAMETERS TO PARTICLE ORIENTATION

by

Joseph Robert O'Brien
Bachelor of Science, Millersville University, 2013

A Thesis

Submitted to the Graduate Faculty

of the

University of North Dakota

in partial fulfillment of the requirements

for the degree of

Master of Science

Grand Forks, North Dakota

August
2016

This thesis, submitted by Joseph Robert O'Brien in partial fulfillment of the requirements for the Degree of Master of Science from the University of North Dakota, has been read by the Faculty Advisory Committee under whom this work has been done and is hereby approved.

_____
Michael Poellot

_____
David Delene

_____
Cedric Granger

This thesis is being submitted by the appointed advisory committee as having all of the requirements of the School of Graduate Studies at the University of North Dakota and is hereby approved.

_____
Grant McGimpsey
Dean of the School of Graduate Studies

_____
Date

PERMISSION

Title	Sensitivity of Two-Dimensional Stereo (2DS) Probe Derived Parameters to Particle Orientation
Department	Atmospheric Science
Degree	Master of Science

In presenting this thesis in partial fulfillment of the requirements for a graduate degree from the University of North Dakota, I agree that the library of this University shall make it freely available for inspection. I further agree that permission for extensive copying for scholarly purposes may be granted by the professor who supervised my thesis work, or in his absence, by the Chairperson of the department or the dean of the School of Graduate Studies. It is understood that any copying or publication or other use of this thesis or part thereof for financial gain shall not be allowed without my written permission. It is also understood that due recognition shall be given to me and to the University of North Dakota in any scholarly use which may be made of any material in my thesis.

Joseph Robert O'Brien

7 July 2016

TABLE OF CONTENTS

LIST OF FIGURES

LIST OF TABLES

ACKNOWLEDGEMENTS

I would like to thank my advisor, Professor Michael Poellot, and other committee members, Drs. David Delene and Cedric Granger, for their guidance and assistance though the course of this thesis work. I also thank my family for their love and support. This thesis would not be possible without it. I would also like to thank my friends and fellow graduate students who provided relief and helped mold my graduate experience. I would also like to thank Andrea Neumann for countless assistance and advice during this process.

ABSTRACT

Information on the size distribution, orientation and the axial ratio of ice particles is important for the improvement of precipitation retrievals by polarized radar. However, uncertainty in the natural particle orientation and axial ratios remains due to the difficulty in obtaining *in situ* observations of these parameters. This difficulty arises because of possible re-orientation of particles by airflow around aircraft sampling instrumentation. Due to this possible re-orientation, observations of ice particles become a function of the viewing angle of the sampling instrumentation. The two-dimensional stereo (2D-S) optical array probe (OAP) manufactured by SPEC, Inc. offers the capability for comparison between two orthogonal sample volumes (vertical and horizontal) and the determination of whether previously unknown errors in particle image aspect ratio, size distribution and other derived parameters arise due to the viewing angle of imaging instruments.

To further understand the effect of particle orientation on OAP measurements, microphysical data collected with the University of North Dakota Citation II research aircraft during the Integrated Precipitation and Hydrology Experiment (IPHEx) and Olympic Mountain Experiment (OLYMPEx) are analyzed. Planar and columnar type ice crystals have been previously shown to fall with their broad face horizontal. However, 2D-S measurements of aspect ratios indicate a preferred vertical orientation of these particles within the sample volume

of the instrument. Analysis of the effects of this orientation suggest that planar crystals are under-represented, and under sized, within OAP measurements.

CHAPTER I

INTRODUCTION

Motivation

Mid-latitude precipitation is the product of the Wegener-Bergeron-Findeisen process, which involves the growth of ice particles at the expense of liquid droplets in mixed-phase clouds (i.e. consisting of both liquid droplets and ice particles) (Rodgers and Yao 1989). Since the equilibrium vapor pressure is lower for an ice surface than that of a liquid, the mixed-phase cloud environment promotes the rapid growth of ice crystals through diffusion of evaporating liquid droplets (Sulia and Harrington 2011). The growth mechanisms of ice hydrometeors (e.g. diffusional growth, accretion, aggregation) result in the formation of particles with greater mass, area, and fall velocities than the initial cloud particles. As these particles fall they experience melting and evaporation. Depending on the temperature structure of the lower troposphere, these particles may fully transition to liquid within the melting layer or fall to the ground as mixed precipitation and snow. Continental precipitation type and rates are therefore influenced by the size distribution, concentration, and habit of ice particles within the cloud environment. Thus, in order to have accurate global estimates of precipitation from remote sensing systems, an understanding of ice particle sizes, concentrations, and habits is required.

The majority of measurements taken to describe the precipitation and radiative processes of the atmosphere are through ground- and space-based, active and passive remote sensing. To increase the accuracy of ice particle representation in cloud environments, improvement of remote sensing techniques that retrieve cloud microphysical properties are needed. The Global Precipitation Measurement (GPM) satellite was launched in February 2014, as a joint project between the National Aeronautics and Space Administration (NASA) and Japan Aerospace Exploration Agency (JAXA) in order to accurately measure global rain and snowfall amounts. The GPM satellite contains precipitation radars Ka-band (35.5 GHz) and Ku-band (13.6 GHz), which provide the capability to distinguish the phase and orientation of a hydrometer (Hou et al. 2014). The determination of the orientation and phase of a hydrometeor is accomplished through analysis of polarimetric radar parameters such as effective radar reflectivity, differential reflectivity and depolarization ratio. However, there continues to be uncertainty in remote sensing measurements due to multiple scattering from ice particles. This uncertainty is due to the variety of ice particle habits and the non-spherical nature of these particles that prohibits the use of a single theory to describe their scattering behavior (McFarquhar et al. 1999). Ice particles have also been known to increase radar backscatter compared to that which is expected from spheres of the same mass (Marchand et al. 2013). Increased radar backscatter is due to the non-spherical nature of these particles (i.e. larger backscattering cross-sectional area than spheres of the same mass), as well as the variable ice particle density with size. Additionally, ice particles oriented perpendicular to the incident radar beam have a greater chance of enhancing backscatter than randomly oriented particles (Marchand et al. 2013). Thus, the relationship between ice particle radiative and microphysical properties needs to be improved upon. In order to improve

the representation of cloud environments from ground- and space-based remote sensing platforms, bulk ice microphysical properties are needed to describe physical characteristics such as precipitation rates and ice content within cloud as well as radar-derived properties (Heymsfield et al. 2004). For polarimetric radar, knowledge of the size distribution (i.e. number concentration as a function of particle size), axis ratio (i.e. the ratio of the width to the length of a particle), and orientation of ice particles can improve the interpretation of returned power to the radar (Schefold et al. 2002). Knowledge of the habit, size and axis ratio of ice particles is also important in order to describe the fall velocity and orientation of these particles, which are used to calculate vapor deposition, accretion and aggregation rates in modeling precipitation processes (Schefold et al. 2002; Sulin and Hurrington 2011). Therefore, it is necessary to have accurate measurements on the size, habit, axis ratios, and concentration of ice particles in order to accurately describe cloud microphysical properties.

Optical Array Probes

In situ measurements of cloud microphysical properties can be made with airborne probes, such as optical array probes (OAPs), to gain insight into cloud properties that cannot be resolved from remote-sensing platforms. Particle size distributions (PSDs), or the number concentration of particles as a function of size, can be derived from OAP measurements. OAPs produce shadow images of particles passing through a high-intensity, helium-neon light beam that illuminates a linear array of photodetectors (Knollenberg 1969). If a particle passes through the light beam within the sampling area, such that a minimum threshold detection voltage is reached, particle size is inferred from the number of diodes occulted (Knollenberg 1969). OAPs,

and imaging systems in general, are capable of measuring a large size range of particles since the depth of field (i.e. the distance away from the object plane that particles are detected) varies with the square of the particle diameter (Knollenberg 1969). The depth of field allows for the sampling volume to always increase with increasing particle size, which compensates for the decrease in concentration of larger particles (Knollenberg 1969). There is however an inherited problem with OAPs, which have been known to produce erroneous PSDs due to the dependence of measured particle size on the position of the particle within the sample volume (Korolev 2007). Erroneous PSDs are primarily due to large counting and sizing errors that occur when particles pass outside the optical depth of field, as well as, slow response time of the photodiode array and amplifier (Lawson et al. 2006). These sizing and counting errors can lead to potential order-of-magnitude errors in PSDs of particles less than approximately 100 μm (Lawson et al. 2006). Additionally, due to the slow response time and effective pixel size of older OAPs, there is not sufficient resolution to determine the shape and phase of most particles less than three hundred μm (Lawson et al. 2006). To correct for these issues, a new OAP was developed by Stratton Park Engineering Company (SPEC) called the two-dimensional stereo optical array probe (2DS OAP). The 2DS consists of two lasers that cross at right angles. These orthogonal lasers illuminate two linear 128-photodiode arrays, which produce an effective pixel size of roughly ten microns (Lawson et al. 2006). The overlap region of the two lasers allows for a region where particle images are orthogonal, and allows for determination of the distance to either object plane (Lawson et al. 2006). This allows for correction of the depth of field and sample volume effects, improving measurements of particle concentration (Lawson et al. 2006). The improved time response of the 2DS has also helped to improve measurements from another

inherit issue with OAPs, and airborne instruments in general, which is particle shattering. Ice particle shattering on the tips of OAPS can lead to errors in PSDs through the production of small ice artifacts (Lawson 2011). Generally, modified probe tips and post-processing rejection of particles based on particle arrival time, or time a particle takes to transit across the photodiode array, have been used to limit particle shattering. The 2DS may have a more effective particle arrival time algorithm due to faster time response and greater size resolution of the instrument, allowing it to better reproduce instances of particle clusters, which is indicative of particle shattering (Lawson 2011).

Ice Microphysical Properties

Bulk ice microphysical properties are calculated from OAPs through the relation of particle dimension to ice particle mass (m). If the ice particle is one of the regular types of habits (e.g. plates, columns, dendrites, needles, etc.) found in the atmosphere, the projected area of the particle and assumed bulk ice density provide information on the effective density of the ice particle (Heymsfield et al. 2004). Effective density is defined as the ice particle mass divided by the volume of an equivalent diameter sphere, where diameter is equal to the maximum particle dimension (D) (Cotton et al. 2012). Effective density, as described in Cotton et al. (2012), allows for ice particle mass to be expressed as a power law, where:

$$M(D) = \frac{\pi}{6}\rho_{ice}D^3 \ . \qquad (1)$$

If effective density is assumed to be proportional to some power of the particle dimension, the ice particle mass can be expressed in a more generalized form:

$$M(D) = aD^b \ , \tag{2}$$

where a and b are constants (Cotton et al. 2012). Equation 2, known as a mass-dimensional (M-D) relationship, has specific values of b corresponding to various habits of ice particles. As described in Heymsfield et al. (2004), values for b have been extensively studied in earlier studies through different methods, such as ice particle melting, direct comparison with an evaporative measurement, and projected area relationships. The bulk ice water content (IWC) is obtained by integration of the PSD assuming the M-D relationship, such that IWC is expressed as:

$$IWC = \int_0^{D_{max}} N(D)\, m(d)\, dD \ , \tag{3}$$

where N(D) is the size-dependent concentration (Cotton et al. 2012; Heymsfield et al. 2004). In order to obtain better estimates of ice microphysical properties from ground- and space-based remote sensing platforms, improved relationships between in-situ bulk microphysical parameters and radar observations (e.g. radar reflectivity) are needed. However, in order to improve the relationship between bulk microphysical parameters and radar observations, better representation of ice particle mass through M-D relationships is needed.

Recently, there has been some question as to which particle image dimension should be applied to define the diameter of a particle, which affects the sizing of particles within PSDs and derived microphysical parameters. Hogan et al. (2012) shows that using the maximum dimension leads to an overestimate of effective radar reflectivity (Z_e) by 3.7 decibels (dB), compared to using the mean diameter when applied to the widely used Brown and Francis (1995) M-D relationship. In order to better represent the scattering of ice particles, recent studies have

represented ice particles as horizontally oriented oblate or prolate spheroids with a fixed axis ratio (Hogan et al. 2012; Matrosov et al. 2005a). Axis ratio is defined to be the ratio of the width to the length of a particle. Using the horizontally oriented oblate spheroid method, with a constant axis ratio of 0.6 and applying the Brown and Francis (1995) mass-dimensional relationship, Hogan et al. (2012) was able to predict Z_e to within 1 dB for single phase ice clouds. However, Hogan et al. (2012) indicated that there is evidence of deviations from the fixed value of axis ratio for individual aircraft runs. Additionally, Hogan et al. (2012) does not include measurements taken within mixed-phase environments, where the presence of supercooled liquid droplets would substantially increase the vapor diffusion to ice particles, creating ice particles of larger sizes and more extreme axis ratios (Sulia and Harrington 2011). Measurements of axis ratio are needed in order to accurately describe not only the scattering properties of ice particles, but also particle fall velocity, and growth rate. An assumption of constant axis ratios may not be adequate to accurately describe these processes. Thus, there is a clear need for in-situ measurements of ice particle axis ratio, for a variety of particle habits.

Ice Particle Aspect Ratio

Unfortunately, it is difficult to obtain in-situ measurements of the axis ratio of ice particles without affecting the sample. Korolev and Issac (2004) studied a large dataset of particle images obtained with the Cloud Particle Imager (CPI) probe in order to determine the frequency and aspect ratio of particles within ice clouds. Aspect ratio is defined as the ratio of width to length *of an image*, and can be used to infer the intrinsic *particle* axis ratio. The CPI probe records high-resolution digital images of particles by utilizing a high-powered pulsed laser

with a digital charge-coupled device (CCD) camera having 1024 x 1024 pixels, and pixel resolution of 2.3 μm (Korolev and Issac 2004). The study found that the most frequent particle can be described as irregular with an aspect ratio of 0.6 and that the aspect ratio of particle images would be a function of the viewing angle. The aspect ratio found within Korolev and Issac (2004) was the justification for using an axis ratio of 0.6 in the Hogen at el. (2012) study. However, the intrinsic axis ratio of the particle is unknown from CPI measurements due to the reorientation of particles within the sample tube. Due to the deceleration of particles within the sample tube, it is unlikely that ice particles are viewed from the side such that the width of a particle can be measured; thus, the true axis ratio is unknown. Measurements of particles within the free-stream atmosphere are needed in order to accurately determine the axis ratio of ice particles.

In-situ observations of ice particle axis ratio are difficult to obtain due to the re-orientation of particles by turbulence introduced by the presence of the aircraft. Thus, it is often assumed that OAPs are not coupled to the atmosphere and the orientation of particles within the sample volume of OAPs is random. Thus, information on properties such as axis ratio are unavailable (Hogan et al. 2012). King (1986) studied the air flow and particle trajectories around sampling aircraft in an attempt to find justification for observations showing a preferred orientation of ice columns measured by the two-dimensional cloud probe (2DC OAP). The preferred orientation of columns sampled in King (1986) were roughly 60° off horizontal. Any preferred orientation is significant since any rotation of crystals around the viewing plane will result in possible errors in PSDs and derived quantities King (1986). King (1986) found that for most ranges of aircraft sizes, sampling speeds, and range of interest in crystal sizes, there was

sufficient aerodynamic torque to align particles along the direction of instantaneous drag, with effects maximized near wing tips for wing mounted probes. The instantaneous drag is the result of the relative change of the air velocity in the orthogonal directions (e.g. along direction of flight and across direction of flight) ahead of the sampling location (MacPherson and Baumgardner 1988). MacPherson and Baumgardner (1988) studied this instantaneous drag ahead of the King Air wingtip-mounted OAPs with the use of a Rosemount 858 five-port differential pressure flow-angle sensor placed inside one of the probe canisters. MacPherson and Baumgardner (1988) found significant flow deceleration within one meter ahead of the probe due to a combination of effects from the wing, pylon and probe canisters themselves. Additionally, MacPherson and Baumgardner (1988) found a 3 ° sideslip angle difference between the inboard and outboard sampling locations due to vortex shredding associated with the wingtip. MacPherson and Baumgardner (1988) concluded that the combination of flow disturbances can cause distortion in the 2-D images of the particles and errors in the measured concentrations, sizing of particles from 2-D images, and quantities derived from calculated PSDs.

An estimate of the flow-induced errors may be possible if multiple OAPs were flown in the same sampling location, in different orientations, to account for possible reorientation of particles. OAPs have been historically oriented vertically (i.e. orthogonal to the ground; projects images onto the x-z plane), since ice particles, depending on habit, are known to fall with their major axis horizontally. This allows for the broad face (i.e. largest area) of the particle to be sampled by the OAP, assuming the particle maintained its natural orientation. Horizontally oriented OAPs would allow measurements of the "side-on" shape of ice particles (i.e. width),

where plates and dendrites would appear as rectangles with the orientation of the particle horizontal in the absence of flow distortion (King 1986). The 2DS now offers the opportunity to measure two orthogonal viewing from the same sampling location for determination of possible particle orientation effects. Assuming no distortion of flow from the aircraft, particles should be preferably oriented within the vertical 2DS array, such that the broad face of particles (i.e. Asp ~ 1.0) are sampled. This situation would allow the horizontal 2DS array to presumably sample the thickness of these particles (i.e. Asp << 1.0). This situation would also allow estimates to be made about the mean axis ratio of these particles, since the major and minor axes are viewed within the orthogonal photodiode arrays.

Objectives

The objective of this study is to determine if there are possible orientation effects within the sample volumes of the two 2DS arrays by comparison of aspect ratio measurements. Possible effects of airflow are to induce a preferred orientation of particles, to randomly re-orient particles, or to have no effect on the particle orientation. Possible orientation effects of the probe are determined by analyzing 2DS images of ice particles that are known to have a free-stream, preferred falling orientation. Previous research on horizontally oriented ice particles has been conducted in order to describe a variety of atmospheric phenomena. Theoretical calculations have described the orientation of planar and columnar ice crystals, which were determined to fall in a preferred horizontal orientation within a range of Reynolds number ($0.39 < Re < 80$) with oscillations not existent at this range of Reynolds numbers. (Cho et al. 1981; Bréon and Dubrulle 2004). List and Schemenauer (1971) calculated the Reynolds numbers for planar and columnar

models through fluids of known viscosity, and found that these particles are within a stable horizontal free-fall until Reynolds numbers greater than 200, where secondary motions cause the models to oscillate. Additionally, zenith- and nadir-pointing Doppler LIDAR measurements have observed enhanced backscatter due to horizontally oriented plates within the atmosphere (Marchand et al. 2013; Westbrook et al. 2009). The contamination of CALIPSO (Cloud-Aerosol Lidar and Infrared Pathfinder Satellite Observations) ice cloud microphysical retrievals, due to specular reflection from horizontally oriented planar crystals, was so significant that the LIDAR was moved to 3° off-nadir to reduce the contamination (Marchand et al. 2013). Independent confirmation of the presence of these particles within the atmospheric environment is needed in order to determine orientation effects within the 2DS. Analysis of CPI image data from the Integrated Precipitation Hydrology Experiment (IPHEx) determines when periods where planar and columnar ice crystals were observed. Analysis of 2DS aspect ratio measurements in these periods determines the orientation of particles within the sample volume. Comparison analysis of the PSDs from the 2DS arrays determines possible bias in the sizing of particles due to the effects of orientation. Calculation and comparison of derived quantities such as ice water content and effective radar reflectivity determine effects of orientation on derived mass-related quantities.

CHAPTER II

METHODOLOGY

Project Overview

Two NASA Global Precipitation Measurement (GPM) ground validation missions, IPHEx (Integrated Precipitation and Hydrology Experiment) and OLYMPEx (Olympic Mountain Experiment) had the purpose of validating and verifying precipitation measurements from the GPM satellite constellation. Validation and verification of precipitation measurements is achieved by collocating and comparing measurements from in-situ aircraft, ground based multi-band radars, and the GPM core observatory in order to obtain horizontal and vertical profiles throughout the region of interest. Additionally, ground validation missions allow for improved physical understanding of meteorological conditions and the creation of algorithms needed for future remote sensing applications. IPHEx was a ground validation mission conducted in North Carolina during the summer of (i.e. May – June) 2014. The project was designed to determine the relationship between precipitation and hydrologic processes in regions of complex terrain. With this focus of research in mind, the project was centered in the Appalachian Mountains and the Piedmont and coastal regions of North Carolina. Due to a lack of precipitation over the Appalachians during the project period, the majority of measurements

were obtained in the Piedmont and coastal region, with a number of flights off-shore. Since the atmospheric environment was dominated by convective forcing, flight profiles often included stacked legs (i.e. level flight legs at multiple altitudes) in regions of organized, non-severe convection. OLYMPEx was a validation mission conducted in Washington during November and December 2015. The project was designed to measure the evolution of frontal systems from the Pacific Ocean into the Olympic Mountains. Therefore, samples were obtained over the Olympic Mountains and off the coast of Washington during pre- and post- frontal passages. Flight profiles during this mission include stacked legs at radials of ground radars and constant bank angle spirals over these radars. In stark contrast to IPHEx, the more benign atmospheric environment during OLYMPEx allowed for extended periods within cloud, at multiple altitudes, and provided immense amounts of precipitation sampling over the scientific research area.

Citation II Overview

The platform used to obtain in-situ cloud measurements during IPHEx and OLYMPEx was the University of North Dakota Citation II Atmospheric Research aircraft (UND-Citation II). This aircraft has been modified for atmospheric research and is capable of providing in-situ aerosol and cloud microphysical measurements at altitudes from near the surface to 13 km. The aircraft has been modified to provide instrument sampling locations close to free-stream, undisturbed airflow. UND-Citation II modifications include: pylons underneath the wings to

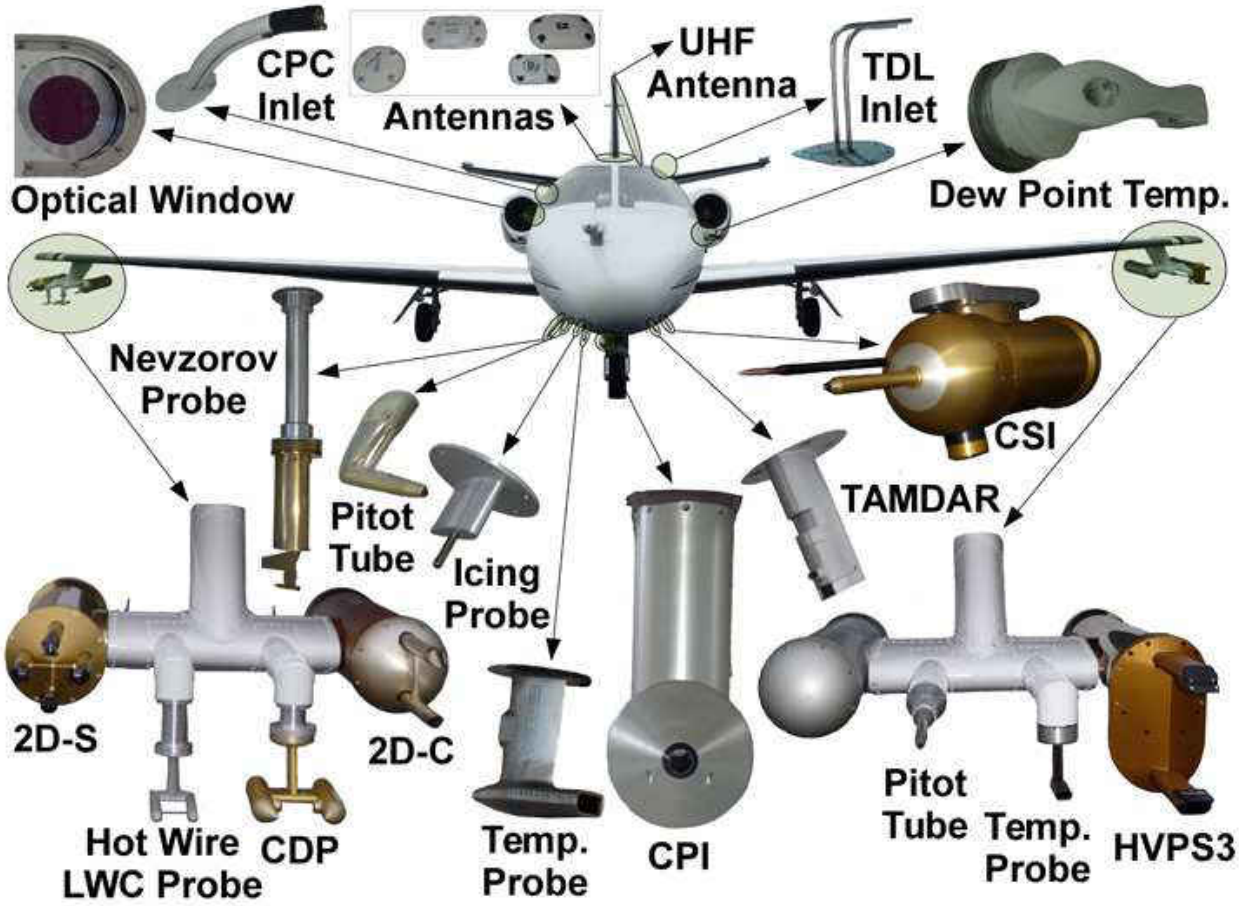

Figure 1: This figure shows the configuration of the University of North Dakota Citation II Research Aircraft for the Integrated Precipitation and Hydrology Experiment (IPHEx).

allow for mounted instruments, a nose boom extending from the aircraft nose for wind and pressure measurements ahead of the aircraft, and multiple fuselage modifications to accommodate instruments that may exceed the weight and size limits of other areas. Various configurations of instruments are possible and depend on the research interests of the project. For instance, the instrument configuration for IPHEx is shown in Figure 1. The 2DS was added to the outboard pylon underneath the right wing of the UND-Citation II before the start of the project. The outboard pylon location of the 2DS allows not only for comparison with the Cloud Droplet

Probe (CDP), King Liquid Water Content Probe (King-LWC), but also with the Two-Dimensional Cloud Probe (2DC) OAP. The instrument configuration for OLYMPEx is nearly identical to the configuration for IPHEx, except for the inclusion of a second SPEC High Volume Precipitation Spectrometer Version 3 (HVPS-3) on the inboard pylon, underneath the left wing. The second HVPS-3 was included in order to obtain measurements in an orthogonal direction from the HVPS-3 on the outboard pylon, which is very similar to the 2DS design. Instruments that measure standard atmospheric environmental variables (e.g. temperature, dew point, pressure-altitude, GPS position, three-dimensional winds) are always included within the project configuration, along with the data acquisition system, the Scientific Engineering Associates (SEA Inc.) M-300. The M-300 allows for real time data acquisition and calculations of physical parameters such as true airspeed (i.e. airspeed corrected for temperature and altitude), liquid water content (LWC) and IWC. True airspeed (TAS) is a critical parameter for OAP measurements, since the sample volume is dictated by the TAS of the aircraft and affects particle images, sizing, and concentrations. The M-300 calculates TAS in real-time, and transmits this parameter to the OAP located on the wingtips. All instrument data acquired by the M-300 are saved in a binary formatted file (*.sea). Each of the SPEC instruments (e.g. 2DS, HVPS-3, CPI) record data on their own Windows XP computers.

Airborne Data Processing and Analysis Software Package

In order to quality control and assure data collected with the UND-Citation II in a timely matter, the Airborne Data Processing and Analysis Software Package (ADPAA) is used to post-process the M-300 data files (Delene 2011). ADPAA allows for fully automated processing of

airborne data, with the creation of processed, preliminary data files for quick analysis hours after a flight. A fully automated process allows airborne scientists to check instrument status between flights, which offers a measure of quality control for the dataset. ADPAA processing is split into four different processing levels: binary into analog measurements, analog into base physical measurements, base physical measurements into project-desired physical measurements, and collection/calculation of physical measurements from different measurement platforms. The first level converts the saved binary data from the M-300 into analog measurements (i.e. voltages and resistances). The second level converts these voltages into physical measurements, such as temperature and pressure, which are used within the third level to calculate project-oriented physical parameters, such as LWC and IWC. The fourth level combines physical parameters from multiple data acquisition systems, such as the M-300 and a particle counter. After each of these processing levels is completed, a summary file for the project at hand is created, pulling data from each instrument file desired into one file. Each flight is analyzed after a project to quality assure the data, which involves removing any data deemed to be invalid and applying a parameter specific missing value code for that time frame.

The data obtained during IPHEx (OLYMPEx) with the UND-Citation II and processed with the ADPAA software on 24 April 2016 (26 April 2016) is used to describe the cloud environment during areas of interest. Of particular interest to this study are the temperature and relative humidity of the cloud environment, as these are two of the main factors that determine ice particle habit, or type. Additionally, understanding the GPS position, altitude, angle of attack and sideslip angle gives insight into how measurements were obtained with the Citation. The orientation of the aircraft when measurements are being obtained is important in understanding

possible airflow effects on observed particle orientation. Additionally, since the TAS sent to the SPEC probes during flight is not recorded by the OAPs, a quality-assured TAS is needed for post-processing the OAP data.

Software for OAP Data Analysis Version 2

The data collected with the 2DS and HVPS-3(s) during IPHEx and OLYMPEx were processed with software called Software for OAP Data Analysis – Version 2 (SODA2). The software was developed by Aaron Bansemer at the National Center for Atmospheric Research (NCAR), and was used to calculate particle size distributions and IWC for IPHEx and OLYMPEx. Within the SPEC data acquisition software, the data from the primary and secondary photodiode arrays are stored within binary data buffers and include metadata (e.g. particle arrival time and specific photodiode identification). For both IPHEx and OLYMPEx, the 2DS was positioned on the outboard, right wing pylon such that the primary photodiode array was aligned orthogonally to the ground and the secondary photodiode array parallel to the ground. For the rest of this study, the primary photodiode array will be referred to as the 'vertical' photodiode array (i.e. 2DS-V), while the secondary photodiode array will be referred to as the 'horizontal' photodiode array (i.e. 2DS-H). SODA2 is designed to process each photodiode array separately,

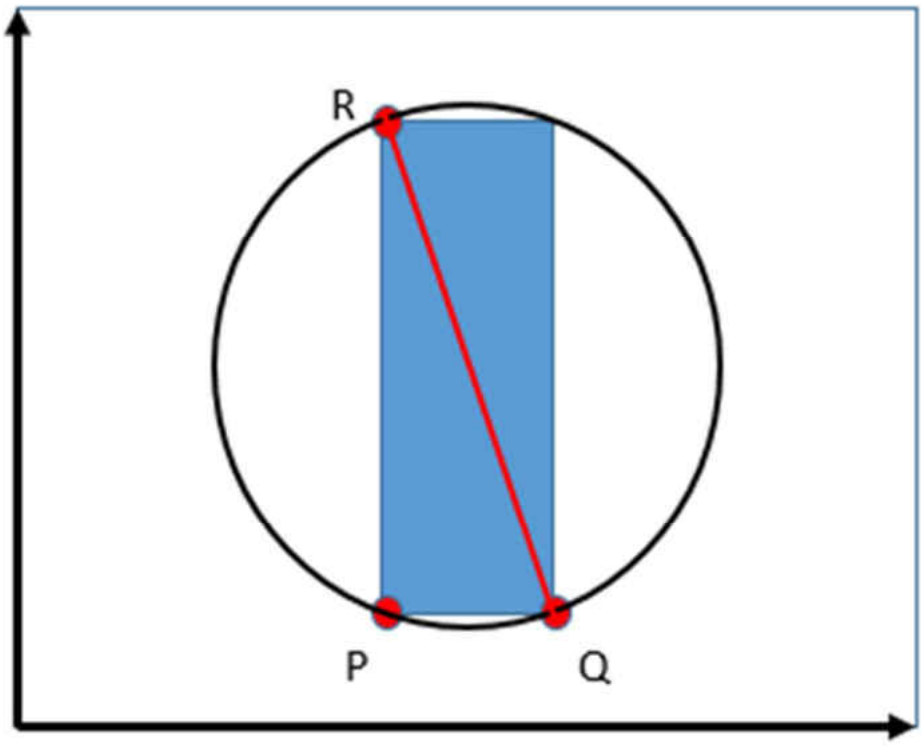

Figure 2: This figure shows an example of the SODA2 circle fit method of an artificially created 'column' particle image. Each of the three red points within the image correspond to points P,Q,R that define the circle. The red line corresponds to diameter of the minimum bounding circle.

and at this time, stereo images (images within both photodiode arrays) are unavailable. The standard SODA2 processing method used within this study is called the 'circle fit method', and is shown in Figure 2. For each particle image within a data buffer, the circle fit method sizes particles by enclosing each image with the smallest possible circle. The diameter of the particle image is then defined as the diameter of the bounding circle. The bounding circle is defined by the three points (*P*, *Q*, and *R*), which form a triangle with acute angles. Since these three points lie on the circle and are equal distance to the center, the center of the bounding circle is found by

calculating the midpoints of the *PQ* and *QR* cords. The center of the bounding circle is perpendicular from each of these cord midpoints. The radius of the bounding circle is then found by calculating the distance from the center of the circle to one of the three points, *P*, *Q*, or *R*. In order to find the aspect ratio of the image, the major and minor axis of the particle image must be found. The major axis is found by determining the maximum distance of a line going through two points of the particle image, where these two points are found by bisecting the vertex of *PQR* (vertex is smallest angle). The minor axis of the particle image is defined as the summation of maximum distance of the particle image from both sides of the major axis. Aspect ratio is then found by calculating the ratio of the minor to major axis of the particle image. The area ratio of the particle image is found by calculating the ratio of the area of the particle image to the area of the bounding circle. Additionally, cross-sectional area is found by multiplying the area of the particle image by the resolution of the probe, which is 10 microns for the 2DS. In order to calculate the canting angle, or angle from the axis in the direction of flight, the angle between the major axis of the particle image and the y-axis is found. The data are stored within an Interface Definition Language (IDL) structure, where each parameter is stored within a multi-dimensional array of particle counts per time and size bin (size bin variation is based on the parameter in question). Parameters, such as particle concentration, are then found by taking the particle number distribution (i.e. number of particles within a certain size bin) and multiplying by the bin width. Particle images are created by printing data buffers to a file, with the option of printing every buffer or the first buffer of each second within a minute. The latter option is used in this study to select particle images from the HVPS-3 and 2DS that communicate predominate habit and orientation.

Case Selection

In order to determine the possible orientation of particles within the IPHEx and OLYMPEx datasets, cases need to be selected for periods where naturally orientated particle habits were sampled. As discussed in the introduction, plates, dendrites, columns and needles have been shown to be horizontally oriented within the atmosphere. Analysis of how these particles are oriented within the 2DS measurements will determine the possible re-orientation of particles. Review of the 2DS particle images will give a clear indication of the orientation of these particles and determine the category of possible orientation for each case. As discussed previously, the categories of possible orientation due to airflow effects are: no reorientation of particles, random orientation of particles, and preferred particle orientation. Cases are determined through extensive search of science notes taken by instrument operators during each flight. These notes are taken to describe the sampled atmospheric environment, including information on the predominant particle habit, LWC, temperature, and location of the aircraft within its current sampling leg. Review of these flight notes determines time periods where the particles of interest were observed. Additionally, CPI images are reviewed in order to independently confirm the existence of these particles within the specified time period. If the specified time period does not include the entire level flight segment to which it corresponds, CPI images from the entire flight leg are reviewed in order to confirm the full time period these particles are found to existence. After the particles of interest have been independently confirmed, 2DS-V and 2DS-H particle images are reviewed for the entire period in order to determine possible orientation effects. Additionally, 2D-C and HVPS-3 images are reviewed in order to determine if any of the

orientation effects observed on the 2DS also occur on these probes. For each of these time periods, analysis of derived size and mass parameters provides insight the possible effects of particle orientation on 2DS measurements.

Analysis

Visual inspection of particle images allows for possibility to determine the possible orientation of particles within the sample volume. A quantitative means of describing the possible orientation effects not only helps with explaining the phenomena, but allows for understanding of how the possible orientation affects derived parameters. This study will use multiple parameters to quantify and determine possible orientation effects. The parameters include aspect ratio, area ratio, and canting angle. Aspect ratio will be used to determine the orientation of the broad side (i.e. face of the particle with largest cross-sectional area) of the particle. For example, if there is no orientation of particles such that a dendrite where to pass through the sample volume of the 2DS horizontally, the particle would be viewed as a sliver, or rectangle, within the 2DS-H array. Within the 2DS-V array, the majority of the dendrite would be viewed. In terms of aspect ratio, the broad face of the dendrite would have an aspect ratio very

close to 1, while the side view of the particle would be much less than 1. Plots of aspect ratio as a function of size for both orientations would thus give insight into particle orientation. If there is no orientation, aspect ratio would be much greater within the 2DS-V data than the 2DS-H data. If there was random orientation, there should be no discernable difference within the aspect ratio measurements.

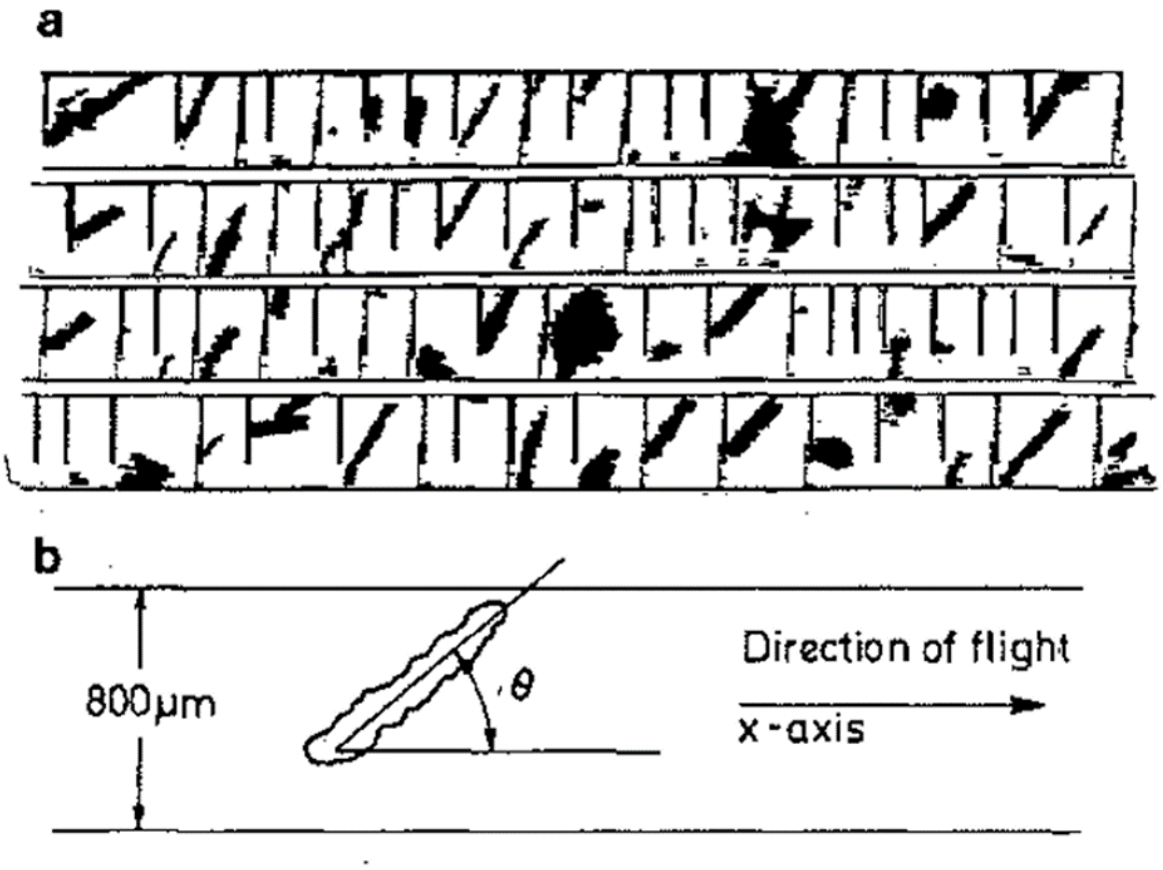

Figure 3: This figure shows the preferred orientation of column particles investigated within the King (1986) study. (a) Particle images obtained with a wingtip, starboard mounted 2D-C. (b) Definition of canting angle defined within the King (1986) study, which is used to describe the preferred orientation of particles. Figure taken from King (1986).

Area ratio measurements will also be used to determine orientation. Area ratio is defined as the number of shaded pixels per particle size for each particle image. Area ratios measurements close to 1 will indicate the broad face (i.e. largest cross-sectional area) of the particle is being sampled, while area ratios much less than one will indicate the side view of the particle is being sampled. While similar to aspect ratio, area ratio measurements are directly used within model parameterizations to calculate particle terminal velocity. Comparison of between the orientations of the 2DS will give insight into possible effects of particle orientation on particle terminal velocity, particle growth rates and precipitation rates. A mathematical means to describe the orientation of particles is comparison of the particle image canting angles. In King (1986), a preferred orientation of columns was found within the 2D-C images obtained with a King Air, as shown in Figure 3. These column images had a canting angle of roughly 60°, which King was able to mathematically reproduce with calculations of streamlines around wings of finite length. Though this observed canting angle was a sampling idiosyncrasy, and not due to a natural preferred falling orientation of these particles, this orientation is critically important. Any rotation of particle image within its frame of reference will cause it to be sized differently from a particle with 0 ° orientation, producing unknown errors in PSDs and derived quantities (King 1986).

Understanding the implications of the determined orientation on derived parameters must be known in order to gain insight into possible error and uncertainty within the measurements. Any potential bias within the parameters will not only affect 2DS measurements, but any relationship derived between the PSDs and remote sensing algorithms. To understand the

implications, comparison of 2DS measurements from both orientations will be conducted over size, mass, and other derived parameters, such as effective radar reflectivity. The comparison of size parameters (mean diameter, median diameter, mean volume diameter, median volume diameter, and effective radius) will give insight into if the observation orientation has an effect on the sizing methods of SODA2. These size parameters are calculated after SODA2, and are based on the parameters described in Theisen et al. (2009). Mean diameter is defined as the average particle diameter within the particle size spectrum, and is calculated by

$$Mean\ Diameter\ (\mu m) = \frac{\sum(D_i n_i dD_i)}{\sum(n_i dD_i)}, \quad (1)$$

where D_i is the midpoint of the *i*th bin in microns, n_i represents the number concentration in the *i*th bin (m^{-4}), and dD_i represents the width of the *i*th bin of the size spectrum in microns. Median diameter is defined as the particle diameter that separates the particle spectrum such that half of the spectrum is composed of smaller particle diameters and half is found within larger diameters. Medium diameter is calculated by

$$Median\ Diameter\ (\mu m) = b_{i^{50\%}} + (\frac{0.5 - cumu_{i^{50\%}-1}}{pro_{i^{50\%}}})(b_{i^{50\%}+1} - b_{i^{50\%}}), \quad (2)$$

where $b_{i^{50\%}}$ represents the first particle size bin that contains greater than 50% of the cumulative distribution; pro_i is the number distribution at the *i*th bin divided by the total number distribution; $cumu_i$ is the sum of pro_i from the first bin to the *i*th bin; and $b_{i^{50\%}+1}$ is one particle size bin larger than $b_{i^{50\%}}$. The mean volume diameter is defined as the mean diameter of the volume distribution and is calculated by

$$Mean\ Volume\ Diameter\ (\mu m) = \left[\frac{\sum(D_i^3 n_i dD_i)}{\sum(n_i dD_i)}\right]^{1/3}. \quad (3)$$

Median volume diameter is similar to the median diameter, but is defined as the particle diameter that separates the particle volume distribution. Median volume diameter is calculated by

$$Median\ Volume\ Diameter\ (\mu m) = b_{i^{50\%}} + (\frac{0.5 - cumu_{i^{50\%}-1}}{pro_{i^{50\%}}})(b_{i^{50\%}+1} - b_{i^{50\%}}), \quad (4)$$

where, in this case, pro_i is the particle volume at the *i*th bin divided by the total volume distribution, and particle volume is calculated by

$$Particle\ Volume\ (\mu m^3) = \frac{4\pi}{3}\left(\frac{D_i}{2}\right)^3 (n_i)\ . \quad (5)$$

Effective radius is a useful parameter used within remote sensing applications in order to determine cloud optical extinction coefficient and is calculated by

$$Effective\ Radius\ (\mu m) = \frac{\Sigma\left[\left(\frac{D_i}{2}\right)^3 n_i\, dD_i\right]}{\Sigma\left[\left(\frac{D_i}{2}\right)^2 n_i\, dD_i\right]}\ . \quad (6)$$

The mass, or ice water content, calculations in this study are completed through two different methods, effective density and mass-dimensional. The effective density method assumes each particle is spherical, and applies a bulk density based on the particle habit and dimension to calculate the mass. Therefore, the calculation of ice water content using the effective density method is then

$$IWC\ \left[\frac{g}{m^4}\right] = Volume\ of\ Bin\ * Bulk\ Density\ of\ Particle * Number\ Concentration\ of\ Bin\ . \quad (7)$$

The calculation of ice water content using the M-D method does not assume spherical particles, and the mass of the particle is related to some dimension of the particle (longest particle

dimension in this study) through the use of previously calculated empirical relationships. Ice water content using the M-D method is calculated by

$$mass_i\ [g] = a\ D_i{}^b$$

$$IWC\ \left[\frac{g}{m^4}\right] = mass_i\ *\ n_i\ , \tag{8}$$

where *a* and *b* are the empirical coefficients relating mass to particle dimension. Effective densities used within this study are listed in Table 1, while M-D relationships are listed in are listed within Table 2.

Table 1: This table contains bulk densities for various ice particles used within ice water content calculations. Based on data of Heymsfield (1972). Diameter range is the range of particle sizes this relationship is valid over.

Crystal Type	**Bulk Density, ρ_c, (g cm^{-3}) d (mm), L (mm)**	**Diameter Range**
Plate	$\rho_c = 0.9$	
Dendrites	$\rho_c = 0.588\ d^{-0.377}$	d ≥ 0.3 mm
Column	$\rho_c = 0.65\ L^{-0.0915}$	L ≥ 0.028 mm

Table 2: This table contains mass-size relationships for various ice particles used within ice water content calculations. The particle dimension used within plate and dendrite (column and needle) calculations is in cm (mm). Diameter range represents the particle size range these relationships are valid for. Based on data from Heymsfield and Kajikawa (1987) and Mitchell et al. (1990).

Crystal Type	**Mass-Size Relation**	**Diameter Range**
Plate	$m\,(g) = 3.76\,x\,10^{-2}\,d^{3.31}\;\;(d = cm)$	0.3 mm ≤ d ≤ 1.5 mm
Dendrites	$m\,(g) = 6.12\,x\,10^{-4} d^{2.29}\;\;(d = cm)$	0.6 mm ≤ d ≤ 5.3 mm
Column	m (mg) = $0.064\,d^{2.6}\;\;(d = mm)$	0.2 mm ≤ d ≤ 0.6 mm
Needle	$m\,(mg) = 0.0049 d^{1.8}\;\;(d = mm)$	0.6 mm ≤ d ≤ 2.7 mm

The last parameter calculated is effective radar reflectivity, which gives insight into how the measured particle size distribution by the 2DS would compare with a remote sensing platform. While this study does not compare with ground, airborne (onboard the NASA ER-2), or space radar measurements, it offers the opportunity to expand the 2DS comparison into terms a wider range of the atmospheric science community are familiar with. Additionally, it offers a glimpse into possible future work comparing with radar observations. Effective radar reflectivity is calculated by

$$Radar\ Reflectivity\ (Z)\ [dBZ] = 10 * LOG\left[\sum {D_i}^6 * n_i * dielectric\ constant\right], \quad (9)$$

where, for S-band radars (2-4 GHz), the dielectric constant assumes spherical particles and is 0.93

CHAPTER III

DATA

Data Overview

Review of flight notes from the IPHEx and OLYMPEx campaigns determined periods where natural horizontally oriented ice particles were observed. These periods were categorized by ice particle habit to determine sensitivity of orientation to habit. Each case occurred during level flight profiles and has an average length of three to four minutes, which corresponds to roughly 19-26 km of cloud measurements at an airspeed of 110 meters per second. The purpose of this chapter is to show select cases for each particle habit and present the total number of cases that will be used within the analysis. For each case, 2DS images are shown from both orientations of the probe. These images display only the first buffer of each second for an entire minute. Additionally, CPI images from the flight leg will be shown. Each image displays a particle size as defined by the maximum dimension of the particle image. Unfortunately, environmental periods where only pristine ice crystals are found are rare. Therefore, the majority of cases within this study contain multiple habits, and are referred to as 'mixed'.

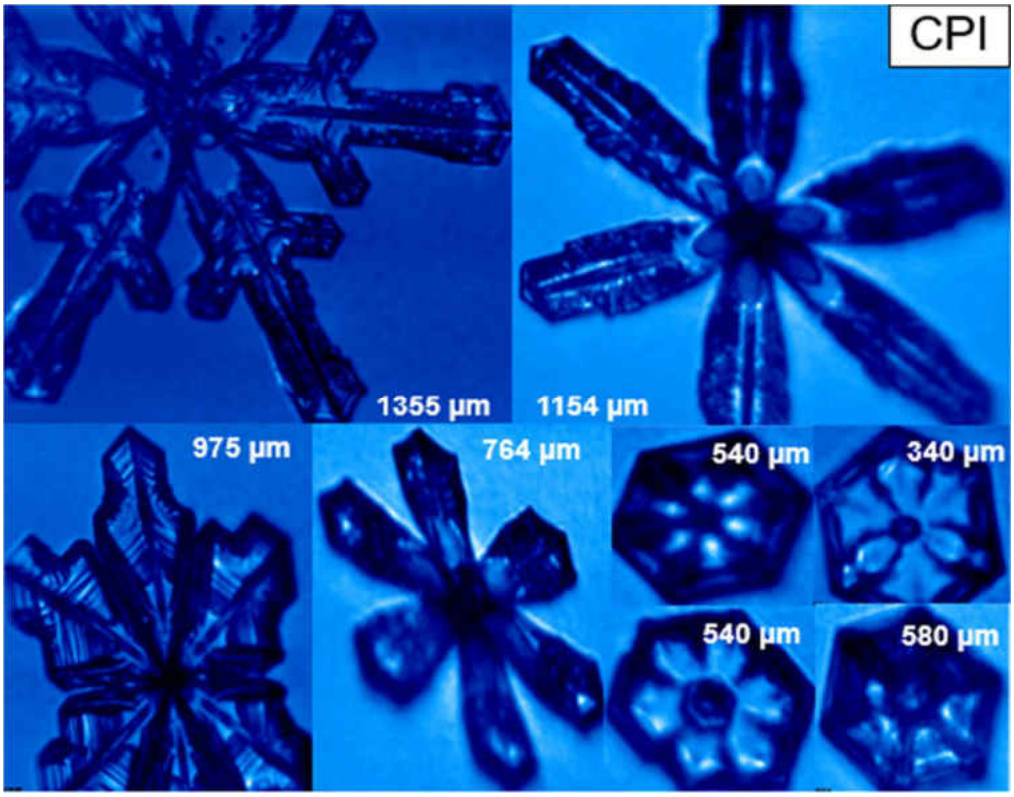

Figure 4: The figure shows CPI images from 23 May 2014, 14:23:00-14:27:00 UTC. The diameter given in the white text is the largest particle image dimension.

Dendrite

Two representative cases for dendrites have been selected. The first, is a four-minute flight leg from the May 23rd 2014 light that consists primarily of dendrites with some small plates (Figure 4). The 2DS images in Figure 5 show a distinct feature for this time period. Dendrites are clearly more distinguishable within the horizontal array of the 2DS compared to the vertical. Images from both orientations of the instrument are from the exact same time period, suggesting that these dendrites are oriented vertically within the sample volume of the instrument. In this instance, the particle images within the vertical array of the 2DS are showing

the side or minor axis of most dendrites. It is interesting to note that within the vertical images, there appears to be a constant canting angle, similar to the images found within Figure 3.

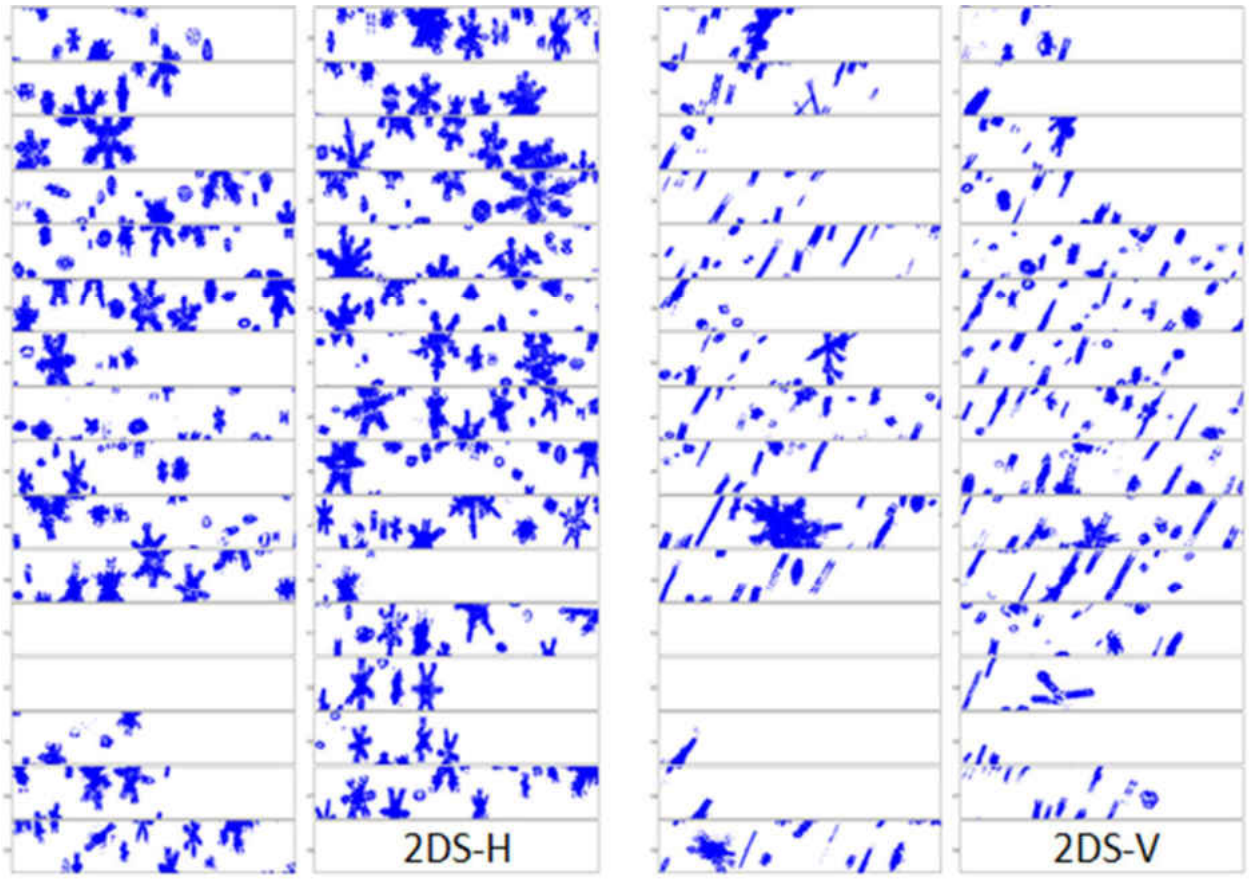

Figure 5: This figure shows 2DS particle images from the 23 May 2014, 14:24:28-14:25:00 UTC. flight. The 2DS-H (2DS-V) image corresponds to the particle images obtained with the horizontally (vertically) aligned probe arm of the instrument. There are 4 columns (two for each 2DS orientation) of particle image buffers. Each row within these columns represent the first buffer for each second of data.

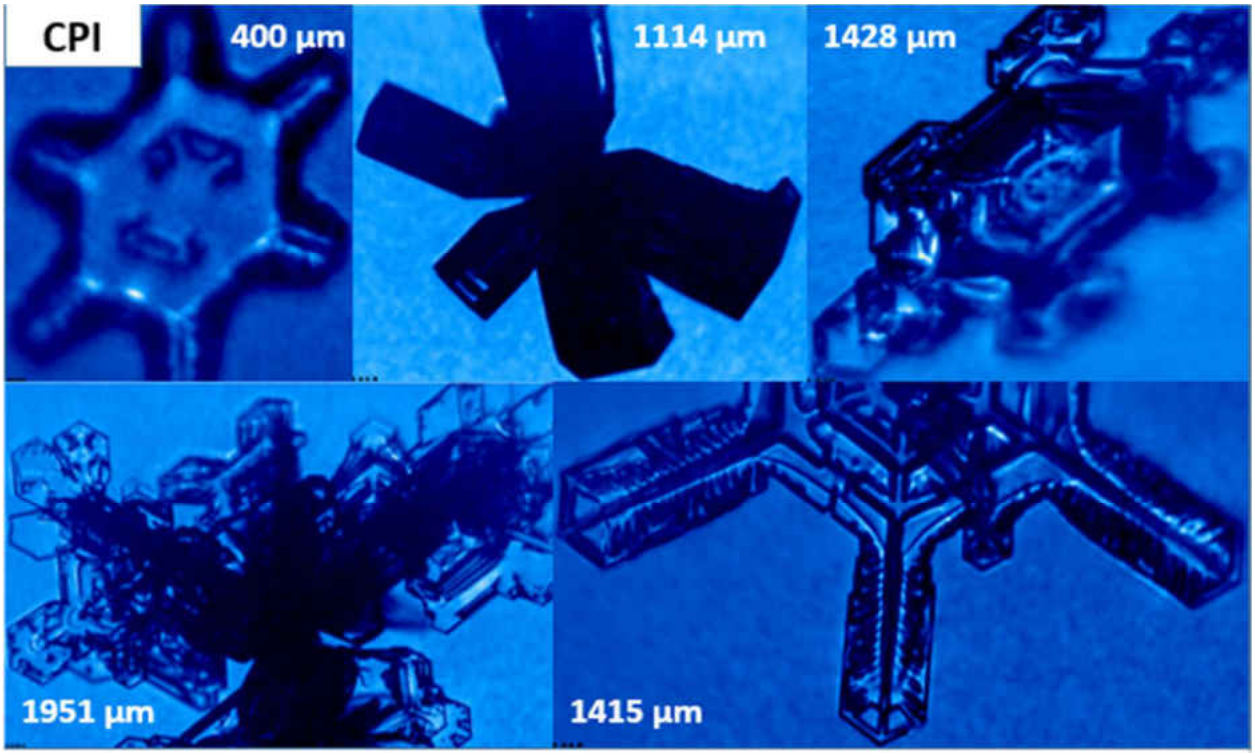

Figure 6: This figure shows CPI images from 12 Nov. 2015, 19:45:00-19:50:00 UTC. The diameter given in the white text is the largest particle image dimension.

The second case is November 12th, 2015 flight and represents the mixed dendrite cases found within this study. The CPI images in Figure 6 indicate that dendrites are present within this environment, along with additional habits. 2DS images (Figure 7) show a variety of particles, a large number of which are indistinguishable and can be classified as having an irregular habit. Dendrites are clearly observed within the horizontal array of the instrument. However, within the vertical array, many long rectangular images are observed with a preferred orientation when dendrites are viewed within the horizontal array. This is consistent with 'side-on' images of dendrites found within the first dendrite case. It should be noted that the irregular

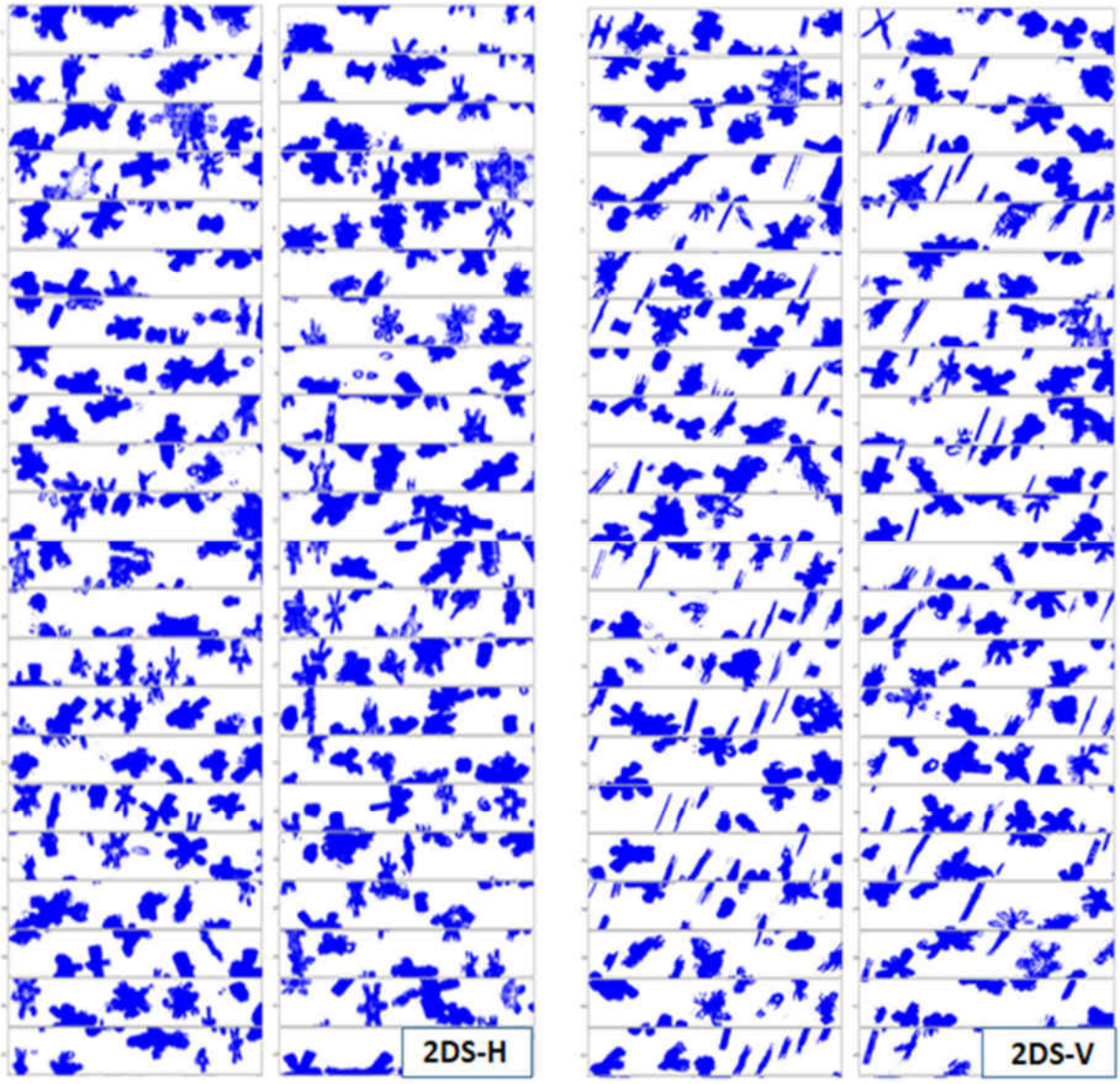

Figure 7: This figure shows 2DS particle images from 12 Nov. 2015, 19:48:00-19:48:43 UTC. The 2DS-H (2DS-V) image corresponds to the particle images obtained with the horizontally (vertically) aligned probe arm of the instrument. There are 4 columns (two for each 2DS orientation) of particle image buffers. Each row within these columns represent the first buffer for each second of data.

particles within both arrays appear to be randomly oriented during this time period, with only the dendrites having a preferred orientation.

The May 23rd, 2014 flight is the best example of preferred orientation of dendrites observed with the 2DS during the IPHEx and OLYMPEx field campaigns. While the November 12th, 2015 flight contains mixed habits, the same preferred orientation of dendrites is found within this flight. Overall, every dendrite case listed in Table 3 has a preferred orientation such that dendrites are vertically oriented within sample volume of the 2DS. There were no instances of horizontal orientation (such that dendrites would be more distinguishable within the vertical array), and no instances of random orientation during periods where dendrites are observed.

Table 3: Dendrite Cases

Project	Flight Date	Start Time	End Time
IPHEx	16 May 2014, 17:00:32 UTC	15:19:00 UTC 14:47:00 UTC	15:21:00 UTC 14:49:00 UTC
	23 May 2014, 13:21:31 UTC	14:22:00 UTC	14:28:00 UTC
OLYMPEx	12 Nov. 2015, 18:49:13 UTC	19:46:00 UTC	19:49:00 UTC
	23 Nov. 2015, 14:49:18 UTC	15:56:00 UTC	16:01:00 UTC
	23 Nov. 2015, 20:23:09 UTC	22:54:00 UTC	22:59:00 UTC
	5 Dec. 2015, 14:17:47 UTC	14:46:00 UTC 16:59:00 UTC 17:05:00 UTC	14:50:00 UTC 17:02:00 UTC 17:08:00 UTC
	12 Dec. 2015, 16:39:54 UTC	18:44:00 UTC 19:18:00 UTC	18:48:00 UTC 19:21:00 UTC
	18 Dec. 2015, 05:24:31 UTC	03:13:00 UTC 03:31:00 UTC	03:16:00 UTC 03:36:00 UTC
Total:	8 Cases	48 Min	

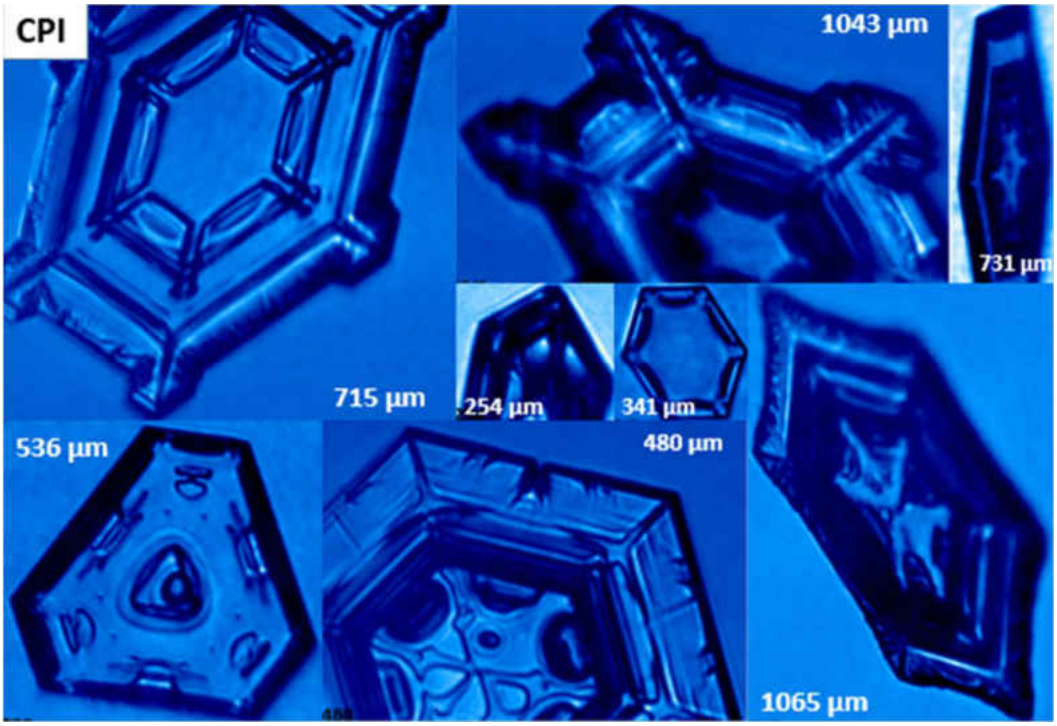

Figure 8: This figure shows CPI images from 25 May 2014, 19:50:00-20:00:00 UTC. The diameter given in the white text is the largest particle image dimension.

Plates

The plate case from May 25th, 2014 flight, along with a majority of plate cases within Table 4, contains large plates (Figure 8) and additional habits. As in the dendrite cases, plates are more distinguishable within the horizontal array of the 2DS compared to the vertical array, as seen in Figure 9. Within the vertical array, particle images are rectangular which is indicative of the 'side-view' or minor axis of the plate. Again, like the 2DS vertical dendrite images, there appears to be a preferred canting angle within the vertical plate images. All of the plate cases within Table 4 appear to have a preferred orientation, such that plates are vertically oriented within the sample volume of the 2DS. There are no environments where plates were equally

represented within both arrays of the 2DS, suggesting that the orientation of these particles is not random. Additionally, there are no periods where plates were more distinguishable within the vertical array of the 2DS, suggesting that there is a re-orientation of these particles.

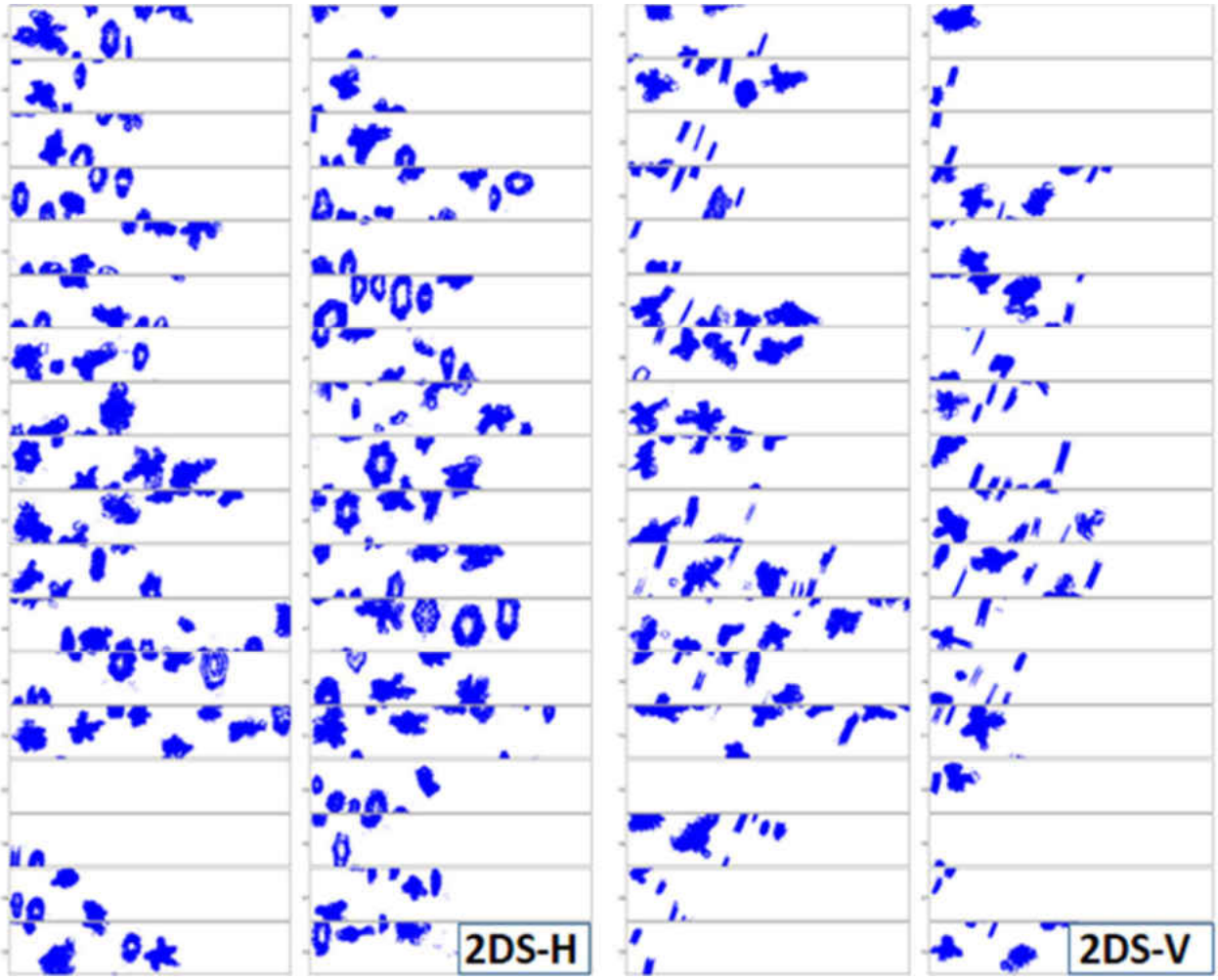

Figure 9: This figure shows 2DS particle images from 25 May 2014, 19:55:28-19:56:00 UTC. The 2DS-H (2DS-V) image corresponds to the particle images obtained with the horizontally (vertically) aligned probe arm of the instrument. There are 4 columns (two for each 2DS orientation) of particle image buffers. Each row within these columns represent the first buffer for second of data.

Table 4: Plate Cases

Project	Flight Date	Start Time	End Time
IPHEx	18 May 2014, 10:55:51 UTC	13:08:00 UTC	13:10:00 UTC
		13:16:00 UTC	13:18:00 UTC
		13:24:00 UTC	13:25:00 UTC
	25 May 2014, 18:59:17 UTC	19:49:00 UTC	19:56:00 UTC
		20:05:00 UTC	20:11:00 UTC
	11 June 2014, 16:42:00 UTC	17:59:00 UTC	18:01:00 UTC
OLYMPEx	12 Nov. 2015, 18:49:13 UTC	20:31:00 UTC	20:41:00 UTC
	05 Dec. 2015, 14:17:47 UTC	17:05:00 UTC	17:08:00 UTC
	12 Dec. 2015, 16:39:54 UTC	18:39:00 UTC	18:42:00 UTC
Total:		8 Cases	39 Minutes

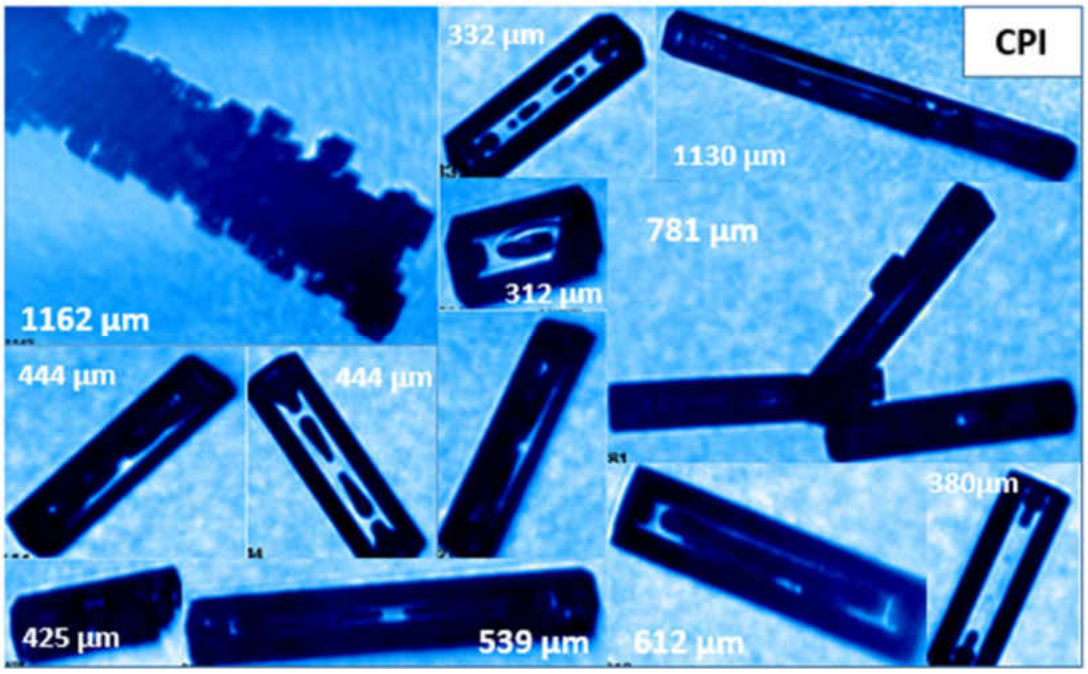

Figure 10: This figure shows CPI images from 28 May 2014, 15:35:00-15:40:00 UTC. The diameter given in the white text is the largest particle image dimension.

Columns

The May 28th, 2014 flight is typical of all observed column cases (Figure 10). As the vertical 2DS images show in Figure , there appears to be a constant canting angle of these column images, closely resembling the column images within Figure 3. However, the 2DS horizontal particle images have no preferred canting angle, indicating a possible random orientation. All of the column cases within Table 5 appear to contain a preferred orientation within the 2DS vertical array but no discernable preferred orientation within the 2DS horizontal array.

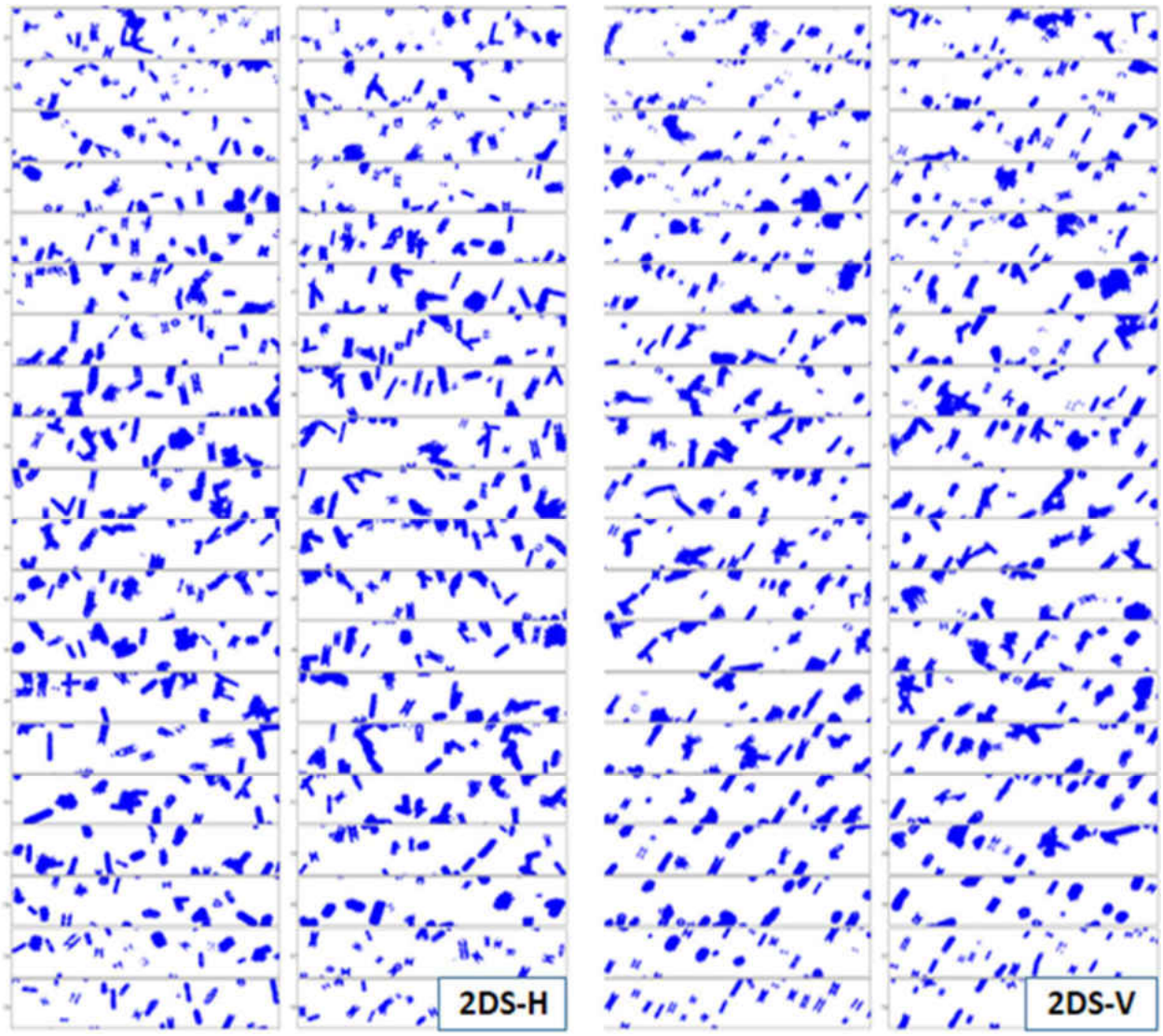

Figure 11: This image shows 2DS particle images from 28 May 2014, 19:48:20-19:49:00 UTC. The 2DS-H (2DS-V) image corresponds to the particle images obtained with the horizontally (vertically) aligned probe arm of the instrument. There are 4 columns (two for each 2DS orientation) of particle image buffers. Each row within these columns represent the first buffer for second of data.

Needles

The observed orientation feature for needles (Figure 12) is best represented by the December 4th, 2015 flight. Similar to the column cases, there appears to be a constant canting angle for particle images within the vertical array of the 2DS (Figure 13). There is no discernable constant canting angle for particle images within the horizontal array. Table 5 contains the list of needle cases within the IPHEx and OLYMPEx datasets. It should be noted that two of the needle cases listed in Table 5 are dominated by needle aggregates. These two needle aggregate cases were included in this study because atmospheric environments where needle aggregates are under represent are rare and under-sampled.

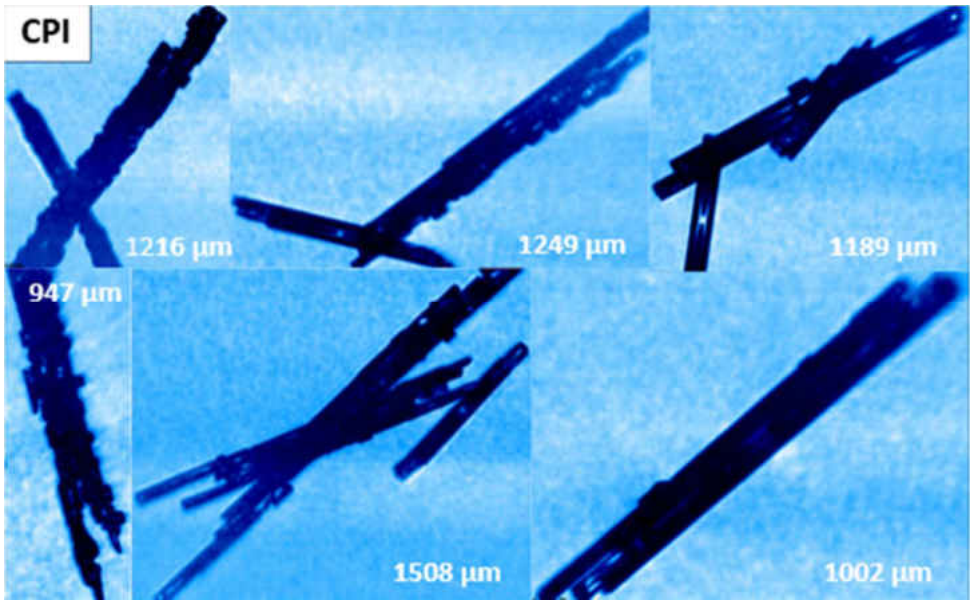

Figure 12: This image shows CPI images from 4 Dec. 2015, 18:10:00-18:20:00 UTC. The diameter given in the white text is the largest particle image dimension.

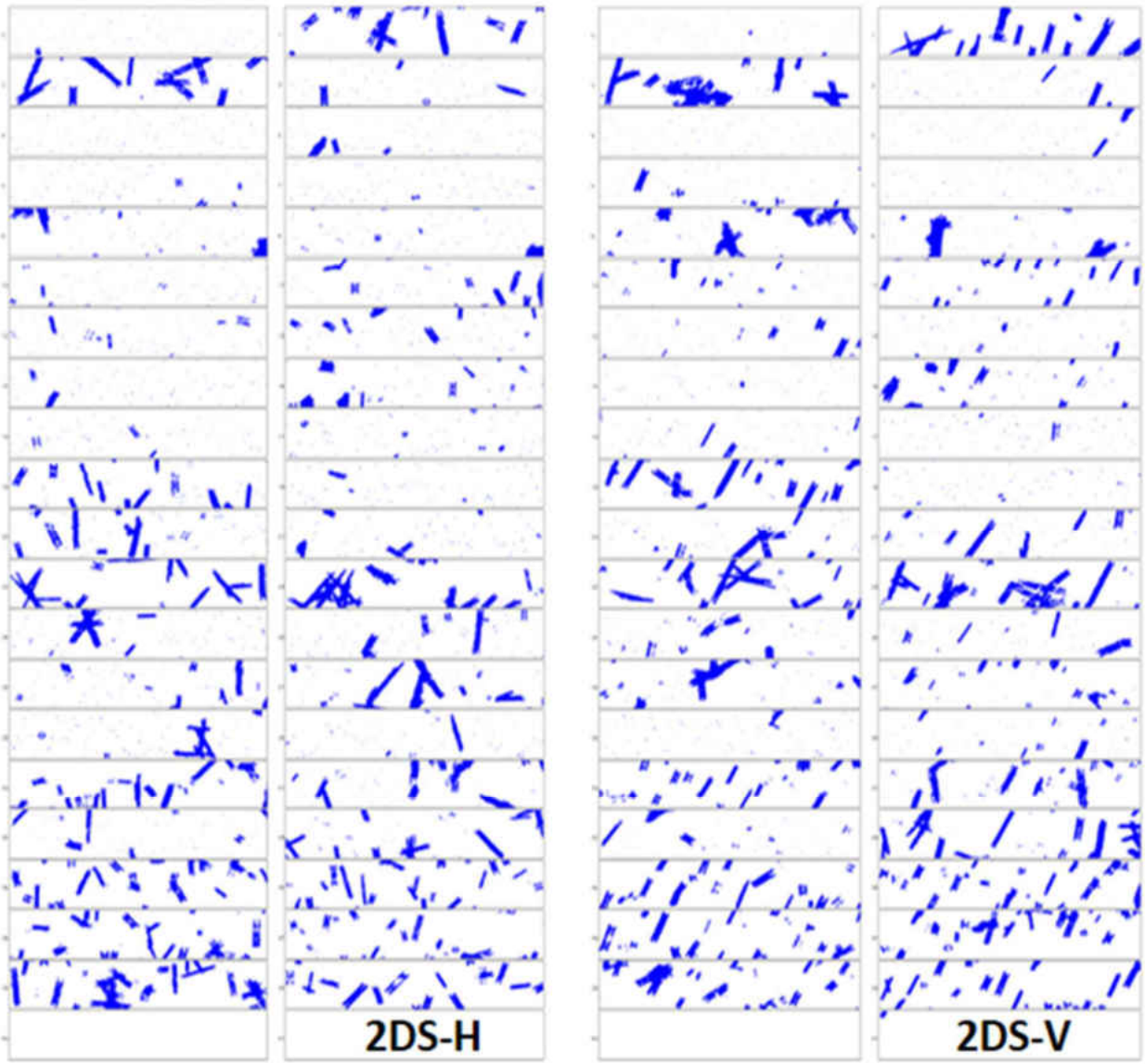

Figure 13: This image shows 2DS particle images from 4 Dec. 2015, 18:17:00-18:17:39 UTC. The 2DS-H (2DS-V) image corresponds to the particle images obtained with the horizontally (vertically) aligned probe arm of the instrument. There are 4 columns (two for each 2DS orientation) of particle image buffers. Each row within these columns represent the first buffer for second of data.

Table 5: Column and Needle Cases

Crystal Habit	Project	Flight Date	Start Time	End Time
Column	IPHEx	10 May 2014, 15:38:13 UTC	17:17:00 UTC 17:25:00 UTC	17:21:30 UTC 17:27:00 UTC
		28 May 2014, 13:10:57 UTC	15:37:00 UTC	15:40:00 UTC
	OLYMPEx	3 Dec. 2015, 13:35:43 UTC	15:25:00 UTC	15:28:00 UTC
Needle	OLYMPEx	13 Nov. 2015, 14:40:36 UTC	15:21:00 UTC 15:27:00 UTC	15:24:00 UTC 15:31:00 UTC
		14 Nov. 2015, 19:24:36 UTC	19:48:00 UTC 20:25:00 UTC	19:51:00 UTC 20:36:00 UTC
		4 Dec. 2015, 16:50:19 UTC	18:17:00 UTC	18:22:00 UTC
Total:		6 Cases (3 Column, 3 Needle)	38.5 min (12.5 min Column, 26 min Needle)	

CHAPTER IV

RESULTS

Overview

The cases presented within the previous chapter represent instances where naturally horizontally oriented ice particles were observed with the UND-Citation II during the IPHEx and OLYMPEx campaigns. Of these cases, a select few were chosen from each particle habit to represent the predominant particle orientation of these particles found within the 2DS sample volume. For each of these select cases, particle images are shown from the CPI and 2DS. While these images indicate the presence of horizontally oriented ice particles within the environment and their orientation within the sample volume of the 2DS, a quantitative means of describing the particle orientation and the effect of this orientation on derived parameters is necessary. Derived measurements of particle characteristics, outlined in Chapter II, offer the opportunity to express the observed orientation and the effects this orientation has on derived parameters.

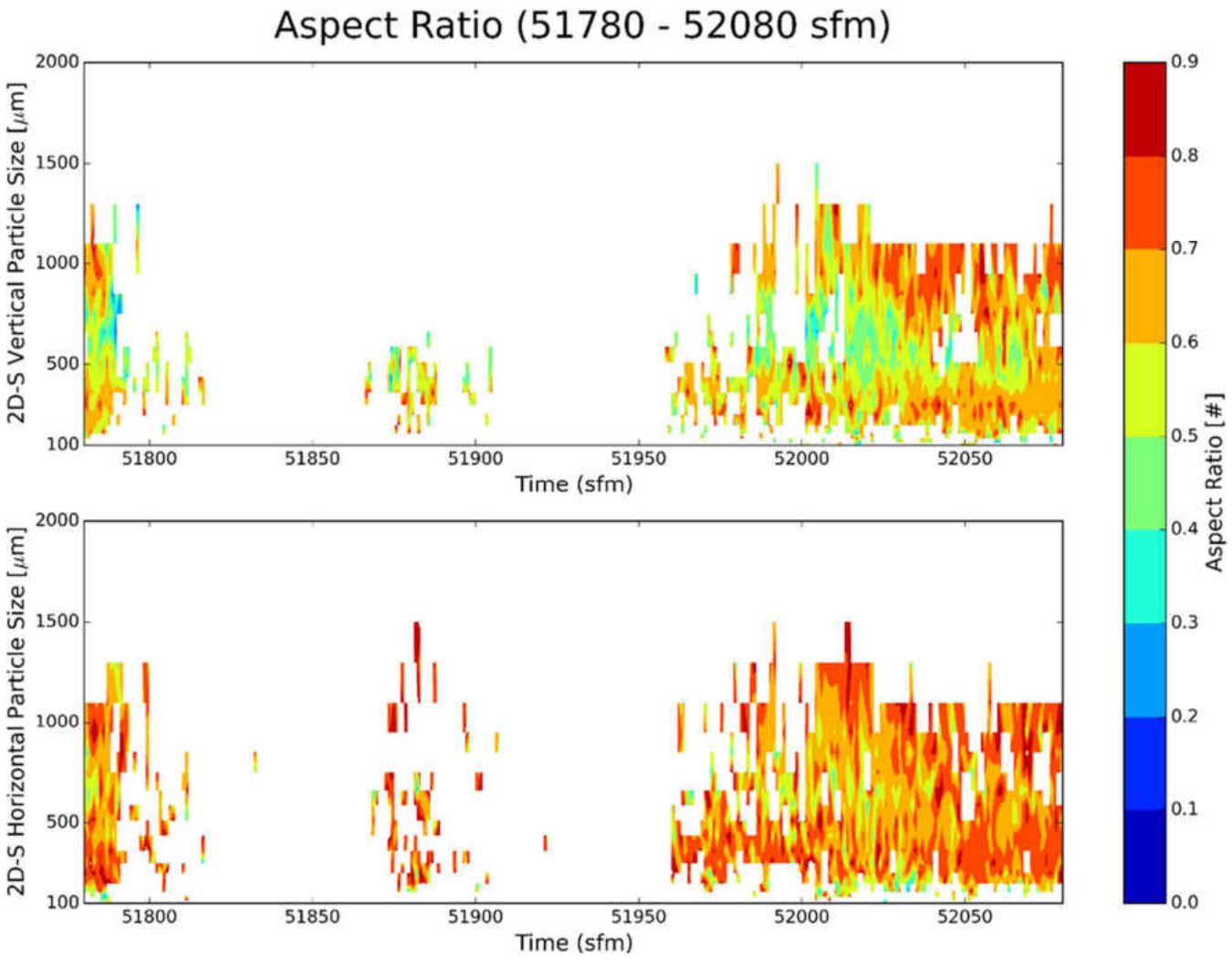

Figure 14: This figure shows 2DS aspect ratios calculations for dendritic particles observed on the 23 May 2014 flight from 51780 to 52080 sfm.

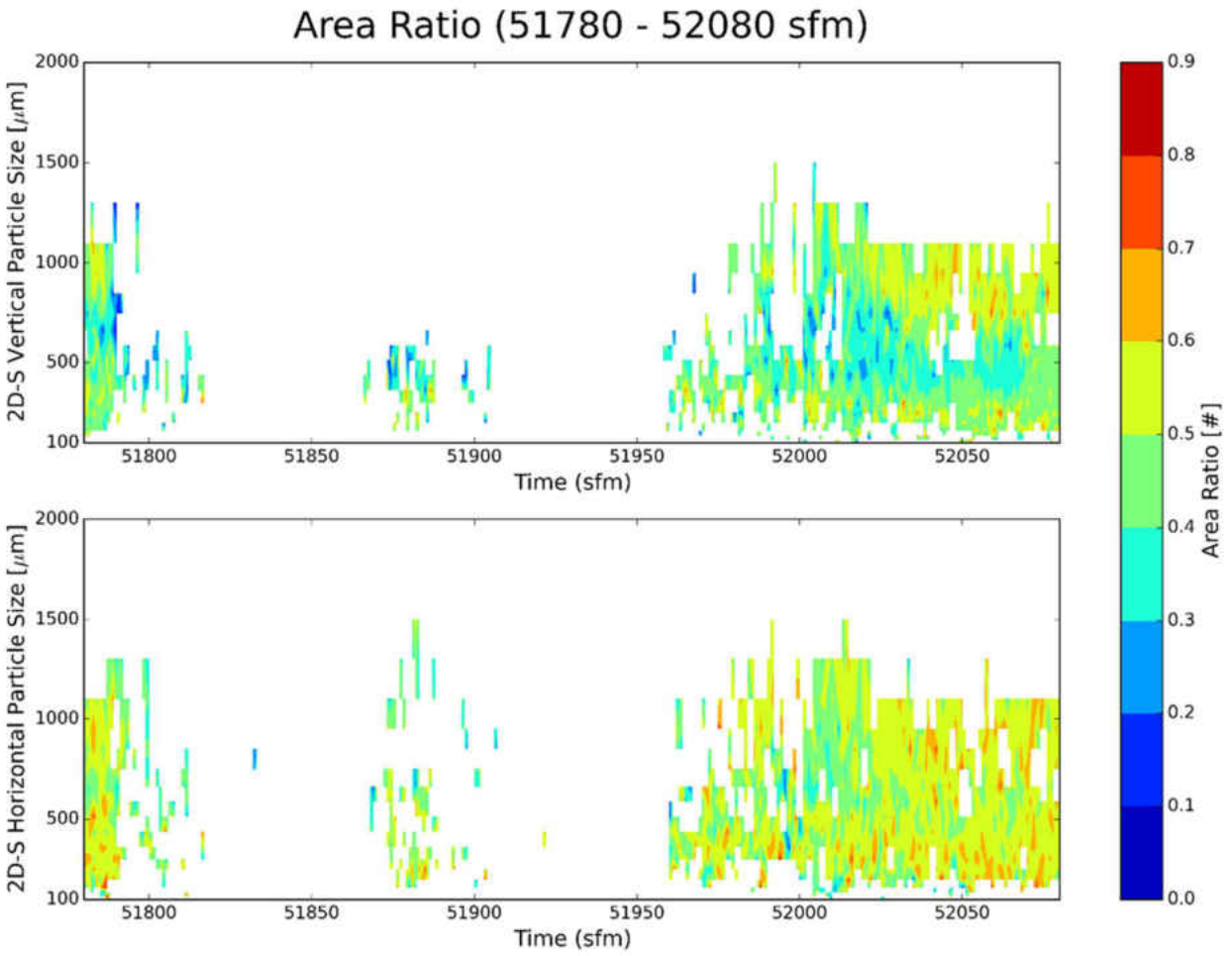

Figure 15: This figure shows 2DS area ratio calculations for dendritic particles obtained on the 23 May 2014 flight from 51780 to 52080 sfm.

Dendrite Cases

The May 23rd, 2014 dendrite case contains remarkable 2DS and CPI images of dendrites, as shown in Chapter III. These dendrites are curiously more discernable within the horizontal array of the 2DS than the vertical array. Figure 14 contains the aspect ratio measurements from both orientations of the 2DS during this period, while Figure 15 contains the area ratio

measurements. The aspect ratio measurements clearly indicate a stark contrast between the orientations of the 2DS. Aspect ratio measurements that correspond to the dendrite images within Figure 4 (i.e. 51,868 – 51,900 sfm) contain values close to one for particle sizes greater than 800 microns for the horizontal array. The 2DS vertical array has lower aspect ratio values during this time period, and also lower values throughout this entire case. The area ratio measurements within Figure 15 follow the same trend for this time period. Area ratio measurements are greater than 0.5 for large segments of the 2DS horizontal array, while measurements are lower for the vertical array.

Comparison of the particle size parameters is found within Figure 16, while derived size distributions from each orientation of the 2DS are found within Figure 17. Within Figure 16, the majority of particle diameters for each parameter are found above the one to one lines. This indicates particle images observed with the 2DS-H are larger than the same particles within the 2DS-V. Slope and intercept of the best fit line for each of these size parameters are found, and best fit lines are also shown within Figure . The best fit lines are above the one to one lines, indicting larger particle images within the horizontal array. While the slopes of the best fit lines are less than one, their position above the one to one line indicate that

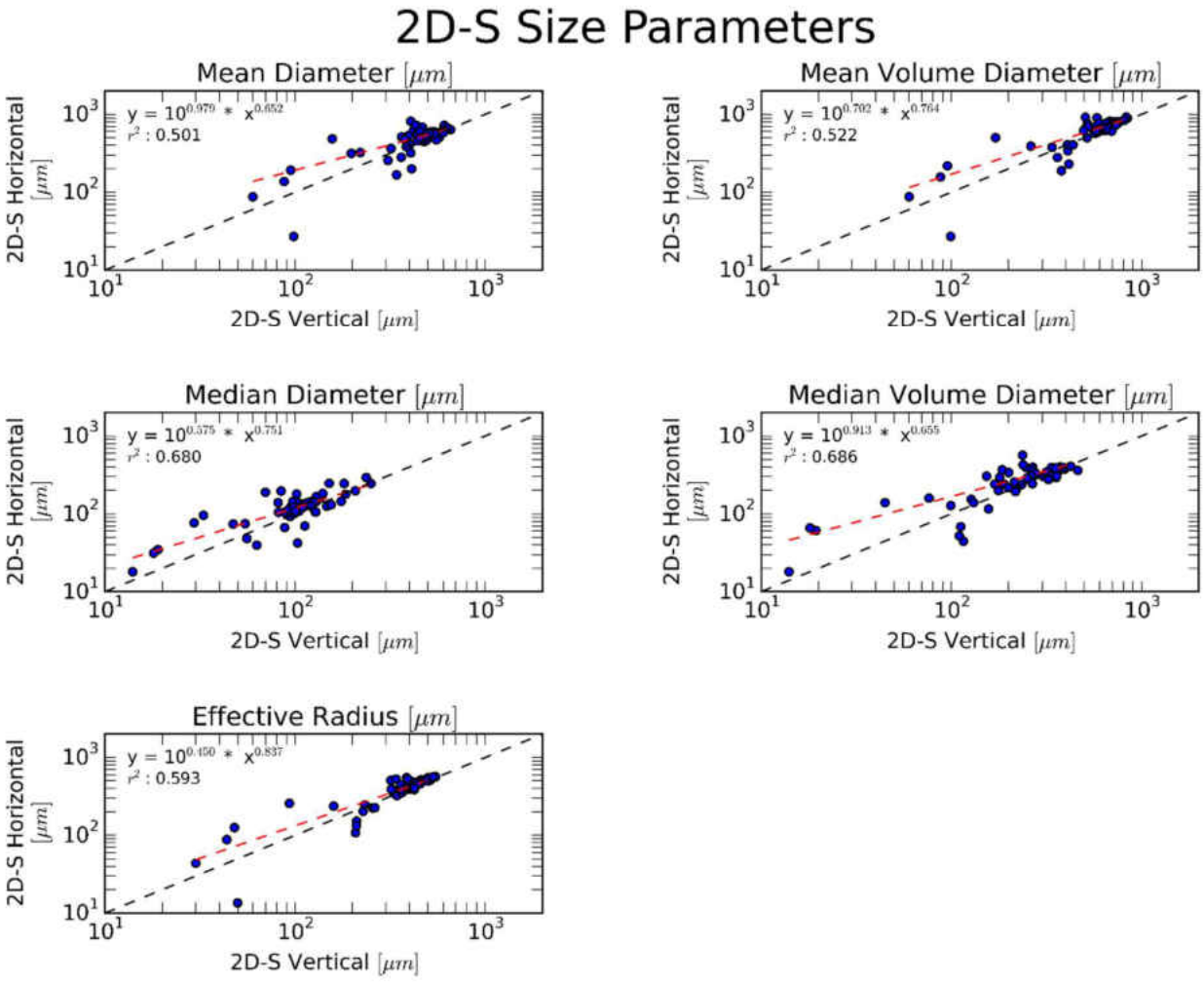

Figure 16: This figure shows 2DS derived size parameters obtained on 23 May 2014 flight from 51780 to 52080 sfm. Data represents five second averages of the original 1 Hz data for each parameter.

the largest discrepancy between 2DS orientations are at the smaller particle sizes. Within Table 6 are five second averages for the 2DS derived parameters for the dendrite cases. Averages for each of the size parameters within Table 6 are larger for the 2DS-H. The average differences

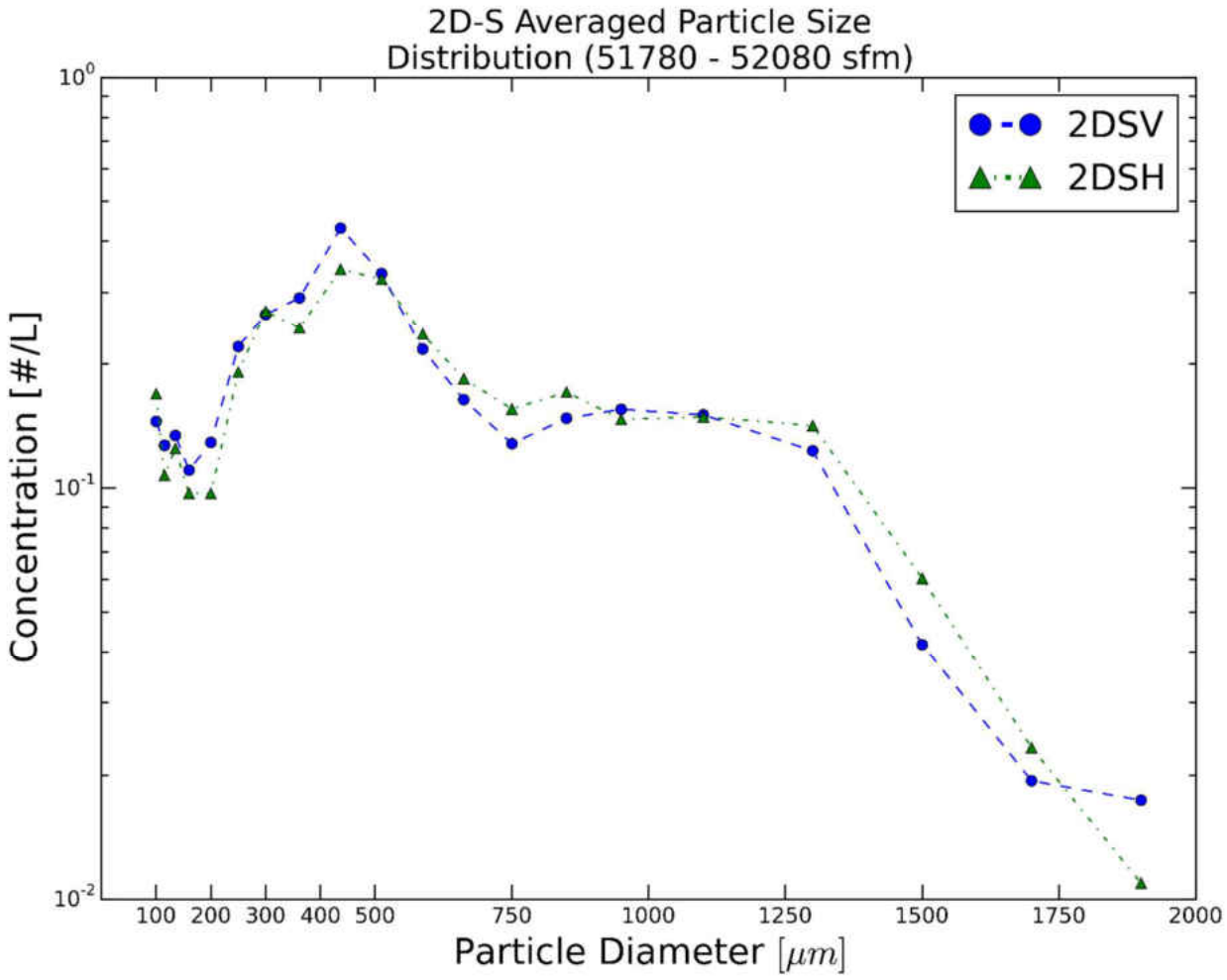

Figure 17: This figure shows 2DS averaged particle size distributions observed on the 23 May 2014 IPHEx flight from 51780 to 52080 sfm.

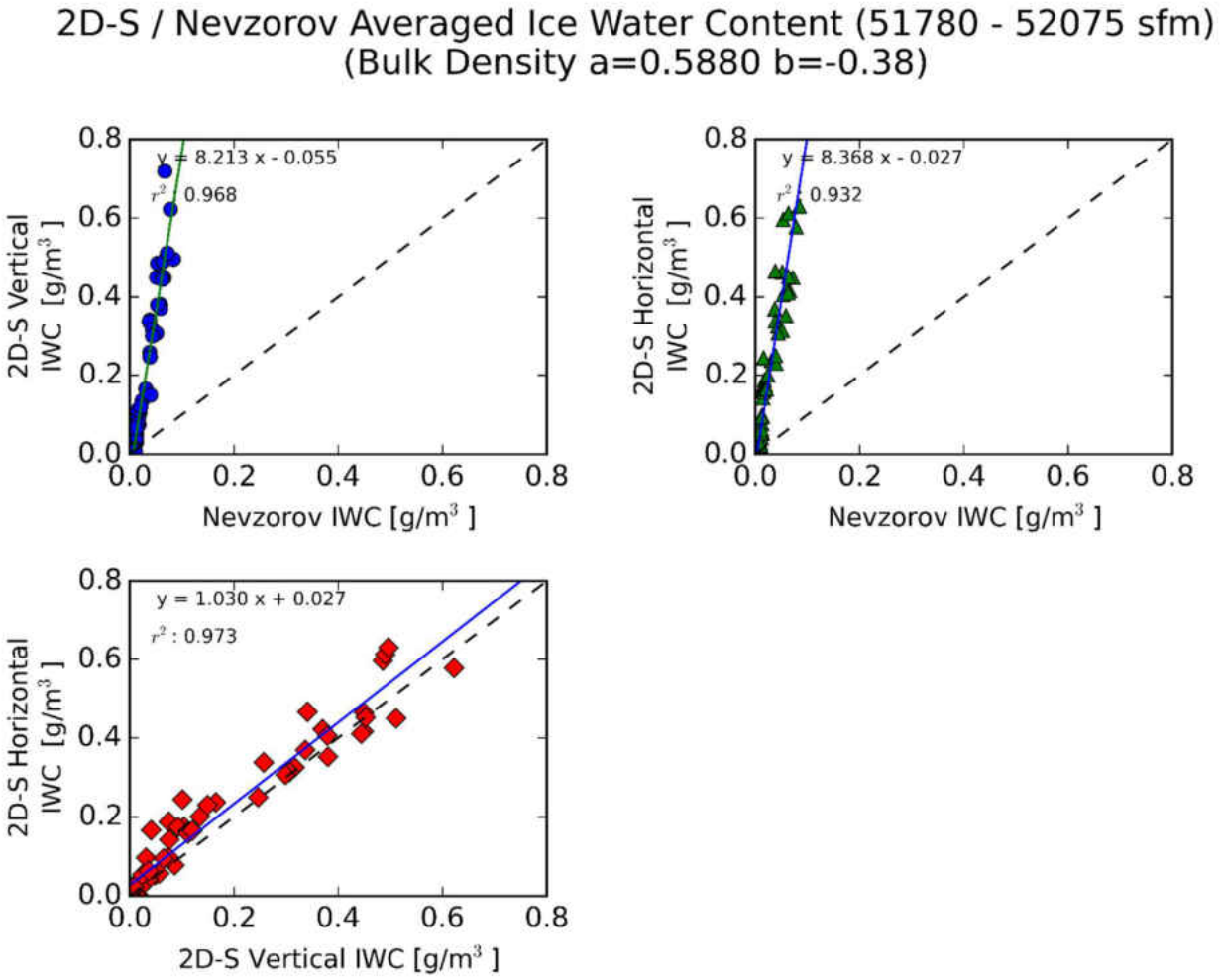

Figure 18: This figure shows Nevzorov and derived 2DS IWC from the 23 May 2014 IPHEx flight from 51780 to 52080 sfm. 2DS IWC was derived using the bulk density method for dendrites. The average IWC for the 2DS-H (2DS-V) during this period was 0.20 g/m^3 (0.17 g/m^3).

(vertical measurements minus horizontal measurements) between size parameter calculations are also included within Table 6, and clearly indicate larger values for each of these size parameters for the 2DS-H. The spread of the difference is also shown for each parameter, with the minimum and maximum difference for each parameter shown. For the majority of the size parameters, the 2DS-H contains larger particle images compared to particle images from the 2DS-V.

Additionally, the average size distribution for each orientation of the 2DS is found within Figure 17. The size distribution was calculated by taking the average of particle concentrations for each particle size bin every five seconds. Figure 17 shows that the observed difference in particle sizes found within Figure 16 is represented within the particle size distribution. For particle sizes greater than 600 microns, the 2DS-H contains greater values per bin size. It is interesting to note that the 2DS-V size distribution has higher values for particle sizes less than 500 microns, with the inflection point between the two distributions occurring around 550 microns. The differences in the particle size distributions suggest that additional moments of these distributions, such as ice water content and radar reflectivity factor, would inherit these differences. Figure 18 contains the derived ice water content for both orientations of the 2DS. Ice water content was calculated using the bulk density method for dendrites, where the particles are assumed to be equivalent volume spheres with a density defined by the relationship in (Heymsfield 1972). The time series of IWC shows greater values for the 2DS-H array compared to the 2DS-V array. The comparison of IWC measurements from both orientations shows a 3% difference in IWC, with larger values calculated by the 2DS-H. This is indicated by the majority of measurements above the one to one ratio line for measurements less than 4 grams per cubic meter. The best fit line for the comparison of IWC measurements is also above the one to one ratio line, with a positive slope and offset. This shows that the 2DS-H derived IWC measurements are larger compared to the IWC measurements derived from the 2DS-V. Additionally, Figure 18 contains a comparison between each orientation of the 2DS and the Nevzorov hotwire probe. As seen in the time series and comparison plots, there is a stark

difference in IWC measurements between the probes. This could potentially be due to low crystal concentration and airflow around the Nevzorov. However,

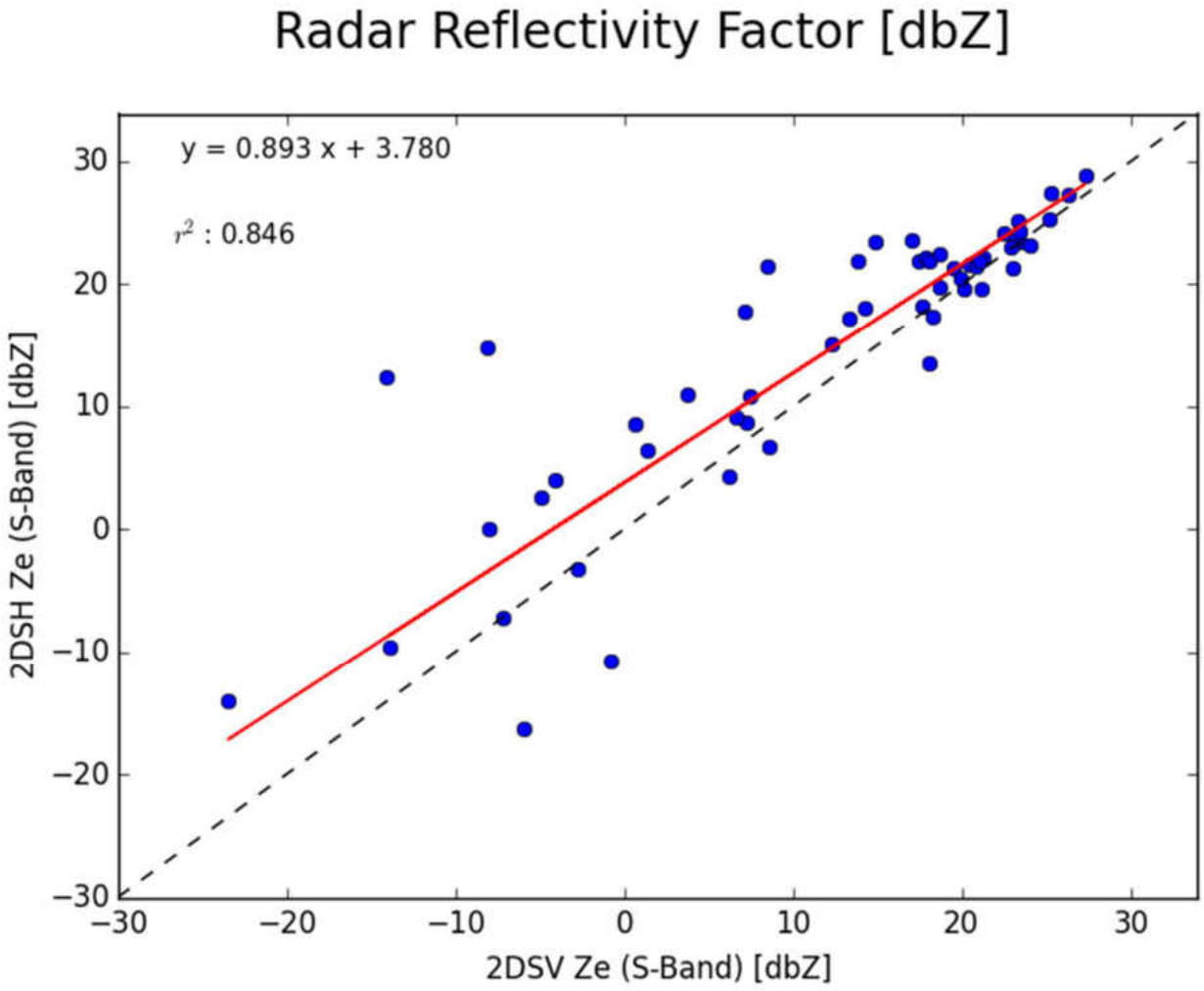

Figure 19: This figure shows 2DS radar reflectivity factor from the 23 May 2014 flight from 51780 to 52080 sfm. 2DS radar reflectivity factor was calculated using a constant dielectric constant (|K2| = 0.197) for S-band radar. The average radar reflectivity factor for the 2DS-H (2DS-V) during this period is 10.1 dbZ (7.9 dbZ).

even with the high offset between the 2DS and Nevzorov IWC, the best fit lines of the comparison indicate that the 2DS-H is in better agreement with the Nevzorov. Table 6 also contains the average derived IWC for the dendrite cases. The 2DS-H IWC has 0.08 grams per cubic meter greater average than the 2DS-V IWC. Figure 19 contains the radar reflectivity factor for both orientations of the 2DS. Radar reflectivity factor was calculated using the national weather service constant value of 0.197 for dielectric constant. As Figure 19 shows, the majority of values above 0 dbZ are found within the 2DS-H array. Table 6 contains the average radar reflectivity factor calculations for each of the dendrite cases. The 2DS-H has, on average, 3.4 dbZ greater values of radar reflectivity factor than the 2DS-V on the May 23rd, 2014 dendrite case, which is roughly a factor of 2 difference in equivalent returned power. Additionally, the time period corresponding to the dendrite images within Figure 5, contains a broad disparity between the 2DS orientations, with the 2DS-H containing an average radar reflectivity factor that is 4.6 dbZ greater than measurements derived from the vertical array. The maximum disparity between orientations during this period is 11.6 dbZ, roughly a factor of 12 difference in equivalent returned power.

All of these figures reinforce the observation of vertically oriented 2DS particle images during this period. Aspect ratio measurements are greater for the horizontal array since the particle images contain the basal plane of the dendrites. Area ratio measurements are also greater for the horizontal array, since the basal plane of the dendrite has more surface area than the side plane. The stark difference in these measurements between the orientations of the 2DS also

indicate that the orientation is not random. One would expect values to be roughly the same between the arrays for this period if there was random orientation. As discussed in previous chapters, any orientation of a particle around the image viewing plane is expected to produce a bias in particle size compared to a particle that exhibits no orientation. The preferred orientation of dendrites has been shown above to size particles differently between 2DS orientations, with the horizontal array containing larger particle sizes. This disparity in particle sizes leads to differences between derived parameters, such as ice water content and radar reflectivity factor, for the probe orientations.

Table 6 : This table contains averages for each 2DS parameter for all dendrite cases. Difference represents the average difference between orientations of the 2DS. Minimum (maximum) represents the minimum (maximum) value of the average difference between orientations of the 2DS.

Parameter	**Units**	**2DS-V**	**2DS-H**	**Difference**	**Min**	**Max**
Mean Diam.	µm	640.76	678.5	-37.74	-66.6	-14.17
Median Diam.	µm	224.64	257.26	-32.62	-78.4	-7.04
Mean Vol. Diam.	µm	834.61	870.86	-36.25	-75.47	-19.15
Median Vol. Diam.	µm	415.12	423.22	-7.3	-40.47	5.7
R_{eff}	µm	541.41	555.59	-14.19	-39.46	-4.3
IWC	g/m^3	0.94	1.02	-0.08	-0.3	0.03
Z_e	dbZ	23.31	24.02	-0.67	-3.36	0.49

Table 6 contains the averages of derived size parameters, ice water content, and radar reflectivity for the dendrite cases observed during IPHEx and OLYMPEx. The 2DS-H contains larger mean diameter, median diameter, mean volume diameter, and effective radius values. Overall, this difference in size parameters leads to the larger derived values of ice water content (0.08 grams per cubic meter on average) and radar reflectivity factor (average of 0.67 dbZ) for the 2DS-H. When compared with the average IWC for the 2DS-V (0.94 grams per cubic meter) and the 2DS-H (1.02 grams per cubic meter) over these cases, the average difference of 0.08 grams per cubic meter is roughly a 7.5% difference in IWC measurements between orientations of the 2DS.

Plate Cases

The May 25th, 2014 case is a flight segment that is dominated by large plate particles. This plate case is the best representation of the observed particle orientation found within the IPHEx and OLYMPEx campaigns. This observed particle orientation, as shown in Figure 8 in the previous chapter, is similar to the orientation of dendritic particles. Plate are clearly more distinguishable within the horizontal array of the 2DS, suggesting these particles are vertically oriented. Figure 20 and Figure 21 contain the aspect ratio and area ratio measurements for this flight segment. As with the dendrite case, aspect ratio measurements are greater for the 2DS-H array compared to the vertical array. Additionally, area ratio measurements are greater for the 2DS-H array compared to the vertical array. In contrast to the dendrite case, the May 25th, 2014 plate case has a lower concentration of particles, across all size bins, as shown in particle size

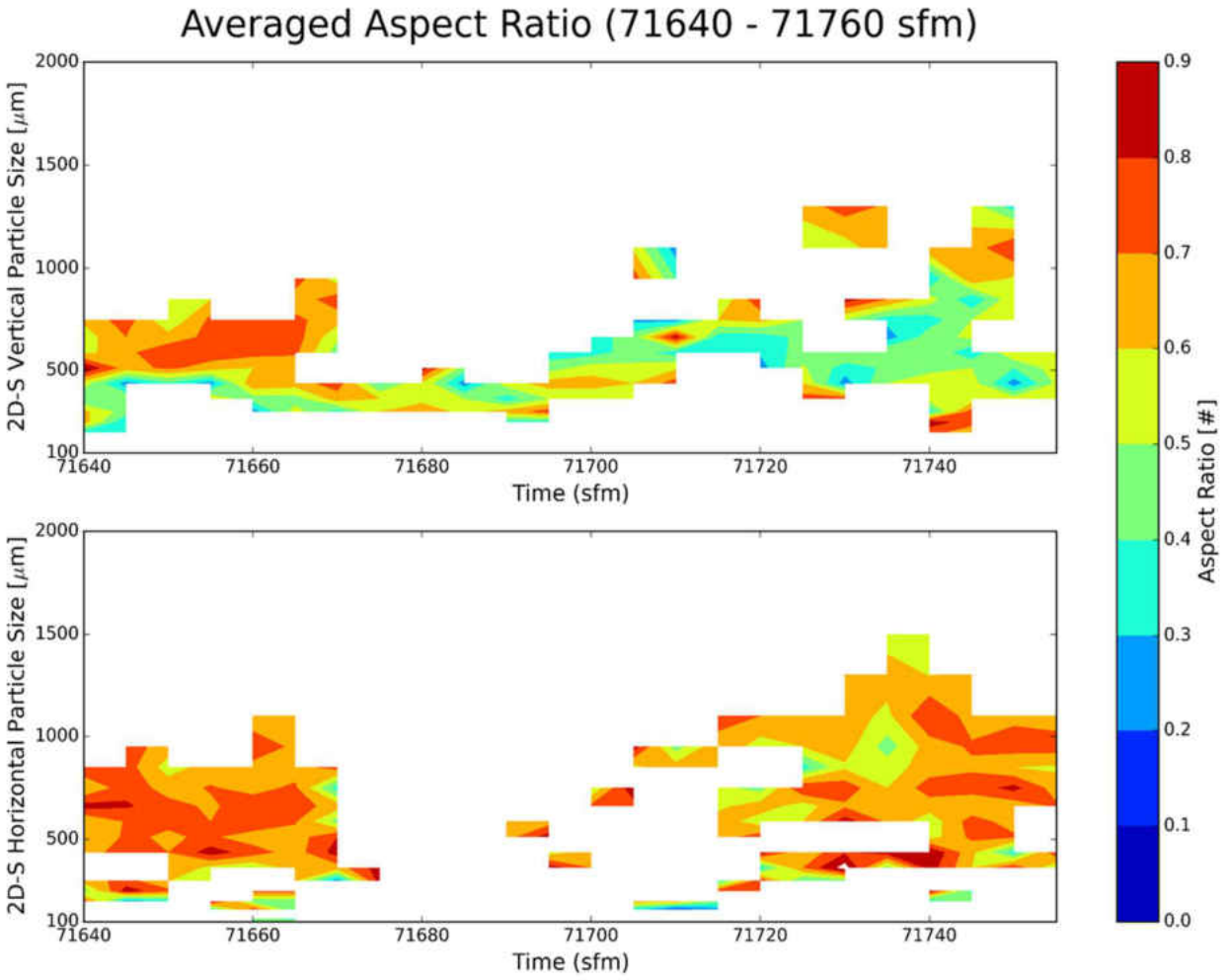

Figure 20: This figure shows 2DS measurements of aspect ratio for plates obtained on the 25 May 2014 flight from 71640 to 71760 sfm.

distribution within Figure 22. The effect of low concentrations can be seen in Figure 20 and Figure 21, where portions contain no measurements. While the concentration of particles is

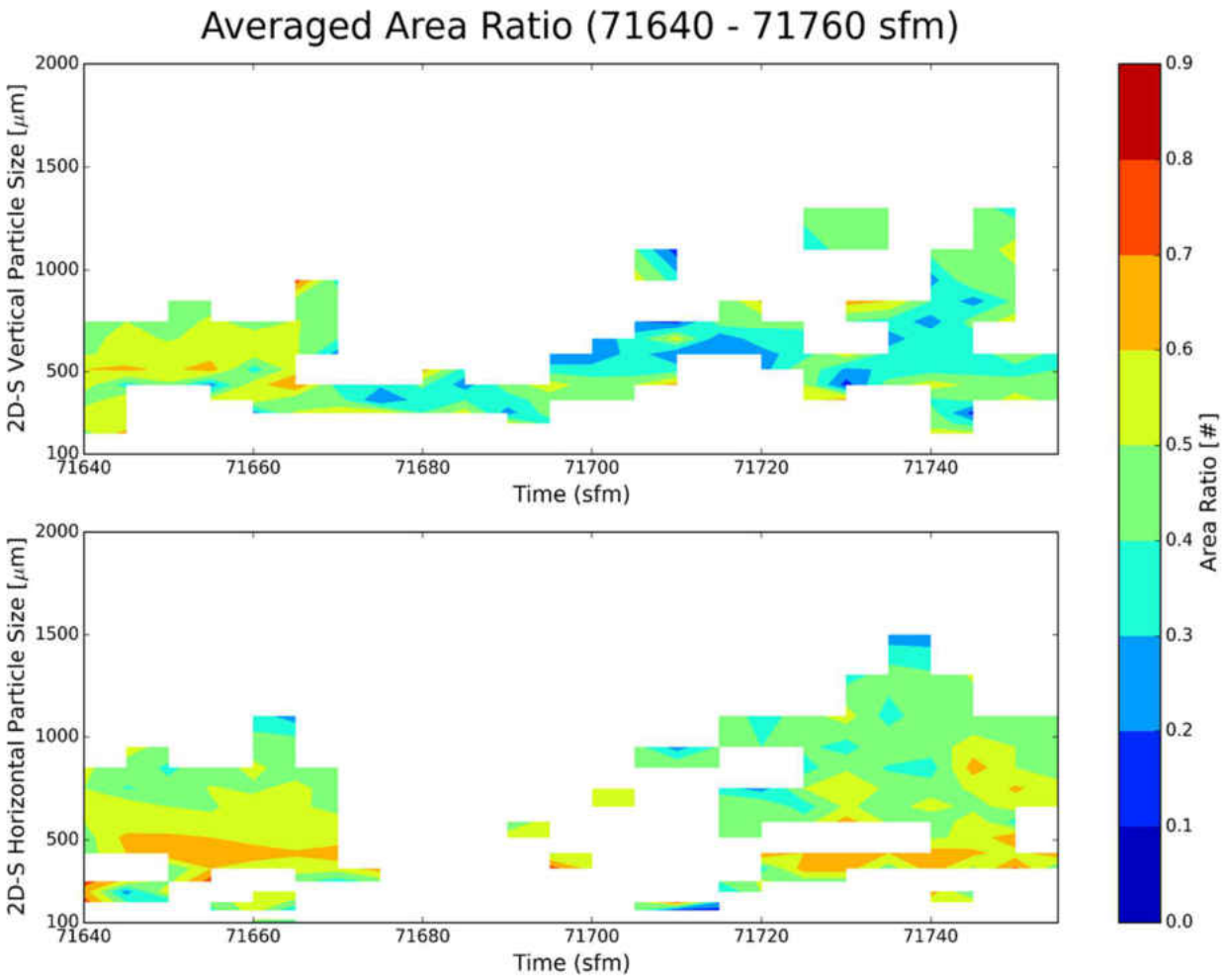

Figure 21: This figure shows 2DS measurements of area ratio for plates obtained on the 25 May 2014 flight from 71640 to 71760 sfm.

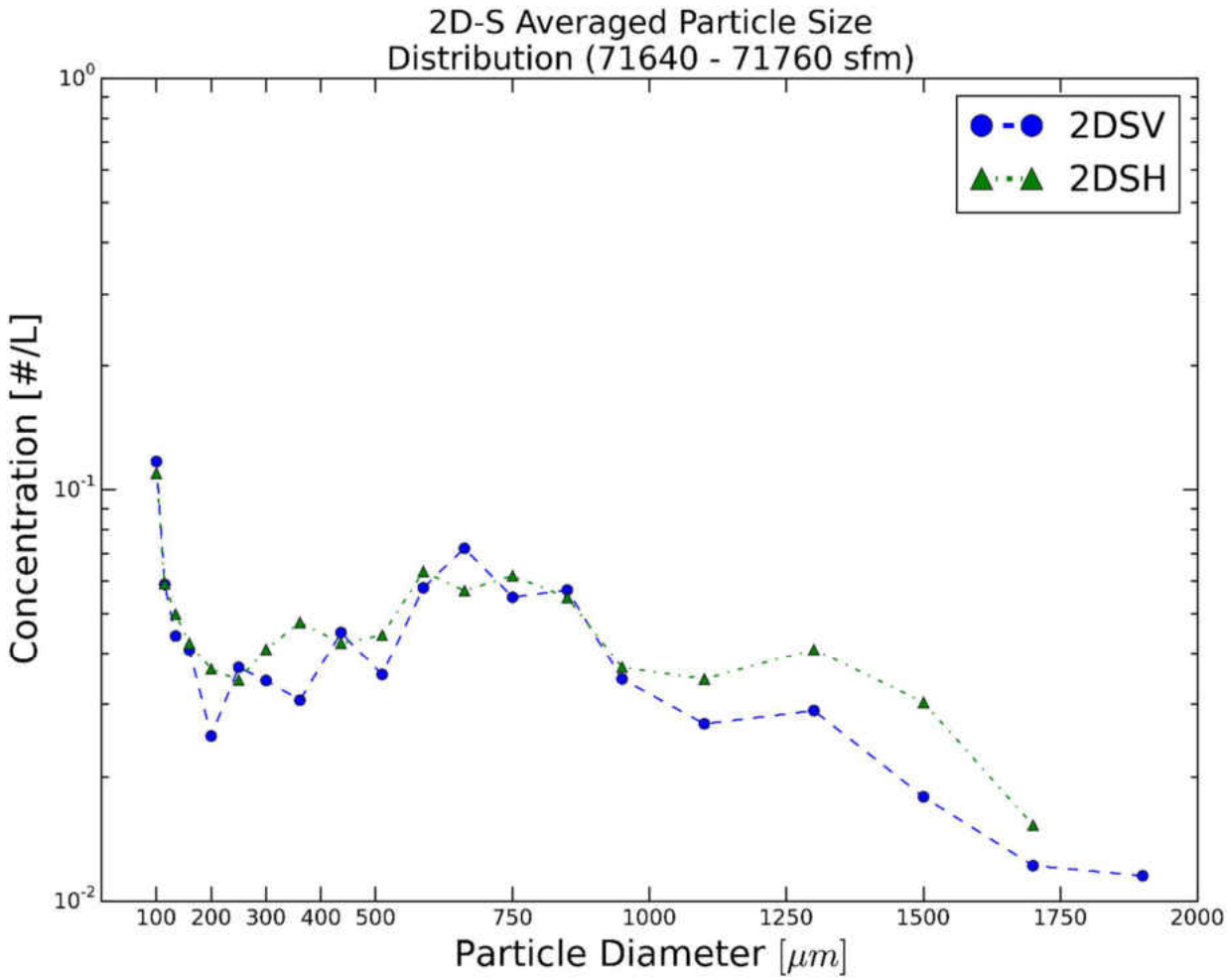

Figure 22: This figure shows the 2DS averaged particle size distributions of the 25 May 2014 flight from 71640 to 71760 sfm.

lower, the May 25th, 2014 case is still the best case to describe the plate orientation since it does not contain mixed particle habits. As shown in Figure 23, there is a clear difference in particle sizes for the orientations of the 2DS, with the horizontal array containing larger particle sizes for the mean diameter, mean volume diameter, median volume diameter, and effective radius.

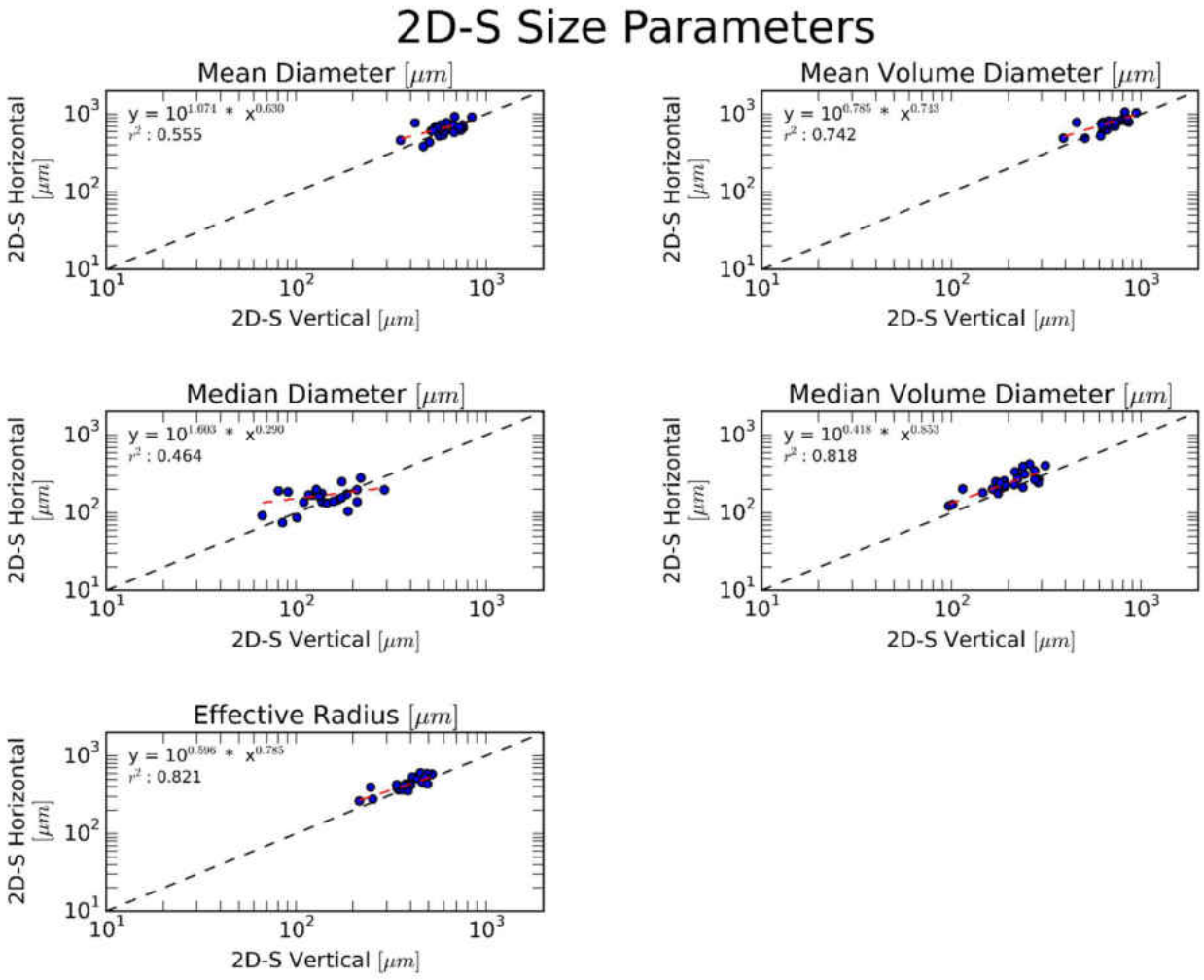

Figure 23: This figure shows 2DS derived size parameters from the 25 May 2014 flight from 71640 to 71760 sfm. Data represents five second averages of the original 1 Hz data for each parameter.

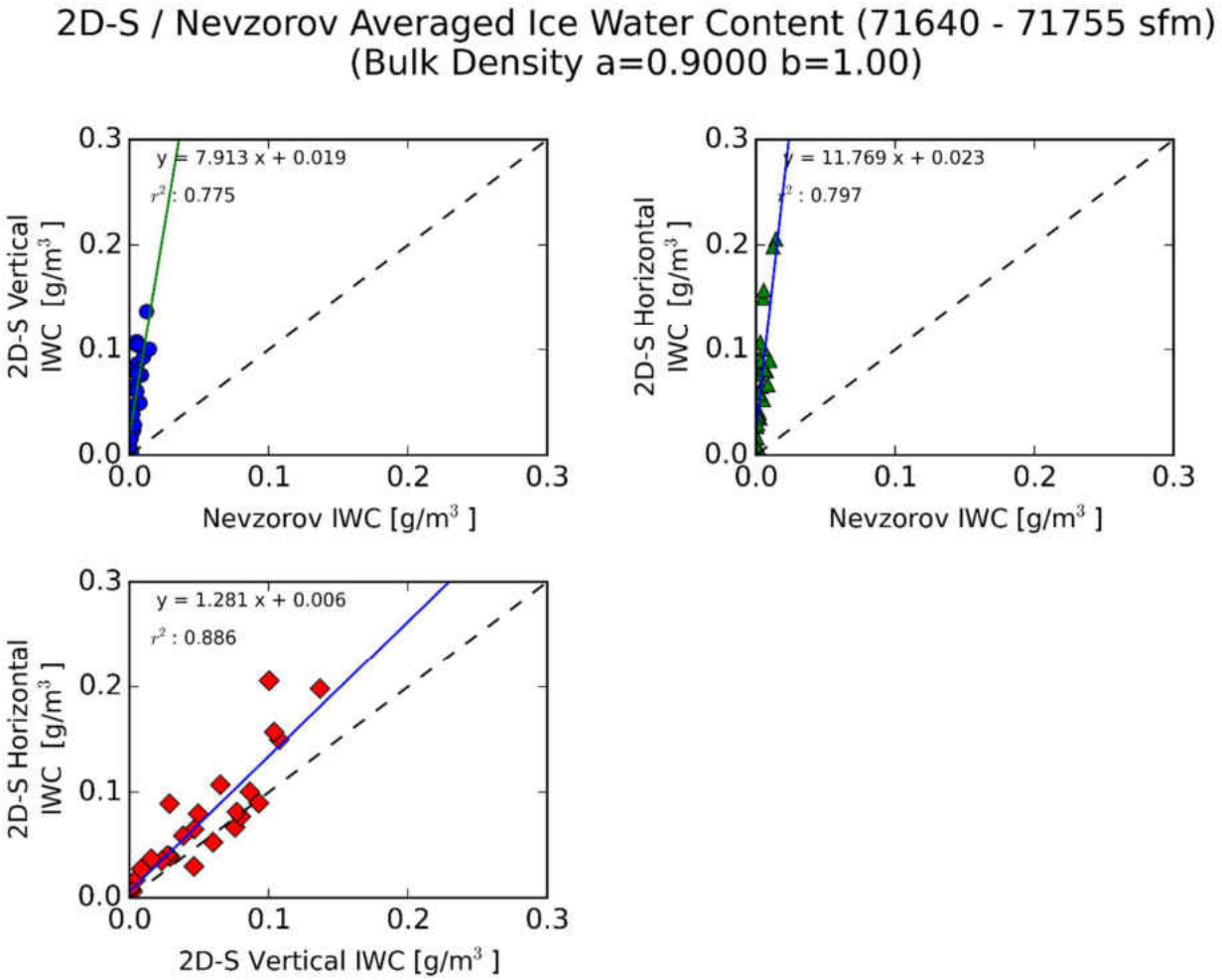

Figure 24: This figure shows Nevzorov and derived 2DS IWC from the 25 May 2014 flight from 71640 to 71755 sfm. 2DS IWC was derived using the bulk density method for dendrites. The average IWC for the 2DS-H (2DS-V) during this time period is 0.07 g/m^3 (0.05 g/m^3).

Also shown in Table 7, the averages of each of these size parameters are greater for the 2DS-H. The best fit lines of the majority of size parameters within Figure 23 show a distinct offset of the entire line above the one to one line, indicating that the 2DS-H contains larger values for those parameters. This offset is not found within the median diameter parameter, which contains a slope less than one. This slope indicates that while the 2DS-H contains larger values for smaller particle sizes, the 2DS-V contains larger values for larger particle sizes.

This difference between size parameters translates into larger ice water content measurements for the 2DS-H through most of this case (Figure 24). The 2DS-H derived IWC values are 28% greater and contain all measurements greater than 0.1 grams per cubic meter. The largest differences are seen in the time period from 71730 to 71760 sfm, which corresponds with the plate images shown in Figure . In Figure 25, the radar reflectivity factor follows the same pattern, with larger derived values for the 2DS-H array compared to the vertical array. The average values for radar reflectivity factor are located within Table 7, and indicate that 2DS-H measurements are an average of 0.49 dbZ greater than the 2DS-V measurements. In the period associated with images in Figure 9, the maximum difference between radar reflectivity measurements is 5.12 dbZ.

Table 7 shows that for most of the plate parameters, the 2DS-H has larger values, as similarly found in the dendrite tables. However, 2DS-V derived IWC has a higher average (0.06 grams per cubic meter) than the values derived from the 2DS-H. The spread of IWC values are shown within Table 7, with a maximum difference of 0.84 grams per cubic meter. This maximum is found on one flight, May 18th, 2014, which dominates the average IWC for the plate cases. When this flight is excluded, the 2DS-H contains 0.06 grams per cubic meter greater values of IWC than values derived from the 2DS-V. A possible explanation for the discrepancy of the May 18th case is that the flight segment is a mixed habit environment, containing large aggregates and plates, which mask the signal of preferably oriented plates. Additionally, portions of the May

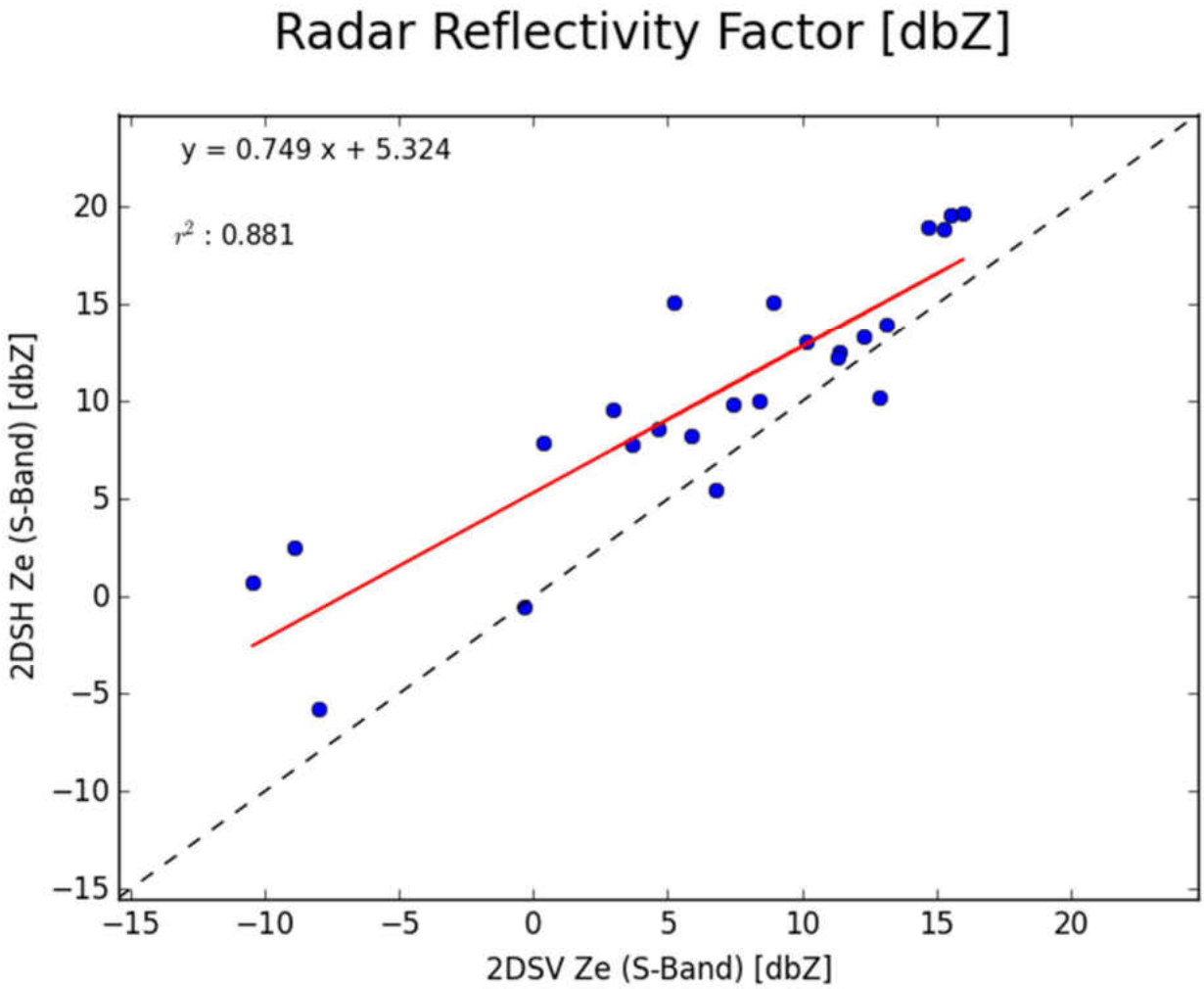

Figure 25: This figure shows 2DS radar reflectivity factor from the 25 May 2014 flight from 71640 to 71755 sfm. 2DS radar reflectivity factor was calculated using a constant dielectric constant (|K2| = 0.197) for S-band radar. The average radar reflectivity factor for the 2DS-H (2DS-V) during this time period is 7.4 dbZ (2.8 dbZ).

18th case contain smaller flight segments (roughly 1.5 minutes) than the rest of the plate cases,

which could affect particle statistics.

Table 7: This table contains averages of each 2DS parameter for all plate cases. Difference represents the average difference between orientations of the 2DS. Minimum (maximum) represents the minimum (maximum) value of the average difference between orientations.

Parameter	Units	2DS-V	2DS-H	Difference	Min	Max
Mean Diam.	µm	605.66	643.96	-38.26	-38.26	-54.85
Median Diam.	µm	201.24	221.47	-20.23	-54.28	-2.03
Mean Vol. Diam.	µm	777.18	812.1	-34.91	-65.53	-23.5
Median Vol. Diam.	µm	347.2	355.79	-8.59	-30.79	24.06
R_{eff}	µm	481.27	495.21	-13.94	-37.71	0.67
IWC	g/m^3	1.31	1.23	0.06	-0.31	0.84
Z_e	dbZ	19.41	20	-0.49	-3.59	2.11

Column Cases

The May 28th, 2014 flight segment contains solid and hollow column particles, as defined by CPI images Figure 10. As shown in Figure 11 of Chapter 3, there appears to be a preferred orientation of columns within the vertical array of the 2DS, such that there appears to be a constant canting angle. Figure 26 and Figure 27 contain the aspect- and area-ratio measurements for the column case.

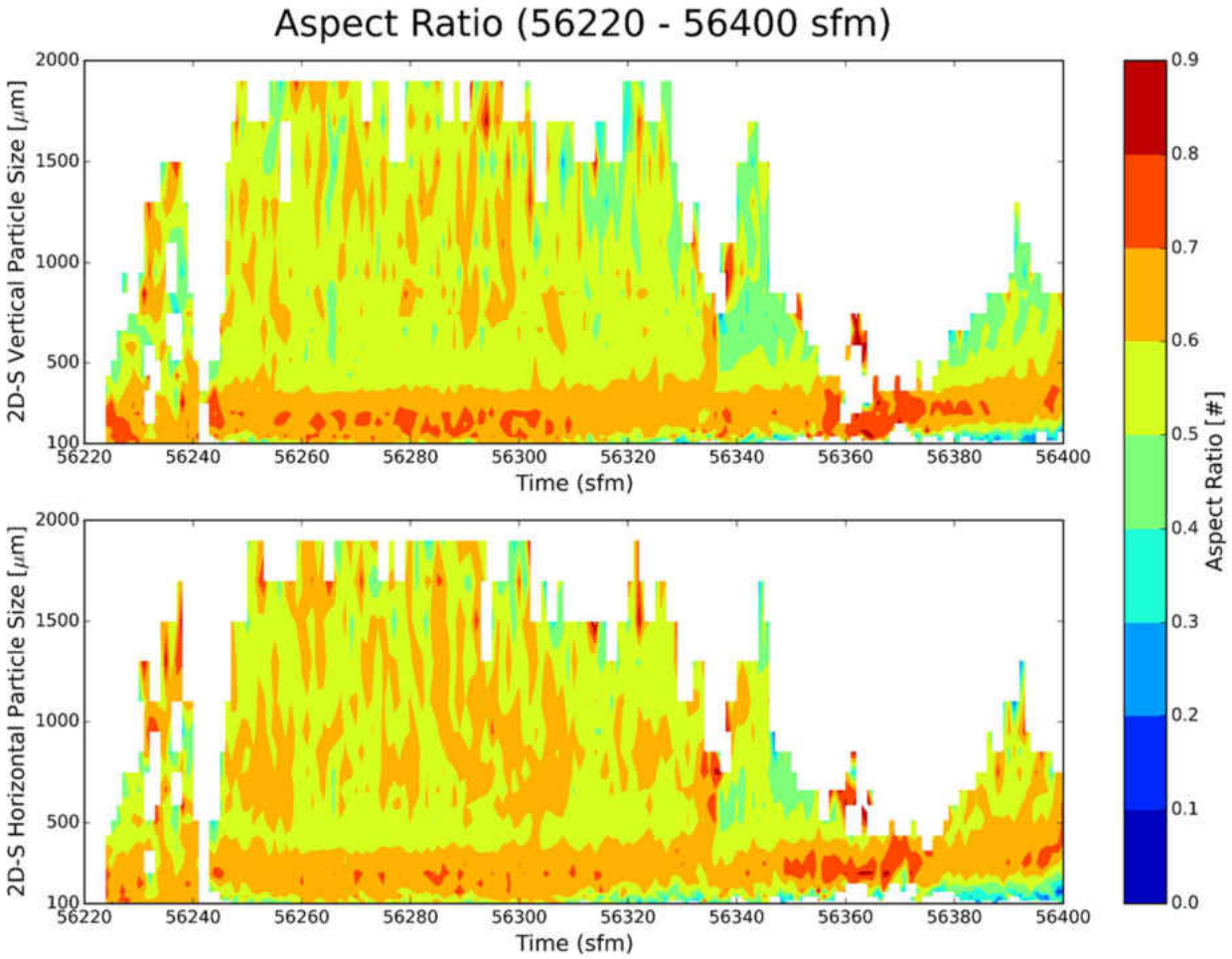

Figure 26: This figure shows 2DS measurements of aspect ratio for columns obtained on the 28 May 2014 flight from 56220 to 56400 sfm.

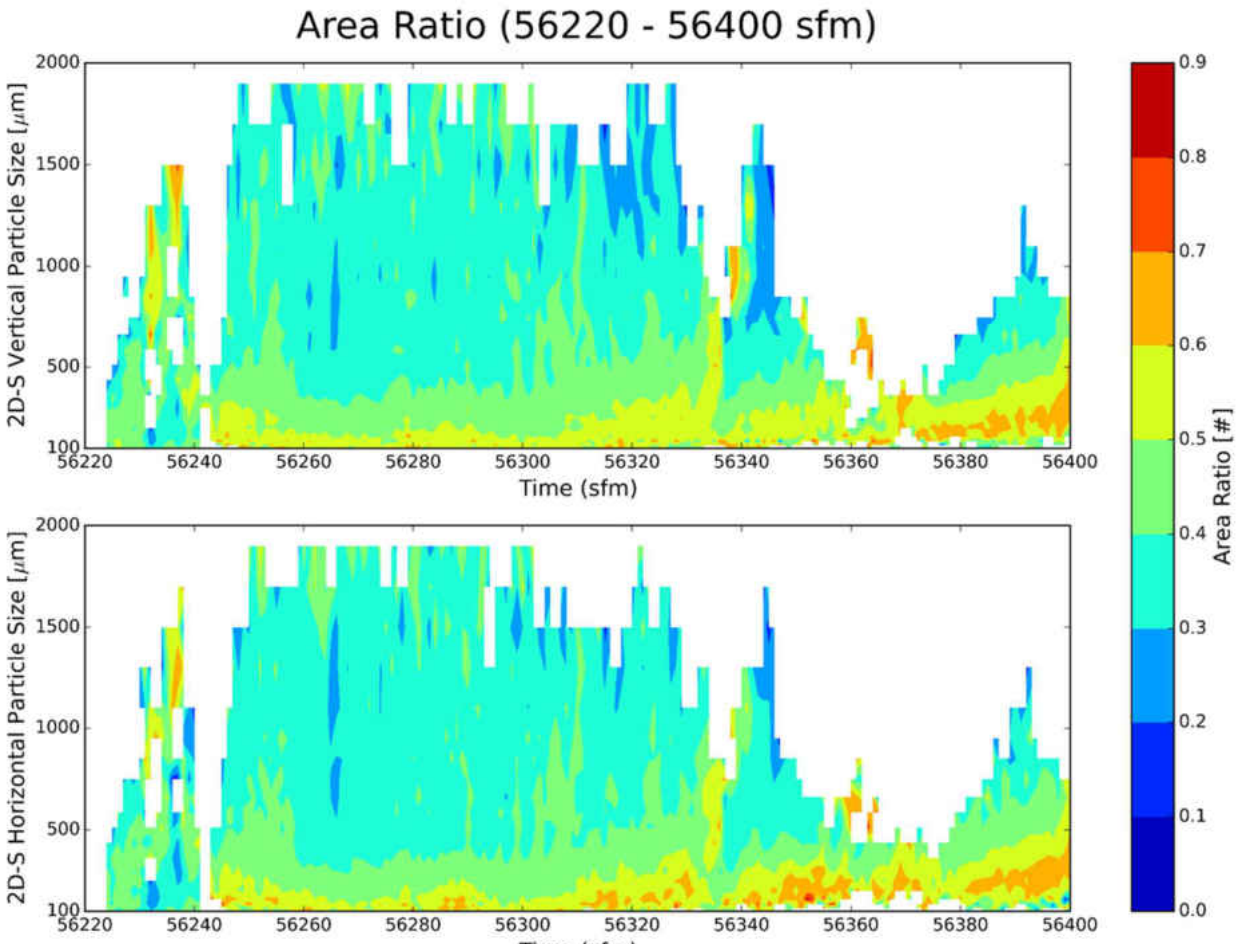

Figure 27: This figure shows 2DS measurements of area ratio for columns obtained on the 28 May 2014 flight from 56220 to 56400 sfm.

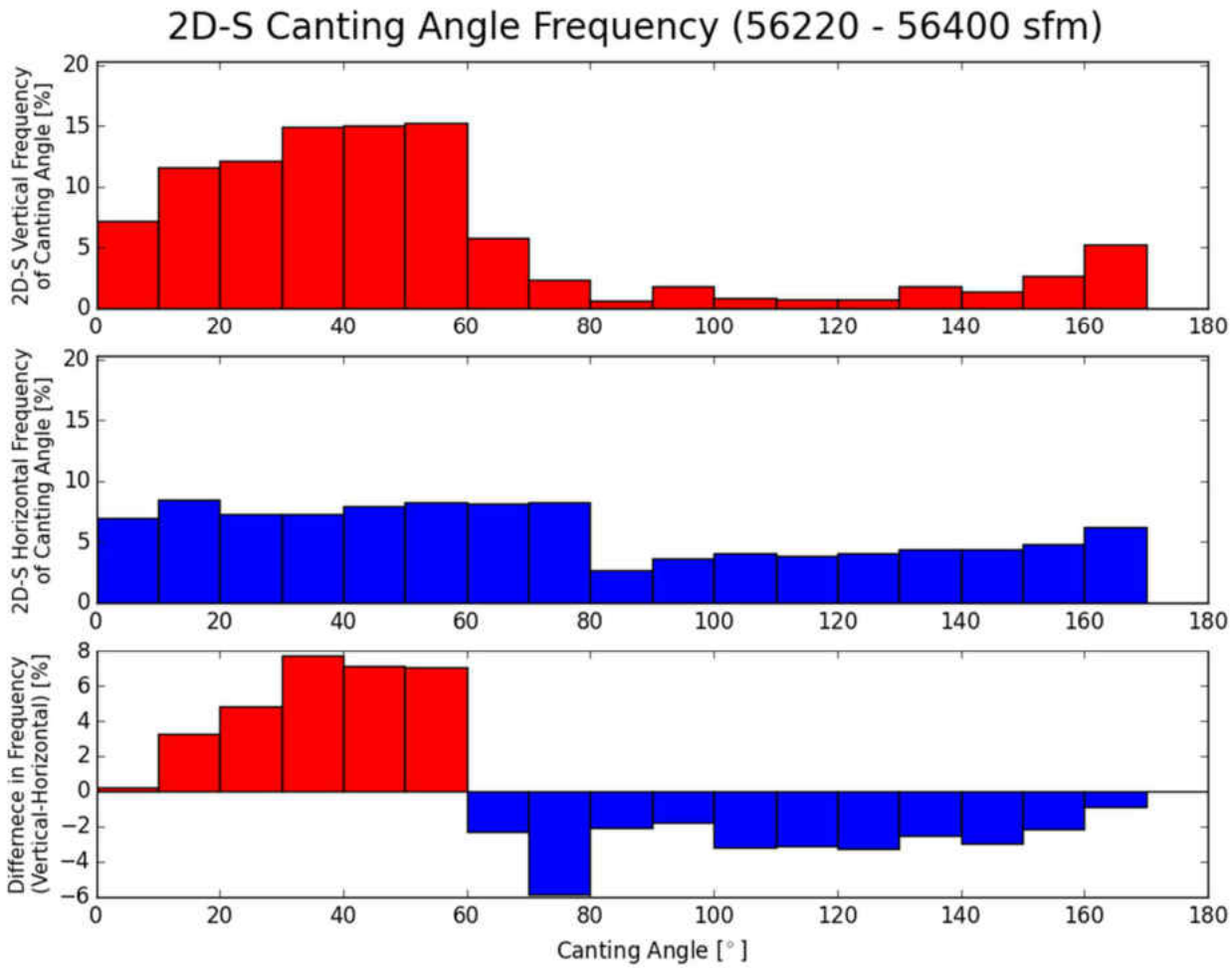

Figure 28: This figure shows canting angle frequency for 2DS column particle images from the 28 May 2014 flight from 56220 to 56400 sfm.

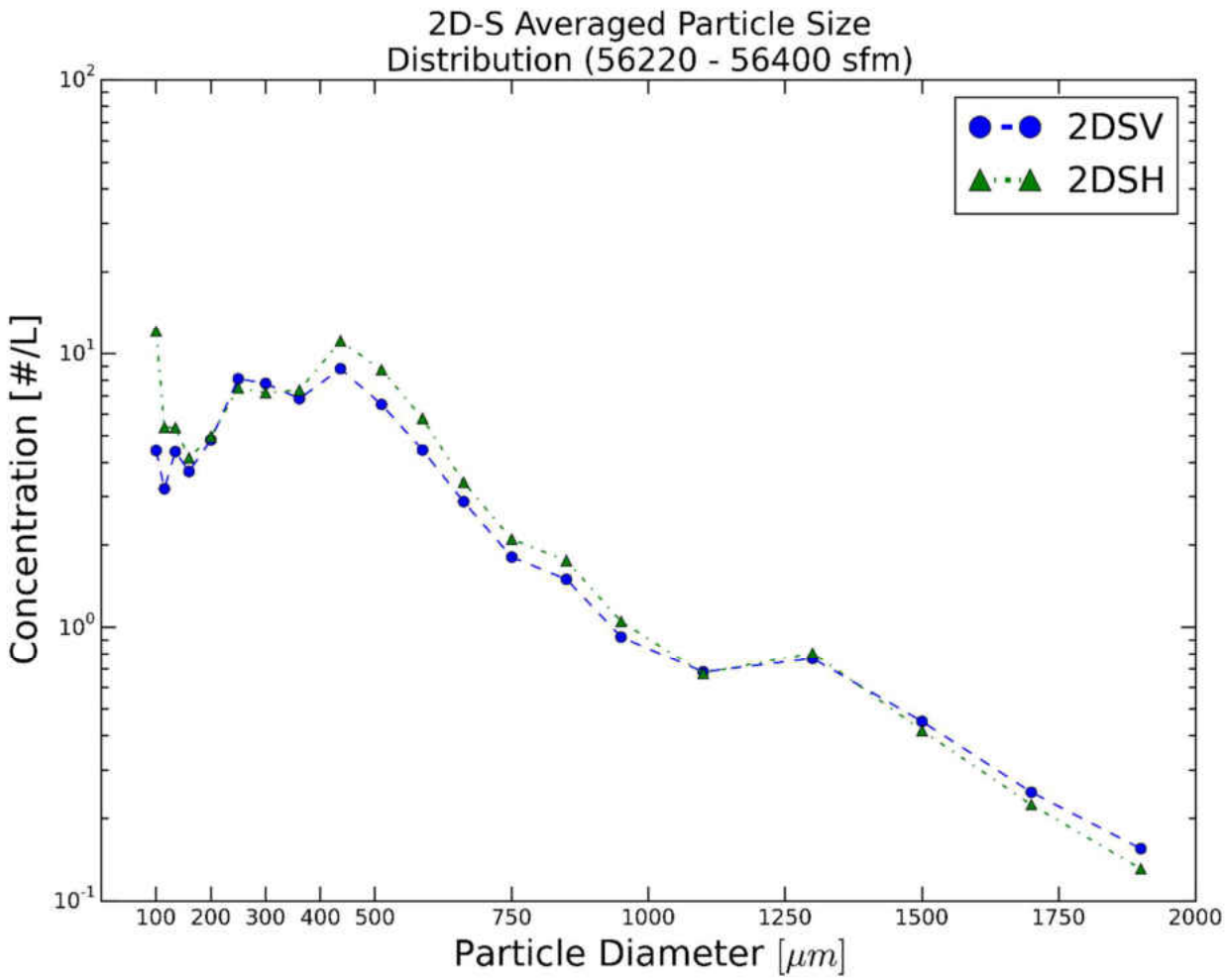

Figure 29: This figure shows 2DS averaged particle size distributions of the 28 May 2014 flight from 56220 to 56400 sfm.

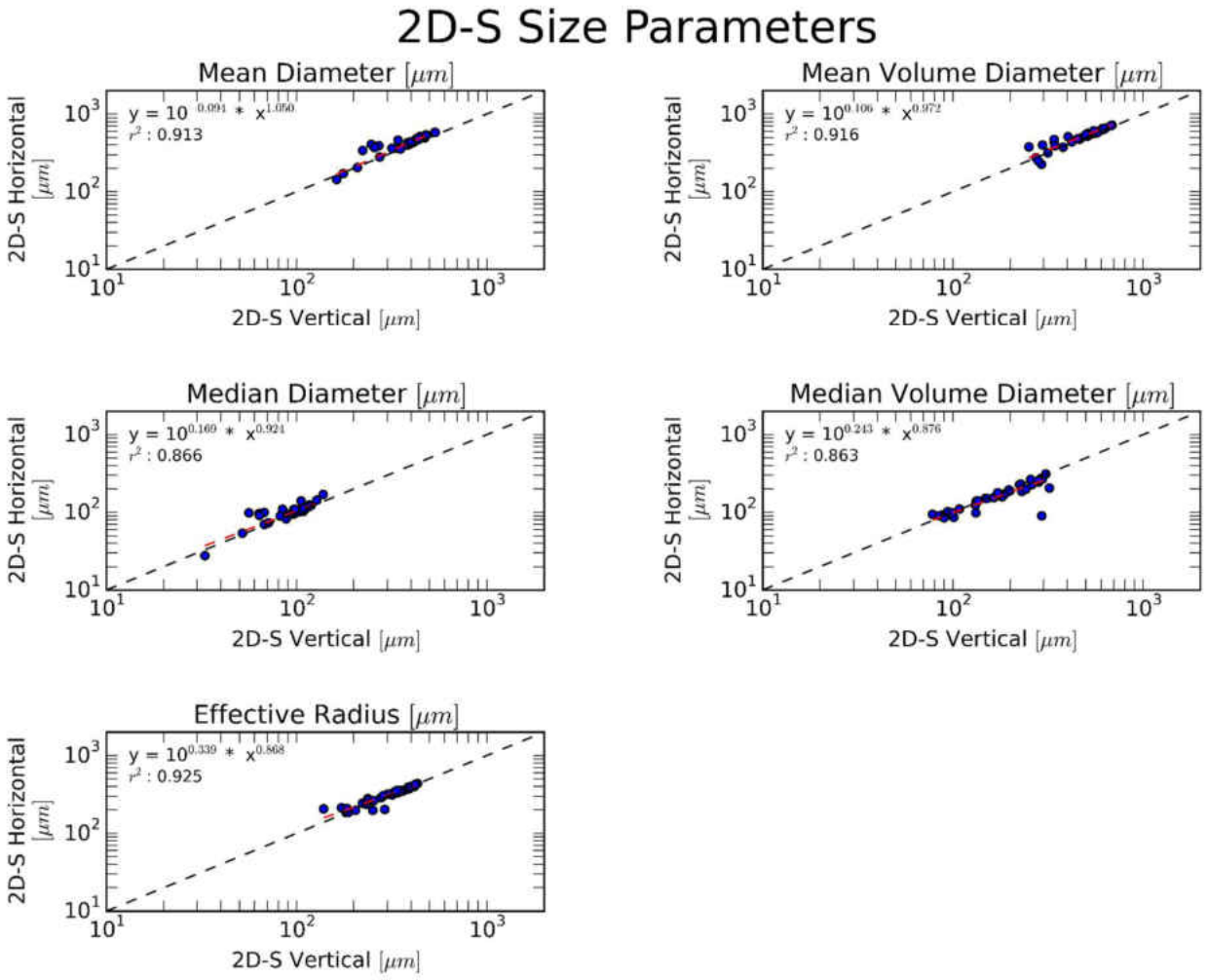

Figure 30: This figure shows 2DS derived size parameters from the 28 May 2014 flight from 56220 to 56400 sfm. Data represents five second averages of the original 1 Hz data for each parameter.

As seen in the figures, there is not a stark contrast in aspect ratio and area ratio measurements between the orientations of the 2DS. Within Figure 26, the vertical array of 2DS contains higher values of aspect ratio for particles less than 300 microns compared to the horizontal array. At the same time, the vertical array has slightly lower values for particles greater than 500 microns from 56260 to 56300 sfm, and also between 56340 to 56350 sfm. There is however a stark difference in aspect ratio measurements at 300 microns for both 2DS arrays. A possibility for this is the presence of short columns, which have a particle axis ratio close to one (i.e. major and minor particle axes are approximately the same length). An image of one of these short columns can be found within the center of Figure 10, where the short column has a maximum dimension of 314 μm. Figure 27 contains similar area ratio measurements for both orientations. The only discernable difference is the slightly greater values of area ratio (~ 0.65) for particles less than 250 microns.

In order to determine if the column images within the 2DS-V array contain a constant canting angle, the frequency of canting angle is displayed in Figure 28. If 2DS particle images have a preferred canting angle, the frequency distribution will contain a maximum. Likewise, if there is not a constant canting angle within the particle images, no distinct particle orientation will contain a maximum. Within Figure 28, there is a maximum in the frequency distribution around 60° for the 2DS-V. However, there is no such maximum within the 2DS-H array. The canting angle frequency within Figure 28 accurately describes the 2DS column images from this case, as shown in Figure 11. It is interesting that there is a preferred orientation of particle images within one array of the 2DS, and not the other. Since the 2DS-V (2DS-H) array projects particles into the x-z (y-z) object plane (King 1986), any airflow within one lateral direction

could potentially produce orientation effects within the object plane associated within direction of airflow, and not the other.

2DS particle size distributions are found within Figure 29. While the 2DS arrays display similar distributions, the 2DS-H array contains larger particle concentrations for particles 400-1000 μm in diameter. 2DS derived size parameters for the column case are located within Figure 30. The slope of the linear fits for the mean diameter, mean volume diameter, and median diameter parameters are close to 1.0 for each of the parameters, indicating that these parameters have no discernable differences between orientations. This indicates that while the 2DS-V does contain a preferred orientation of columns, as shown in Figure 28, this preferred orientation has a marginal effect on the size of particle images. This suggests that there is no discernable difference in the size of column particles images. This can also be inferred from the particle size distributions. As mentioned previously, the particle size distributions are fairly similar, except for the larger concentration of particles for the 2DS-H. This larger concentration of 2DS-H particles could be explained by a larger number of particles removed from the 2DS-V array due to particle shattering.

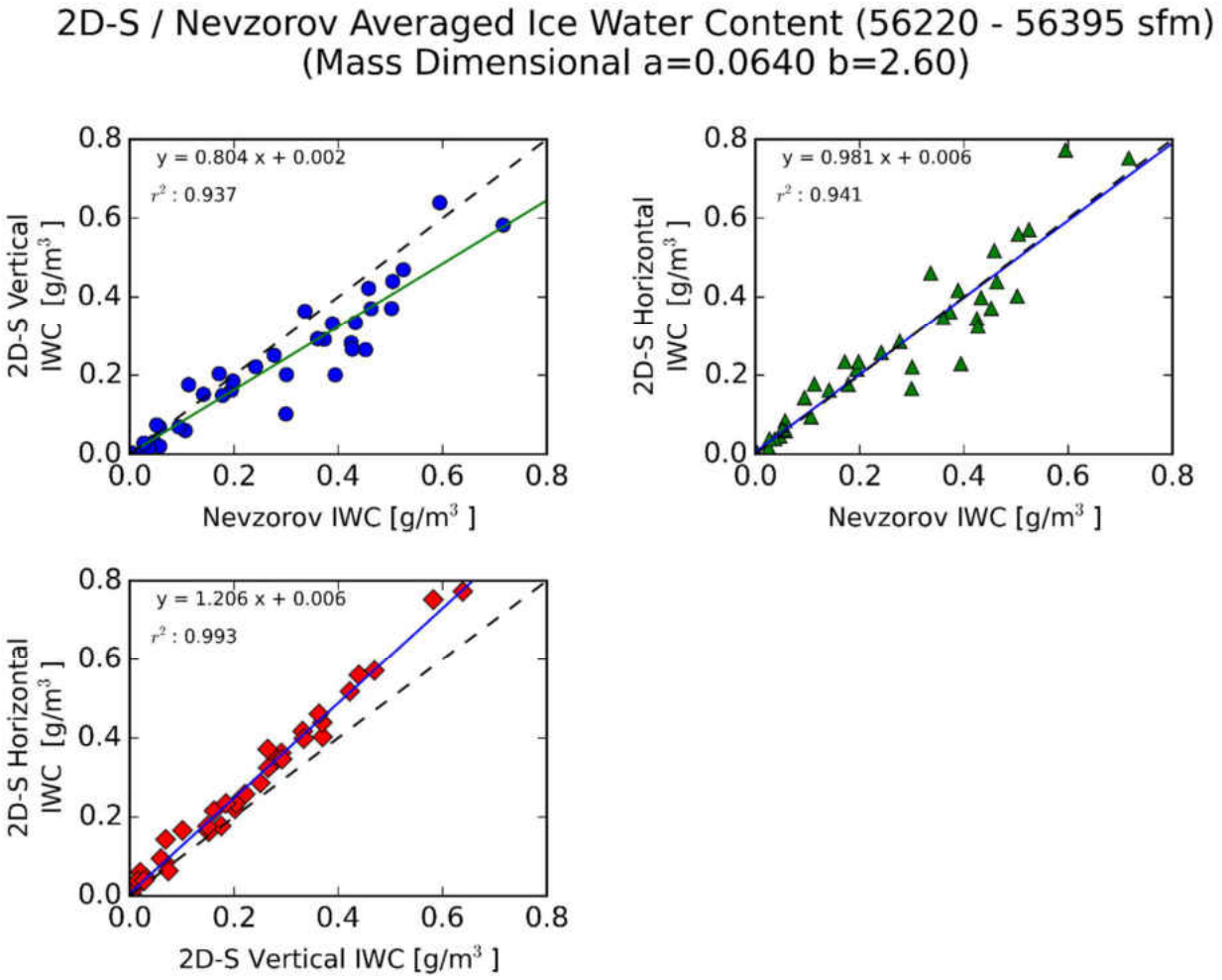

Figure 31: This figure shows Nevzorov and derived 2DS IWC from the 28 May 2014 flight from 56220 to 56400 sfm. 2DS IWC was derived using mass-dimensional method for columns. The average IWC for the 2DS-H (2DS-V) during this time period is 0.27 g/m^3 (0.22 g/m^3)

IWC for the column case was derived using the mass-dimensional relationship for columns outlined within Heymsfield and Kajikawa (1986), and is shown in Figure 31. Figure 31 shows overall a remarkable agreement between the 2DS (both orientations) and the Nevzorov hotwire probe. Curiously, IWC measurements derived from the 2DS-H array are larger by 20% compared to the 2DS-V values for this time period. Additionally, while the 2DS-H not only

contains larger IWC measurements compared to the 2DS-V, it is also in better agreement with the Nevzorov IWC. There is a clear bias within the 2DS-V IWC measurements when compared against the Nevzorov IWC, with differences as large as 0.2 grams per cubic meter. Since there was no discernable difference in 2DS size parameters from this time period, the IWC discrepancies are most likely due to the difference in particle concentrations between the arrays. Figure 32 contains the derived radar reflectivity factor measurements from the 2DS, which are in close agreement over the flight segment. However, there are a few segments of larger 2DS-H measurements, such as at 56360 sfm. This leads to a larger average radar reflectivity factor for the horizontal array (e.g. 0.92 dbZ).

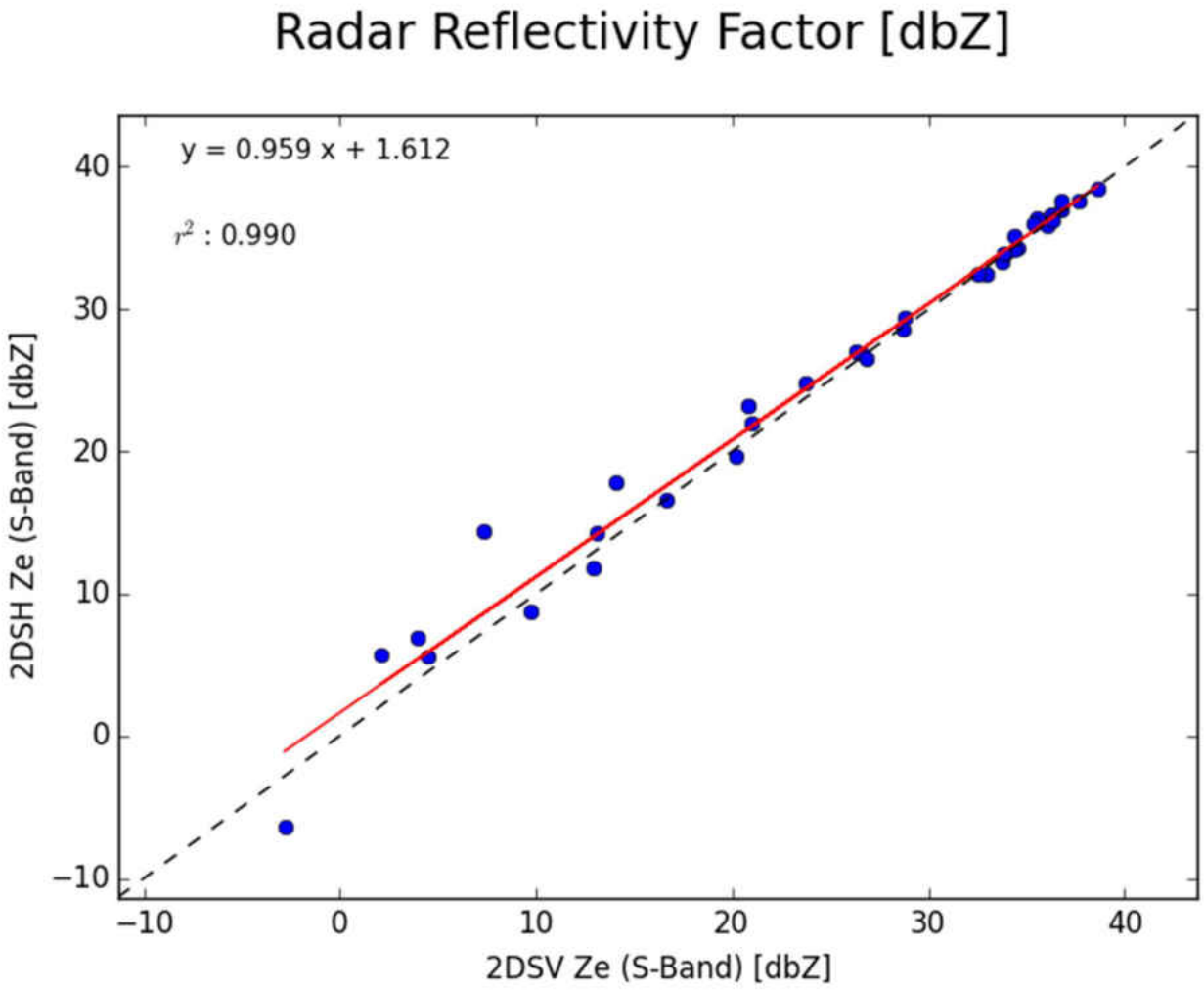

Figure 32: This figure shows 2DS radar reflectivity factor from the 28 May 2014 flight from 56220 to 56400 sfm. 2DS radar reflectivity factor was calculated using a constant dielectric constant (|K2| = 0.197) for S-band radar. The average radar reflectivity factor for the 2DS-H (2DS-V) during this time period is 26.7 dbZ (26.1 dbZ).

Table 8 contains averages of each of the 2DS parameters for the column cases. The 2DS-H contains slightly larger values for each parameter, except for median volume diameter. There is however a large range of average differences for each of the size parameters, which could potentially be due to the limited number of column cases observed. Derived IWC is 11.2%

greater for the 2DS-H values compared to the 2DS-V array, while the 2DS-H also contains 0.57 dbZ greater radar reflectivity measurements. These average differences between orientations is surprising, considering the size parameters only contain a slight difference. If each of the column cases follows the May 28th case, the differences could be attributed to concentration differences between orientations.

Table 8: This table contains averages of each 2DS parameter for all column cases. Difference represents the average difference between orientations of the 2DS. Minimum (maximum) represents the minimum (maximum) value of the average difference between orientations.

Parameter	Units	2DS-V	2DS-H	Difference	Min	Max
Mean Diam.	µm	413.42	436.16	-25.74	-44.53	9.16
Median Diam.	µm	106.3	108.38	-2.35	-8.91	5.22
Mean Vol. Diam.	µm	562.91	580.28	-17.37	-30.6	6.52
Median Vol. Diam.	µm	259.32	248.74	10.59	5.04	16.52
R_{eff}	µm	375.92	377.76	-1.83	-2.91	0.05
IWC	g/m^3	2.39	2.71	-0.31	-0.43	-0.11
Z_e	dbZ	25.84	26.41	-0.57	-0.92	-0.33

Needle Cases

The December 4th, 2015 (1700 Zulu) needle case within Figure 13 is the typical needle case observed during the OLYMPEx campaign. The orientation of needle particles is quite similar to the orientation of columns within the 2DS, with a preferred orientation of needles within the 2DS-V. Needles within the 2DS-H appear to be much more randomly orientated. Figure 33 and Figure 34 contain the aspect and area ratios for the needle cases. Aspect ratio

measurements are generally similar for the orientations of the 2DS, although the aspect ratio measurements for larger particle sizes are much higher than one would expect for needle

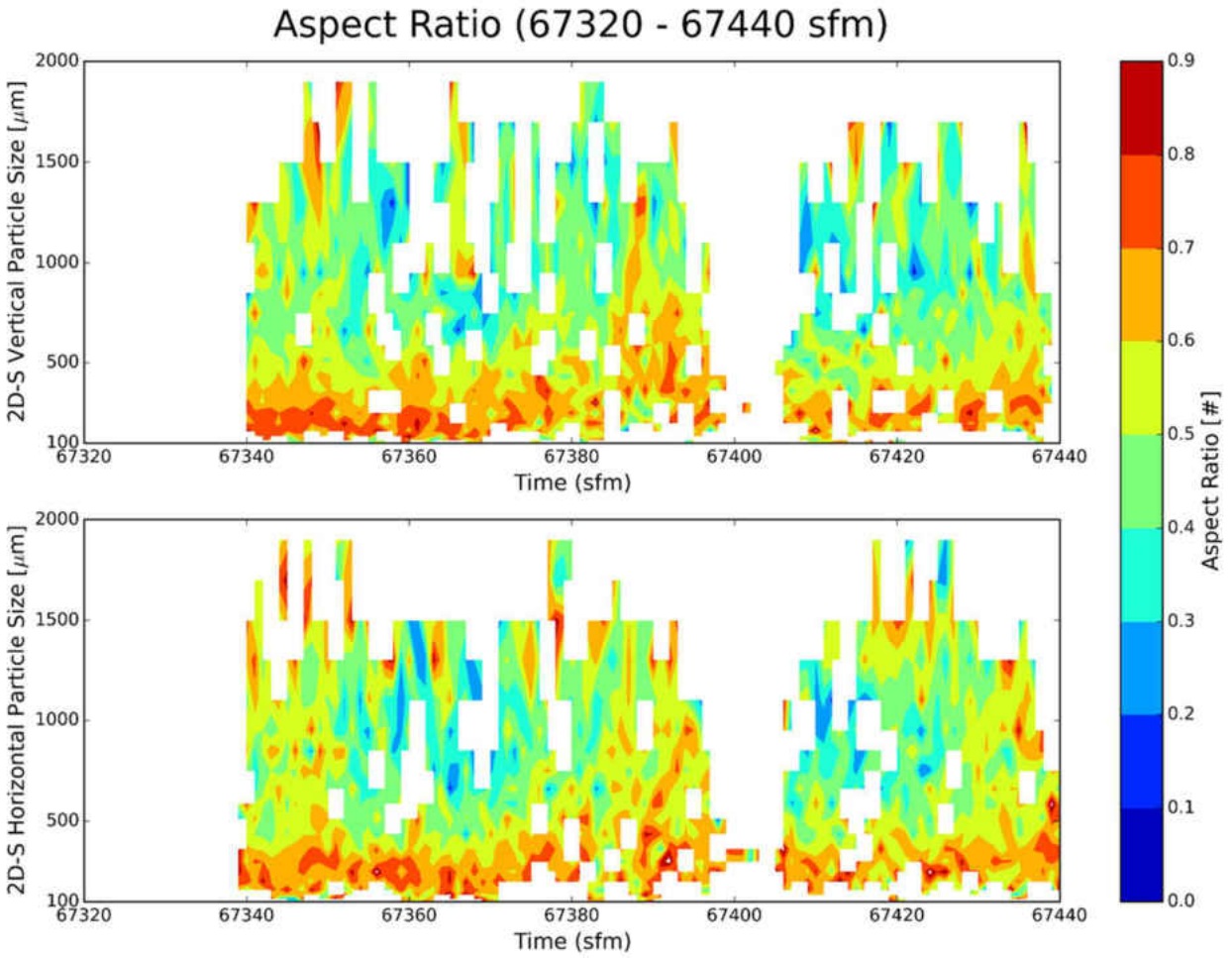

Figure 33: This figure contains 2DS measurements of aspect ratio for needle particles obtained during the 4 Dec. 2015 flight from 67320 to 67440 sfm.

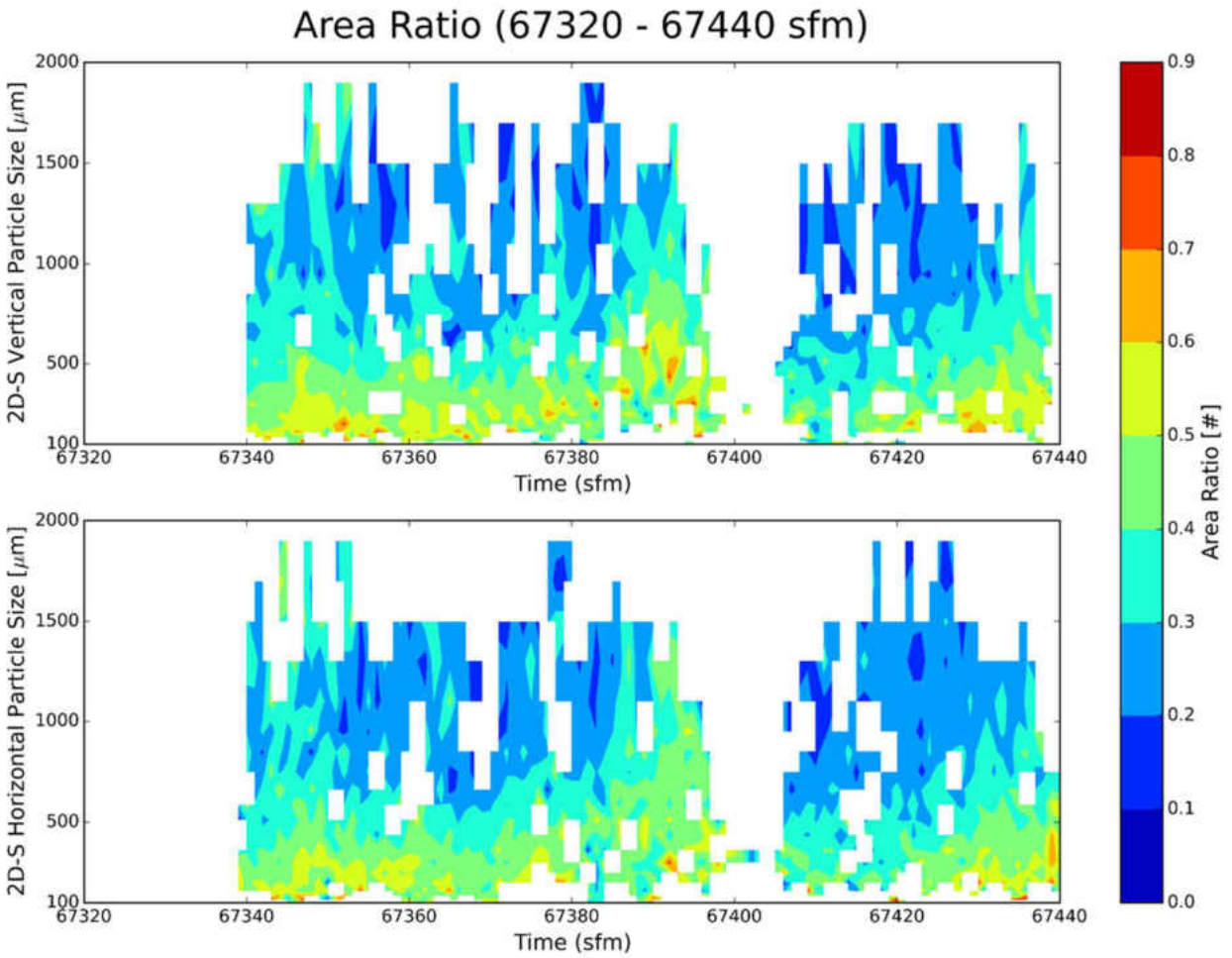

Figure 34: This figure shows 2DS measurements of area ratio for needle particles obtained during the 4 Dec 2015 flight from 67320 to 67440 sfm.

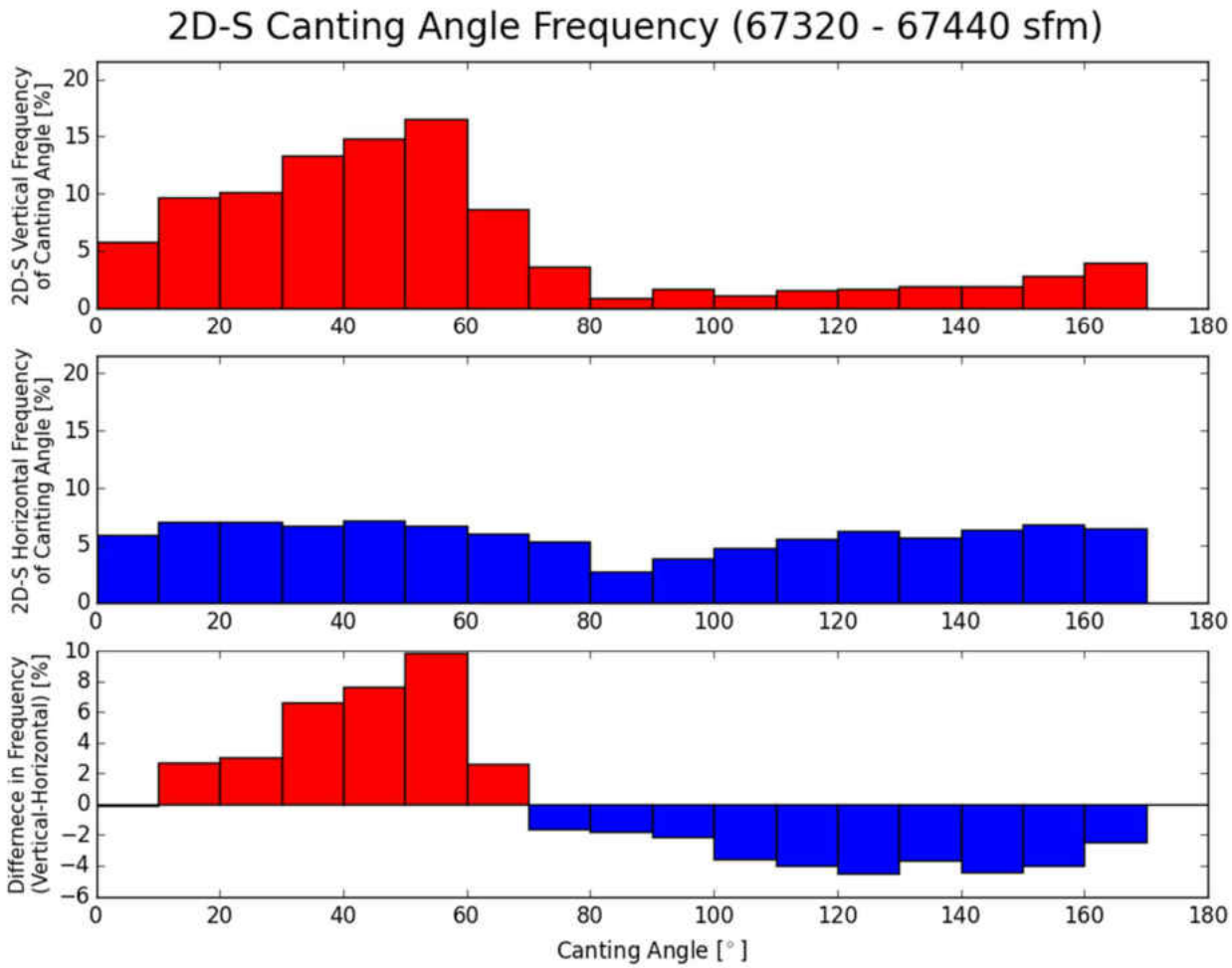

Figure 35: This figure contains canting angle frequency for 2DS needle particle images from the 4 Dec. 2015 flight from 67320 to 67440 sfm.

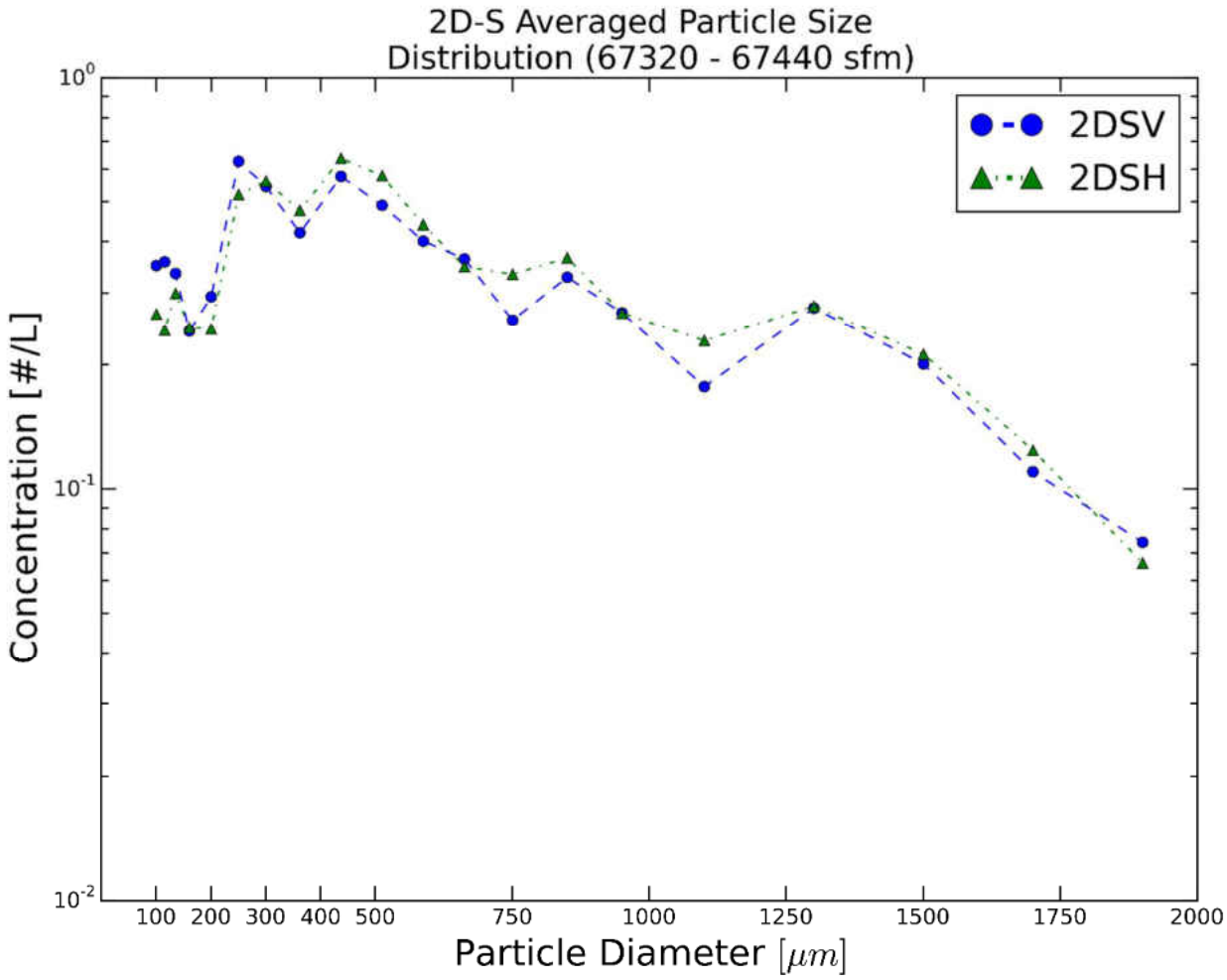

Figure 36: This figure shows 2DS averaged particle size distributions obtained during the 4 Dec. 2015 flight from 67320 to 67440 sfm.

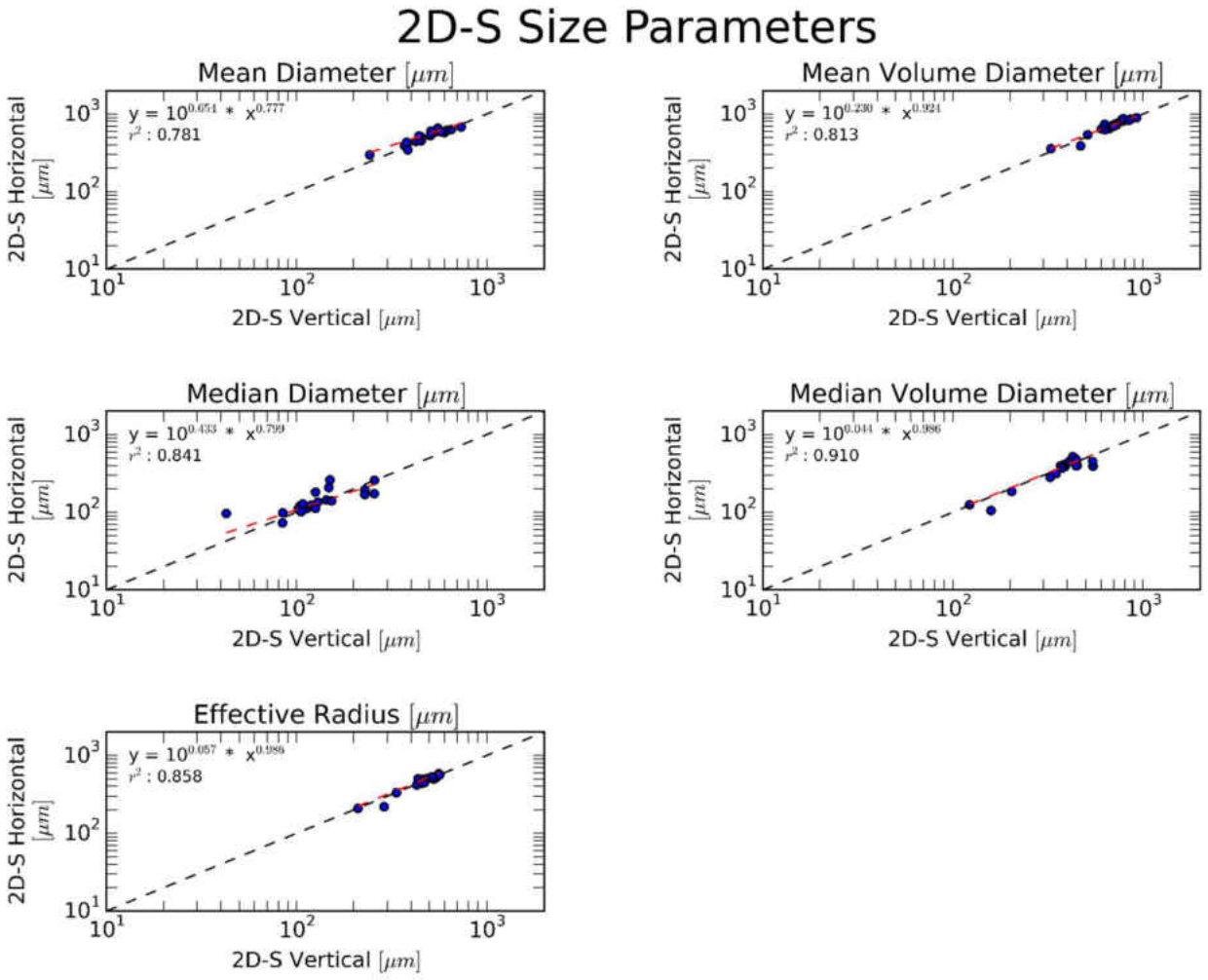

Figure 37: This figure shows 2DS derived size parameters obtained during the 4 Dec. 2015 flight from 67320 to 67440 sfm. Data represents five second averages of the original 1 Hz data for each parameter.

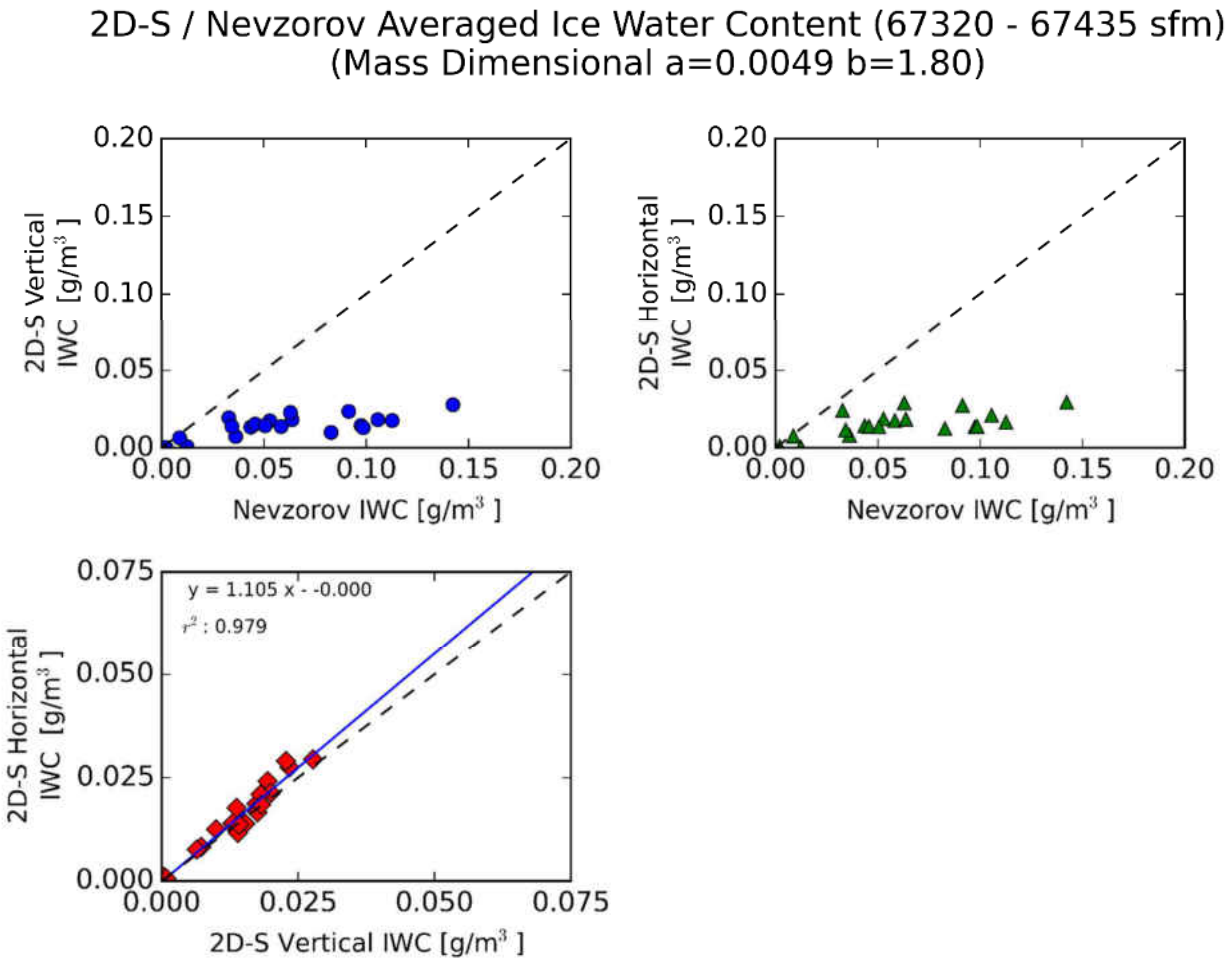

Figure 38: This figure shows Nevzorov and derived 2DS IWC from the 4 Dec. 2015 flight from 67320 to 67440 sfm. 2DS IWC was derived using mass-dimensional method for columns. The average IWC for the 2DS-H (2DS-V) for this time period is 0.01 g/m^3 (0.01 g/m^3

particles alone. This is indicative of needle aggregates within the environment, which also can be seen in the 2DS-H array within Figure 13. Needle aggregates contain greater surface area than needle particles and often contain maximum and minimum particle dimensions are of similar length, resulting in large aspect ratio values. The area ratio measurements are also similar between orientations of the 2DS and are low throughout this flight segment for both orientations.

There are some instances of higher area ratio for larger particle sizes, again reflecting the needle

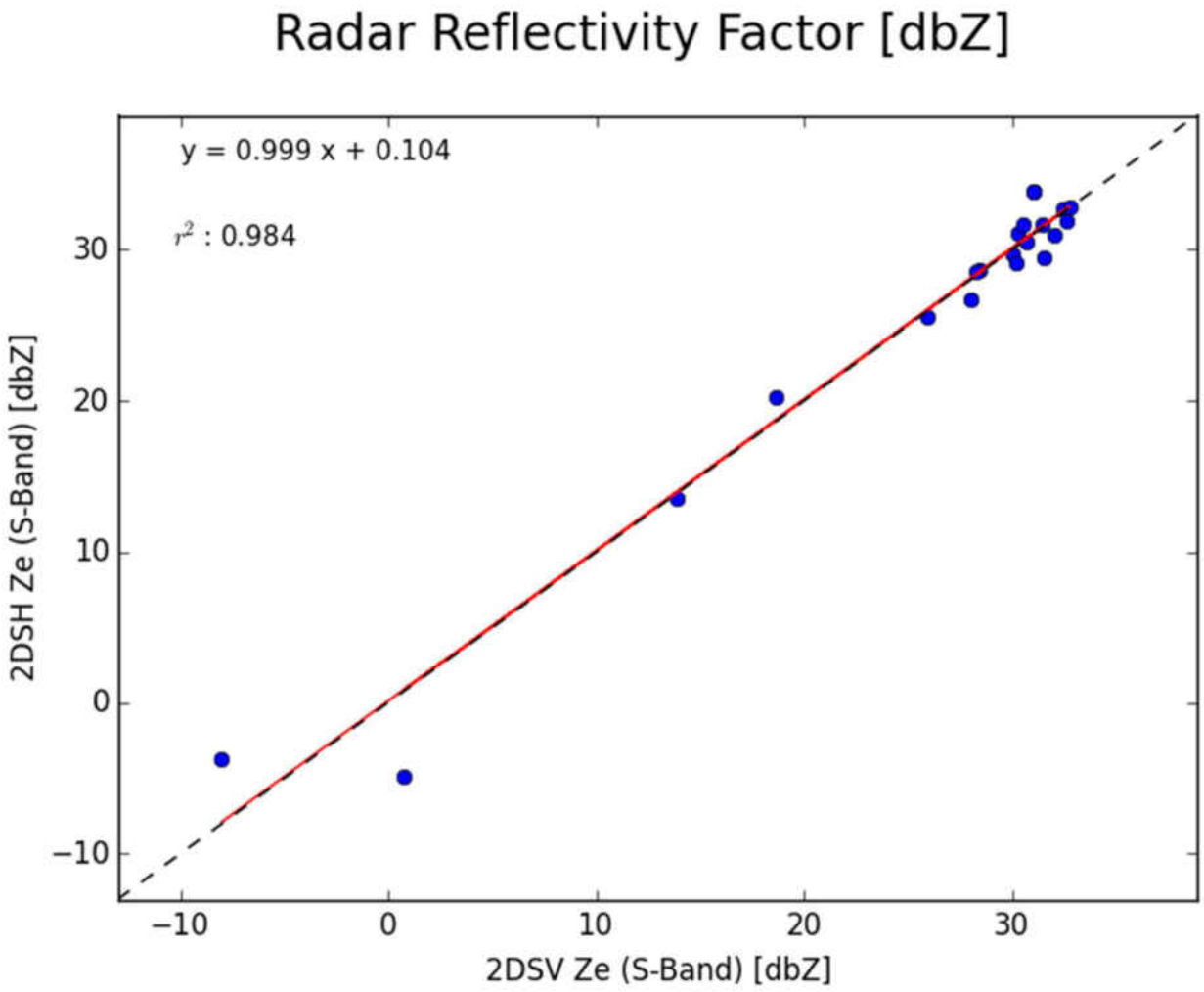

Figure 39: This figure shows 2DS radar reflectivity factor from the 4 Dec. 2015 flight from 67320 to 67440 sfm. 2DS radar reflectivity factor was calculated using a constant dielectric constant (|K2| = 0.197) for S-band radar. The average radar reflectivity factor for the 2DS-H (2DS-V) during this time period is 17.6 dbZ (15.8 dbZ).

aggregates within the 2DS particle images. Once again, since needle aggregates contain greater surface area, these particles will shade more pixels within the minimum bounding circle, resulting in larger area ratio values. Figure 35 contains the canting angle frequency for this needle case. As with the column case, there is a broad peak of the frequency distribution within the 2DS-V array, centering on the 60° canting angle orientation. This maximum is not found within the 2DS-H, which contains a flat frequency distribution. As with the column case, the frequency distribution indicates a preferred orientation of particles within the 2DS-V array, which accurately represents the particle images within Figure 13.

Figure 36 contains the size distributions for each 2DS array for this needle case. The size distributions contain multiple sharp peaks, suggesting the distribution contains a small sample size. Review of the particle images from the 2DS and HVPS3s from this time period indicate the UND Citation was not continuously in cloud, possibly on cloud edge, during this flight segment. While this is unfortunate, the December 4th, 2015 needle case is still the longest observance of the preferred orientation of needles within the 2DS-V. Figure 37 contains the average size parameters between the orientations of the 2DS, with no discernable difference between orientations for the majority of parameters. The only noticeable difference within the size parameters is mean diameter. The mean diameter parameter contains the lowest correlation between parameters (.78) and has a best fit line slightly above the one to one ratio line, indicating larger mean diameters for 2DS-H particle images. IWC measurements, calculated with the mass-dimensional relationship for needles, are found in Figure 38. The majority of measurements are found above the one to one ratio line, indicating larger the 2DS-H contains larger values. As the best fit line shows, the 2DS-H contains 10.5% greater values of IWC compared to the 2DS-V

array. Figure 38 also clearly shows disagreement between the Nevzorov IWC and IWC derived from the 2DS orientations. Inspection of the HVPS-3 particle images from this flight segment show large needle aggregates, with the largest particles roughly 0.5 cm in diameter. The Nevzorov hotwire is effective for particle diameters up to 4 mm, which is believed to be the upper cut size for the instrument. As described previous chapters, the 2DS can accurately size particles from 10 to 2000 microns (128 photodiode array with 10 micron pixel resolution). Therefore, in this instance, the Nevzorov hotwire is sampling particles outside of the 2DS size range, contributing to the discrepancy between Nevzorov and derived 2DS IWC. Additionally, low 2DS particle concentrations due to the non-continuous in-cloud measurements add to this discrepancy. The radar reflectivity factor measurements found in Figure 39 are in agreement for the majority of the flight segment. This is shown through the slopes of the best fit lines for the radar reflectivity factor comparison being close to one, with a slight offset.

For the needle cases, the 2DS-H array contains larger average size parameter values compared to the 2DS-V array. However, the average difference between 2DS orientations is slight. There is no discernable average difference between IWC measurements between the arrays. The 2DS-H contains 0.57 dbZ greater radar reflectivity factor measurements than the vertical array. The small sample size of needle particles within each of these cases, and the small number of needle cases, could potentially be affecting each of these parameter means.

Table 9: This table contains averages of each 2DS parameter for the needle cases. Difference represents the average difference between orientations of the 2DS. Minimum (maximum) represents the minimum (maximum) value of the average difference between orientations.

Parameter	**Units**	**2DS-V**	**2DS-H**	**Difference**	**Min**	**Max**
Mean Diam.	µm	448.57	470.25	-21.68	-40.24	-1.13
Median Diam.	µm	120.08	127.3	-7.21	-12.38	-3.73
Mean Vol. Diam.	µm	664.79	683.17	-18.38	-30.12	-1.34
Median Vol. Diam.	µm	402.29	404.13	-1.84	-8.65	1.52
R_{eff}	µm	474.55	480.17	-5.62	-10.59	0.22
IWC	g/m^3	0.04	0.04	0	-0.01	0
Z_e	dbZ	30.37	30.87	-0.51	-1.77	0.12

CHAPTER V

DISCUSSION AND CONCLUSIONS

Importance of Observations

Ice particles have long been assumed to have a random orientation within the sample volume of OAPs. This is why the preferred vertical orientation of planar ice particles (e.g. dendrites and plates) of the IPHEx and OLYMPEx observations is remarkable. It is important to note that this preferred vertical orientation is present in every instance of pristine planar ice particles. 2DS measurements of dendritic aggregates and irregular particles with side-planes represent a few instances where planar crystals are found within the vertical array. Neither of these types of ice particles are expected to have a natural horizontal orientation within the atmosphere, and thus are not considered within this study. However, the persistence of the vertical orientation of pristine planar ice particles within these campaigns suggests that these particles have been historically under-represented within OAP cloud measurements. This is the result of the historical vertical orientation of OAP instrumentation, which obtains measurements similar to the vertical 2DS array. This has been the preferred alignment in order to sample the largest cross-sectional area of ice particles, which assumes no particle reorientation. Additionally, OAP instrumentation are commonly vertically oriented in order to obtain measurements within a parallel optical path from remote-sensing platforms. Therefore, if only

vertically oriented OAP measurements are explored, there would be undercounting in the frequency of dendrites and plates within the measurements, since only the minor axis of these images are observed. As the results in the previous chapter indicate, not only will the frequency of particles will be affected, but also derived size parameters. All size parameters for planar ice crystals are larger on average for the 2DS-H.

Since the distribution of particles is larger for the 2DS-H, moments of the particle size distribution (e.g. IWC and radar reflectivity factor) should also be larger for the horizontal array. For dendrites, IWC and radar reflectivity factor are greater on average for the 2DS-H array. The difference in radar reflectivity factor indicates that there is greater returned power within the horizontal plane for radars. For plates, this signal is not as clear. LWC is actually greater, on average, for the 2DS-V. Each of the plate parameters shown in the previous chapter contain greater range within derived parameter differences, with a few cases dominating the field. For columnar particles, the orientation of particles is similar to previous research, with a preferred orientation of particles within the vertical array of the 2DS. For both columns and needles, the frequency of particle canting angle peaks at 60° for the vertical array, similar to the peak within the canting angle frequency distribution within King (1986). It is encouraging that the measurements from the 2DS-V was able to reproduce this constant canting angle. However, as the particle images from the columnar cases suggest, the 2DS-H does not contain a constant canting angle. This indicates there is not a preferred orientation of these particles within the 2DS-H particle images. Aspect and area ratio calculations were not able to describe this preferred orientation, as there is no disparity between the 2DS orientations. This could be due to the fact that these columns are not viewed on end within the viewing planes. As shown within the results,

this preferred orientation of columns does create differences within derived parameters for the 2DS. For IWC measurements, the 2DS-H contains greater values compared to the vertical array, and also contains better agreement with the Nevzorov IWC measurements. It should be noted that overall, the 2DS is in good agreement with the Nevzorov during the case shown. While needles follow the same trend as columns, the limited number of cases observed, and the low sampling statistics during these cases, leads to only slight differences between orientations. The comparison of the 2DS for these particles would greatly benefit from more cases, and improved sampling (higher concentration and greater amount of time within cloud) of these particles. However, even with the limited about of cases, the preferred orientation is found within the vertical array of the 2DS. These cases also contain the constant canting angle of 60°. This indicates that the calculations within King (1986) can be expanded to include all columnar particles.

The main objective of the UND Citation II during IPHEx and OLYMPEx was to provide high-resolution in-situ cloud measurements for comparison with multiple remote-sensing platforms. Results from this study indicate potentially large differences in derived size parameters, ice water content and radar reflectivity factor between orientations of the 2DS. Any remote-sensing algorithms or comparisons developed from the 2DS data, that does not take into account the discrepancies between measurements due to the preferred orientation of ice particles, could potentially be in error. For instance, optical depth is a derived parameter that is defined by the vertical measurement of optical thickness above a given altitude (Roger and Yao 1989). Optical depth is used to physically describe the radiative effects (e.g. scattering and absorption) of clouds and aerosols, and its calculation requires mean effective radius derived from a particle

size distribution. As shown in previous chapters, depending on particle habit, there are large discrepancies between 2DS orientations for effective radius measurements. For all dendrite cases, the 2DS-H has a larger mean effective radius measurement compared to the vertical array. The average difference is large (39.5 microns on the 23 May 2014 case). Additionally, the differences between particle characteristics, such as aspect and area ratio, will also affect a variety of cloud physics research areas. For instance, area ratio measurements are used to calculate particle terminal fall velocity. Particle terminal fall velocity calculations are used within atmospheric models and parameterizations in order to calculate particle growth and precipitation rates.

Explanation for Preferred Orientation

While there is a need to understand the effects of ice particle orientation on 2DS measurements, it is important to try to understand the mechanisms that lead to these orientations. Previously, King (1986) and MacPherson and Baumgardner (1988) attempted to describe the effects of airflow around cloud instrumentation on ice particle orientation. The basis for these studies was the observation of a preferred orientation of columnar ice particles within measurements obtained with the 2DC. This preferred orientation is similar to the orientation of columns observed with the 2DS-V. King (1986) found that aircraft induced flow distortions have considerable effects on ice crystal orientation, and there is sufficient aerodynamic torque to align particles along the direction of instantaneous drag. King (1986) was able to reproduce the canting angle of the 2DC columns through a theoretical analysis that defined the orientation as the relative change of airflow in the two orthogonal directions for wingtip mounted instruments.

MacPherson and Baumgardner (1988) found airflow velocities at the sampling location of a 2DC probe are reduced by a combination of effects from the wing, pylon and probe canister up to 1 meter ahead of the probe. Additionally, MacPherson and Baumgardner (1988) found a lateral spanwise (i.e. direction along the length of the wing) velocity component at the outboard sampling location, which produced a 3° sideslip angle at this location. This airflow acceleration could be the explanation for why the 2DS-H does not contain a preferred orientation of columnar particles. Since the 2DS-H optical path is in the spanwise direction, an acceleration within this direction would not be noticeable. The most likely effect would be to change the location of a particle within the optical depth of the horizontal array. This could potentially increase the concentration of particles within the 2DS-H if particles that normally would pass outside the minimum detection threshold are moved closer to the photodiode array, increasing pixel shading. While the orientation of columns was able to be reproduced, neither of these studies offer an explanation for the vertical orientation of planar crystals observed within this current study. Additionally, since there is not an independent confirmation of ice particle habit within each of these previous studies, the observed orientation could potentially be the side-view of planar crystals.

Since the airflow analysis within these studies does not explain the vertical alignment of planar ice crystals, additional mechanisms for this orientation must be considered. A possible explanation, which few studies have addressed, is the electrical field effects induced by the aircraft. Burrows and Stith (1985) modeled the electric charge on the UND Citation II aircraft in order to describe the change in crystal orientation as a charge object approaches these particles. Burrows and Stith (1985) used a simple spherical model to calculate the electric field associated

with airframe charging due to crystal collisions and found that there was significant angular acceleration to reorient columnar ice crystals. The study shows that for particles with a 0° initial atmospheric orientation, depending on the distance from the sampling location, the angle between the electric field and ice particle will be positive. This positive direction will result in a positive counterclockwise torque, sufficient enough to orient particles 90° at the sampling location (Burrows and Stith 1985). The study concluded significant alignment of ice crystals should occur as a rapidly moving charged object approaches, and that the angular motion of ice crystals differs considerably for different initial crystal orientations. Interestingly, Burrows and Stith (1985) show that previous studies have found that the maximum charging rate of the aircraft occurred in atmospheric temperatures between -7°C and -9°C, and wingtip electric fields were found to be seven times greater than that of the fuselage. This temperature range is where the majority of the dendrite and plate cases are found within this study. While Burrows and Stith (1985) may provide the explanation for the vertical alignment of planar crystals within the 2DS sample volume, there has yet to be observations to confirm the simple electric field model used within their study. Therefore, in order to truly identify the mechanisms for the particle orientation, additional measurements of airflow and electric fields around the aircraft, ambient and induced, are needed.

Conclusion

This purpose of this study is to understand the effects of particle orientation on 2DS ice particle measurements. It is often assumed the observed particle orientation is random at the sampling location of aircraft due to the differential acceleration of airflow around the wingtips

(Hogan et al. 2012). However, there has yet to be analysis of ice particle measurements from orthogonal OAPs to prove this assumption. In order to estimate the orientation of particles within the sample volume of the 2DS, the orientation of ice particles with a natural atmospheric horizontal orientation are investigated. The orientation of these particles within the sample volume of the 2DS will determine possible orientation effects. Orientation effects considered are random, preferred, or no orientation. Analysis of 2DS particle images obtained during the IPHEx and OLYMPEx field campaigns indicate a preferred orientation of planar and columnar ice particles. For planar crystals (e.g. dendrites and plates), the preferred orientation is such that these particles are vertically oriented within the sample volume of the 2DS. This preferred orientation creates differences in measurements of particle characteristics (e.g. aspect and area ratios), particle size parameters, derived ice water content, and derived radar reflectivity factor obtained with the orthogonal photodiode arrays of the 2DS. For the majority of these cases, the horizontal array of the 2DS contains larger values for measurements obtained during each of these cases as compared to the vertical array. Thus, any instrument comparison, algorithm development, or model parameterization developed from the IPHEx and OLYMPEx 2DS measurements must take into account this preferred orientation in order to avoid potential errors. It is not yet determined if this orientation is found in all 2DS measurements of pristine ice crystals. It is possible that the UND Citation II has a unique airflow feature that affects particle orientation. Additional research is needed into measurements obtained on a different airframe to determine if the preferred orientation found within this study applies to all 2DS measurements. While there is not a definite explanation for this preferred orientation, two mechanisms (e.g. airflow and electric field effects) explored in previous research are presented. Theoretical and

observational measurements of the differential acceleration of airflow around wingtip mounted instrumentation, described within King (1986) and MacPherson and Baumgardner (1988), are able to accurately reproduce the preferred orientation of columnar crystals. However, this airflow analysis is not able to reproduce the vertical orientation of planar crystals observed within this study. A possible explanation for this orientation is described within Burrows and Stith (1985), which contains a theoretical analysis of the induced electric charge on a sampling aircraft and its effect on the orientation of ice particles. Burrows and Stith (1985) are able to show there is sufficient angular momentum for particles to be vertically aligned (90° orientation) at the sampling location, if the particles have an initial orientation of 0°. While this is a possible explanation for the observed orientation of planar crystals, additional measurements are needed in order to confirm the simple electrical model outlined within Burrows and Stith (1985).

REFERENCES

Bréon, F. M., & Dubrulle, B. (2011). Horizontally oriented plates in clouds. *arXiv preprint arXiv:1106.1227*

Brown, P.R.A, and P. N. Francis, 1995: Improved Measurements of the Ice Water Content in Cirrus Using a Total-Water Probe. *J. Atmos. Oceanic Technol.* **12**, 410–414

Burrows, D. A., & Stith, J. L. (1986). Alignment of fee Crystals due to Transient Electric Fields. *Journal of Atmospheric and Oceanic Technology*, *3*(2), 265-272.

Cho, H-R., J. V. Iribarne, and W. G. Richards, 1981: On the orientation of ice crystals in a cumulonimbus cloud. *J. Atmos. Sci.*, **38**, 1111–1114.

Cotton, R. J., Field, P. R., Ulanowski, Z., Kaye, P. H., Hirst, E., Greenaway, R. S., ... & Dorsey, J. (2013). The effective density of small ice particles obtained from in situ aircraft observations of mid-latitude cirrus. *Quarterly Journal of the Royal Meteorological Society*, *139*(676), 1923-1934.

Delene, D. J. (2011). Airborne data processing and analysis software package. *Earth Science Informatics*, *4*(1), 29-44.

Hou, A.Y, R.K. Kakar, S. Neeck, A.A. Azarbarzin, C. D. Kummerow, M. Kojima, R. Oki, K. Nakamura, and T. Iguchi, 2014: The Global Precipitation Measurement Mission. *Bull. Amer. Meteor. Soc.* **95**, 701–722

Heymsfield, A. (1972). Ice crystal terminal velocities. *Journal of the Atmospheric Sciences*, *29*(7), 1348-1357.

Heymsfield, A. J., & Kajikawa, M. (1987). An improved approach to calculating terminal velocities of plate-like crystals and graupel. *Journal of the atmospheric sciences*, *44*(7), 1088-1099.

Heymsfield, A. J., Bansemer, A., Schmitt, C., Twohy, C., & Poellot, M. R. (2004). Effective ice particle densities derived from aircraft data. *Journal of the atmospheric sciences*, *61*(9), 982-1003.

Hogan, R. J., Tian, L., Brown, P. R., Westbrook, C. D., Heymsfield, A. J., & Eastment, J. D. (2012). Radar scattering from ice aggregates using the horizontally aligned oblate spheroid approximation. *Journal of Applied Meteorology and Climatology*, *51*(3), 655-671.

King, W. D., 1986: Air flow and particle trajectories around aircraft fuselages iv: orientation of ice crystals. *J. Atmos. Oceanic Technol.*, **3**, 433–439.

Korolev, A., and G. Isaac, 2003: Roundness and aspect ratio of particles in ice clouds. *J. Atmos. Sci.*, **60**, 1795–1808.

Knollenberg, R.G., 1970: The Optical Array: An Alternative to Scattering or Extinction for Airborne Particle Size Determination. *J. Appl. Meteor.* **9**, 86–103

Lawson, R.P., D. O'Connor, P. Zmarzly, K. Weaver, B. Baker, Q. Mo, and H. Jonsson, 2006: The 2d-s (stereo) probe: design and preliminary tests of a new airborne, high-speed, high-resolution particle imaging probe. *J. Atmos. Oceanic Technol.*, **23**, 1462–1477.

Lawson, R. P. (2011). Effects of ice particles shattering on the 2D-S probe. *Atmospheric Measurement Techniques*, *4*(7), 1361-1381.

List, R., and R. S. Schemenauer, 1971: Free-fall behavior of planar snow crystals, conical graupel and small hail. *J. Atmos. Sci.*, **28**, 110–115.

MacPherson, J. I., & Baumgardner, D. (1988). Airflow about King Air wingtip-mounted cloud particle measurement probes. *Journal of Atmospheric and Oceanic Technology*, *5*(2), 259-273.

Marchand R., G. G. Mace, A. G. Hallar, I. B. McCubbin, S. Y. Matrosov, and M. D. Shupe, 2013: Enhanced radar backscattering due to oriented ice particles at 95 ghz during stormvex. *J. Atmos. Oceanic Technol.*, **30**, 2336–2351.

Matrosov, S. Y. (2007). Modeling backscatter properties of snowfall at millimeter wavelengths. *Journal of the atmospheric sciences*, *64*(5), 1727-1736.

McFarquhar, G. M., Heymsfield, A. J., Macke, A., Iaquinta, J., & Aulenbach, S. M. (1999). Use of observed ice crystal sizes and shapes to calculate mean-scattering properties and multispectral radiances: CEPEX April 4, 1993, case study. *Journal of Geophysical Research: Atmospheres*, *104*(D24), 31763-31779.

Pruppacher, H.R., J.D. Klett, 1996: Microphysics of clouds and precipitation: second revised and expanded edition with an introduction to cloud chemistry and cloud electricity. Springer Netherlands, 954 pp.

Rogers, R. R., & Yau, M. K., 1989: A short course in cloud physics. Oxford: Pergamon Press.

Schefold, R., B. Baschek, M. Wuest, and E. Barthazy, 2002: Fall velocity and axial ratio of snowflakes. *Proceedings of ERAD (2002)*, 84.

Sulia, K. J., and J. Y. Harrington, 2011: Ice aspect ratio influences on mixed-phase clouds: impact on phase partitioning in parcel models, *J. Geophys. Res.,* 116.

Theisen, C. J., Kucera, P. A., & Poellot, M. R. (2009). A study of relationships between Florida thunderstorm properties and corresponding anvil cloud characteristics. *Journal of Applied Meteorology and Climatology*, *48*(9), 1882-1901.

Westbrook, C. D., Illingworth, A. J., O'Connor, E. J., & Hogan, R. J. (2010). Doppler lidar measurements of oriented planar ice crystals falling from supercooled and glaciated layer clouds. *Quarterly Journal of the Royal Meteorological Society*, *136*(646), 260-276.